Damage limits of superconducting magnets in case of impact by high intensity particle beams

Zur Erlangung des akademischen Grades eines

Doktors der Naturwissenschaften (Dr. rer. nat.)

von der KIT-Fakultät für Physik des
Karlsruher Instituts für Technologie (KIT)

angenommene

Dissertation

von

M.Sc. David Gancarcik

aus Karviná (Tschechien)

Tag der mündlichen Prüfung: 12. Juni 2026
1. Referentin: Prof. Dr. Anke-Susanne Müller
2. Referent: Prof. Dr. Rüdiger Schmidt

Eidesstattliche Versicherung gemäß § 13 Absatz 2 Ziffer 3 der Promotionsordnung des Karlsruher Instituts für Technologie (KIT) für die KIT-Fakultät für Physik:

1. Bei der eingereichten Dissertation zu dem Thema
   "Damage limits of superconducting magnets in case of impact by high intensity particle beams"
   handelt es sich um meine eigenständig erbrachte Leistung.
2. Ich habe nur die angegebenen Quellen und Hilfsmittel benutzt und mich keiner unzulässigen Hilfe Dritter bedient. Insbesondere habe ich wörtlich oder sinngemäß aus anderen Werken übernommene Inhalte als solche kenntlich gemacht.
3. Die Arbeit oder Teile davon habe ich wie folgt/bislang nicht an einer Hochschule des In- oder Auslands als Bestandteil einer Prüfungs- oder Qualifikationsleistung vorgelegt.

   Titel der Arbeit: Damage limits of superconducting magnets in case of impact by high intensity particle beams
   Hochschule und Jahr: Karlsruher Institut für Technologie, 2026
   Art der Prüfungs- oder Qualifikationsleistung: Dissertation zur Erlangung des akademischen Grades eines Doktors der Naturwissenschaften (Dr. rer. nat.)
4. Die Richtigkeit der vorstehenden Erklärungen bestätige ich.
5. Die Bedeutung der eidesstattlichen Versicherung und die strafrechtlichen Folgen einer unrichtigen oder unvollständigen eidesstattlichen Versicherung sind mir bekannt.

Ich versichere an Eides statt, dass ich nach bestem Wissen die reine Wahrheit erklärt und nichts verschwiegen habe.

Ort und Datum	Unterschrift
_____	_____

Abstract

This thesis investigates the damage limits of superconducting accelerator magnets subjected to high-intensity proton beam impacts, with the aim of supporting the safe and reliable operation of current and future high-energy accelerators. To evaluate the material response, a dedicated beam impact experiment was conducted at CERN's HiRadMat facility, using custom-fabricated sample coils. The critical current of the samples was measured before and after irradiation to assess the onset of performance degradation. A comprehensive numerical model, combining experimental beam parameters with Monte Carlo and Finite Element Method simulations, was developed to characterize the energy deposition and thermo-mechanical response of the coils. The results demonstrate that non-impregnated coils based on Nb-Ti conductors can withstand localized energy deposition up to $3.03 \pm 0.21\,\mathrm{kJ\,cm^{-3}}$, corresponding to peak temperatures of $988 \pm 61\,\mathrm{K}$, without measurable degradation in critical current. Nb_3Sn coils, impregnated with CTD-101K epoxy, maintained their critical current up to an energy deposition of $1.75 \pm 0.09\,\mathrm{kJ\,cm^{-3}}$, corresponding to hotspots of $695 \pm 28\,\mathrm{K}$ and mechanical strain of $0.42\,\%$.

Some de-training of the sample coils was observed following irradiation, which could not be attributed solely to thermal cycling. Beam-induced defects were identified in the epoxy, but these had no impact on coil performance. Extrapolations from the tested coils to full-scale accelerator magnets are discussed. These findings contribute to improved magnet protection strategies and provide essential input for the design of resilient superconducting systems in next-generation particle accelerators.

Zusammenfassung

Diese Arbeit untersucht die Schadensobergrenzen von supraleitenden Beschleunigermagneten, die der Einwirkung eines hochintensiven Protonenstrahls ausgesetzt sind. Das Ziel dabei ist, den sicheren und zuverlässigen Betrieb aktueller und zukünftiger Hochenergiebeschleuniger zu gewährleisten. Zur Untersuchung des Materialverhaltens wurde in der HiRadMat-Anlage am CERN ein Bestrahlungsexperiment mit speziell angefertigten Testspulen durchgeführt. Der kritische Strom der Proben wurde vor und nach der Bestrahlung gemessen, um mögliche Leistungseinbußen in Abhängigkeit von der eingetragenen Energie festzustellen. Es wurde ein umfassendes numerisches Modell entwickelt, das die gemessenen Strahlparameter mit Monte-Carlo- und Finite-Elemente-Methoden-Simulationen kombiniert, um den Energieeintrag und die thermomechanische Reaktion der Spulen zu charakterisieren. Die Ergebnisse zeigen, dass nicht imprägnierte Spulen auf Basis von Nb-Ti-Leitern einem lokalen Energieeintrag von bis zu $3.03 \pm 0.21\,\mathrm{kJ\,cm^{-3}}$ standhalten können, was einem Hotspot von $988 \pm 61\,\mathrm{K}$ entspricht, ohne dass eine messbare Reduktion des kritischen Stroms auftritt. In ähnlicher Weise behielten Nb_3Sn-Spulen, die mit CTD-101K-Epoxidharz imprägniert waren, ihren kritischen Strom bis zu $1.75 \pm 0.09\,\mathrm{kJ\,cm^{-3}}$ bei, was Hotspots von $695 \pm 28\,\mathrm{K}$ und einer mechanischen Dehnung von etwa $0.42\,\%$ entspricht.

Nach der Bestrahlung wurde eine gewisse, nicht permanente Leistungseinbuße an den Testspulen beobachtet, der nicht allein auf die thermischen Zyklen zurückgeführt werden konnte. Kleine Risse im Epoxidharz wurden nach der Bestrahlung identifiziert. Diese hatten keine Leistungseinbuße zur Folge. Es werden Extrapolationen von den Testspulen auf Beschleunigermagnete in Originalgröße diskutiert. Diese Erkenntnisse tragen zu verbesserten Strategien zum Schutz der Magnete bei und liefern wichtige Informationen für die Auslegung betriebssicherer supraleitender Systeme in Teilchenbeschleunigern der nächsten Generation.

Contents

Introduction

The Standard Model of particle physics has had remarkable success in describing fundamental particles and their interactions. Particle colliders are an excellent tool for validating the current theory and probing physics beyond it. The Large Hadron Collider (LHC), which is currently operating at a maximum beam energy of 6.8 TeV, is undergoing a major upgrade as part of the High-Luminosity LHC project (HL-LHC). It is expected to begin operating in 2030, significantly increasing the collision rate and thereby enabling high-precision measurements and improved sensitivity to rare processes and potential deviations from the Standard Model.

High-energy hadron colliders rely on superconducting magnets to generate the intense magnetic fields required to steer and focus particle beams. However, during operation, these magnets and their components are exposed to radiation. There are two types of beam losses that lead to exposure of the magnets to radiation. Firstly, steady beam losses, which occur continuously during operation. Secondly, accidental beam losses, which happen sporadically due to hardware failures or severe beam instabilities. These accidental beam losses can lead to the generation of secondary particle showers, resulting in significant energy deposition in the accelerator magnets. In a severe case, the energy deposition happens on microsecond timescales, causing rapid heating and the development of thermo-mechanical stresses within the magnet coils.

Superconducting magnet coils, composed of superconducting strands, are sensitive to such stresses. Exposure can permanently degrade their performance, such as the critical current. As these properties are crucial for the reliable operation of superconducting magnets, such degradation could necessitate magnet replacement, resulting in extended downtime and reduced collider availability for physics data taking.

In light of these challenges, this thesis aims to investigate how superconducting accelerator magnet coils respond to sudden, intense thermal and mechanical shocks resulting from accidental beam losses. The focus is on Nb-Ti coils similar to those used in dipole magnets of the LHC and Nb_3Sn coils similar to those in the final focusing quadrupoles of the HL-LHC. The core objective is to determine how thermo-mechanical stresses from accidental beam losses impact their critical current, and to establish limits beyond which irreversible degradation occurs. By addressing these issues, this thesis contributes to determining safe operational limits for superconducting magnets and helps define the machine protection envelope for future high-energy hadron colliders.

This thesis is based on an experimental campaign aimed at identifying the fundamental damage mechanisms in superconducting materials when exposed to high-intensity beam impact. As part of this campaign, a dedicated experiment was conducted at CERN's High Radiation to Materials facility, where the conditions of accidental beam loss were realistically reproduced using proton beam pulses. For the purposes of this thesis, the campaign can be logically divided into four phases. The first phase consists of the preliminary damage experiments [1], [2], which paved the way for the later studies. The second phase comprises of the strand damage experiment, which was analysed prior to this work [3]–[5]. The third phase involves the design, execution and analysis of the coil damage experiment, which is the base of this thesis [6]–[8]. In this experiment, small coil samples made of Nb-Ti and Nb_3Sn strands were exposed to a proton beam with an energy of 440 GeV. Two main aims were to assess whether the damage thresholds identified during previous experiments at the single-strand level remain valid for multi-strand windings and to investigate the interaction between the strands and the epoxy matrix during energy deposition at cryogenic temperatures. The final phase consists of the aged coil damage experiment, which was prepared in the context of this work [9], but was executed by others.

This thesis is structured into two parts. The first one gives the background, general concepts, and preceding work. Although this part is relatively extensive, it is necessary to provide the required multidisciplinary context and to summarise the previous phases of the experimental campaign, which form the foundation of the present work. The second part discusses the author's own work, which is the design and execution of a damage experiment and the interpretation of the results in terms of the estimation of the damage limits resulting from the beam impact.

The first part is divided into four chapters. Chapter 1 introduces the superconducting magnets and their use in particle accelerators. Beginning with the theoretical foundations of superconductivity, it provides an overview of Nb-Ti and Nb_3Sn superconductors. It presents transport current measurements, which were used to characterise the coils before and after the beam impact to quantify any beam-induced degradation. The chapter explains how the dependence on external magnetic field and lattice strain is characterised during these measurements, and concludes with critical current scaling laws, which enable interpolation and extrapolation.

Chapter 2 provides an overview of high-energy particle accelerators, with a particular focus on the CERN accelerator complex. The LHC and its upgrade are discussed in detail to provide context on the technology used for these superconducting magnets.

Chapter 3 explores the mechanisms of beam-induced damage to magnet components. It introduces the physics of particle–matter interactions, which are embedded in simulation codes, enabling the energy deposition of the impacting beam to be modelled. Chapter 4 addresses machine protection strategies and the operational limits of superconducting magnets. The end of this chapter concludes the first part by summarising earlier work on the damage to components of superconducting magnets.

The second part focuses on the author's own work, which comprises three chapters. Chapter 5 discusses the production of the sample superconducting coils. The assembly, winding, and impregnation steps are discussed in detail. It then moves on to the qualification of the samples with respect to their critical current prior to the beam experiment. Finally, the experimental setup is described.

The results of the beam experiment are evaluated in Chapter 6. The procedure during the experiment and the estimation of the beam properties are presented. Defects resulting from the beam impact are identified by means of visual inspection, computer tomography, and metallography, and are used to estimate the trajectory of the beam.

The coil's performance degradation is evaluated using critical current measurements performed after the experiment. These results are then correlated with the simulated material response. The measured beam properties are used as input for calculating the energy deposited in the samples using the FLUKA transport code. This energy is converted into a temperature rise in

the material, and quantities such as the hotspot temperature and the spatial temperature gradient are derived.

The mechanical response of the coils to the beam impact is simulated using ANSYS, and plastic strain in the coils is compared to previous studies. In the pre-last section, the damage limit found for the small sample coils is extrapolated to a full-size accelerator magnet. Finally, the last section outlines the preparation of an experiment in which the Nb_3Sn coils, aged by exposure to a gamma field with a dose of 25 MGy and 30 MGy, were impacted by a proton beam.

Chapter 7 concludes the thesis with a summary and discussion of the damage limits of superconducting magnets in case of impact by high intensity particle beams.

Part I.

Superconducting magnets for particle accelerators

1. Superconductivity

1.1. Overview of theory of superconductivity

Superconductivity forms the backbone of research infrastructures in high-energy physics and quantum computing. However, everyday technologies also rely heavily on the use of superconductivity, for example, in the magnets of magnetic resonance imaging systems. This chapter will introduce the theory of superconductivity by defining quantities such as the critical temperature T_c, the critical magnetic field B_c, and the critical current density J_c. The classification into Low-Temperature Superconductors (LTS) and High-Temperature Superconductors (HTS), together with the classification into Type-I and Type-II superconductors is subsequently addressed.

The treatment will be cursory, and further details on this subject can be found in References [10], [11]. In 1911 Kamerlingh-Onnes discovered that the electrical resistance of mercury vanishes below a critical temperature of T_c=4.2 K when it enters a new state, the superconducting state [12]. Additionally, the material in the superconducting state exhibits the Meissner-Ochsenfeld effect, meaning that it expels an external magnetic field B_{ext} from its interior, except for a thin layer where shielding currents are generated.

The first classical phenomenological model of superconductivity was given by Fritz and Heinz London in 1935. It is based on the Drude model of conductivity in metals [13], where taking the limit of the mean free time between ionic collisions to infinity leads to the two London equations

$$\frac{\partial}{\partial t}\left(\Lambda \vec{J}_S\right) = \vec{E}, \quad \nabla^2 \vec{B} = \frac{1}{\lambda^2}\vec{B} \tag{1.1}$$

where $\vec{J}_S$ is the supercurrent density, and $\vec{E}$ and $\vec{B}$ are the electric and magnetic fields, respectively. The parameters

$$\Lambda = \frac{m_s}{n_s q_s^2}, \quad \lambda = \sqrt{\frac{\Lambda}{\mu_0}} = \sqrt{\frac{m_s}{\mu_0 n_s q_s^2}} \tag{1.2}$$

are the London parameter and the London penetration depth, respectively. They are determined by the mass m_s, number density n_s, and charge q_s of the superconducting carriers, while μ_0 is the vacuum magnetic permeability. The first London equation implies that the current in a superconductor is accelerated by the electric field. The second London equation describes the exponential decay of the magnetic field inside the superconductor with the characteristic scale of the London penetration depth λ.

The transition from the normal conducting to the superconducting state was explained by Ginzburg using Landau's theory of phase transitions [14], for temperature T near T_c and at zero external magnetic field B_{ext}=0. Second-order phase transitions are characterised by the order parameter Ψ where Ψ=0 in one phase (above the critical point, here the normal state) and Ψ>0 in the ordered superconducting state. The magnitude of the Ψ is proportional to the density of superconducting carriers $|\Psi|^2$=n_s. The Ginzburg-Landau (G-L) theory postulates the free enthalpy density of a superconductor as a function of the order parameter and its spatial derivatives. By minimising the free enthalpy near T_c, the behaviour of the Ginzburg-Landau equations is found. The equations define another characteristic length in a superconductor, called the coherence length ξ. This length describes how the density of superconducting carriers n_s scales at the boundary to normal conducting material. The spatial properties of the superconducting state are characterised by the coherence length ξ, describing variation of carriers close to a surface boundary, and the penetration depth λ, penetration of the magnetic field inside the superconductor.

London equations and the G-L theory describe the macroscopic nature of superconductors. The insight into the microscopic process responsible for superconductivity in LTS was explained in the realms of the Bardeen-Cooper-Schrieffer (BCS) theory [15]. It describes the condensation of electron pairs with opposite momentum and spins into Cooper pairs. This implies m_s=2m_e, and q_s=−2e where m_e is the rest mass of an electron and e is the elementary charge. The attraction of electrons arises from their interaction with the crystal lattice, mediated by phonons, of the material. According to the BCS

theory, Cooper pairs in the lowest energy state are separated from the normal conducting state by an energy gap $\Delta(T)$ as a function of temperature T, which is for $T \leq T_c$ given by

$$\Delta(T) = \Delta(0)\sqrt{1 - \frac{T}{T_c}} \approx 1.73 k_B T_c \sqrt{1 - \frac{T}{T_c}} \tag{1.3}$$

where $\Delta(0)$ is the energy gap at absolute zero, proportional to T_c, and k_B is the Boltzmann constant. The relationship quantifies the stability of the superconducting state to be the highest near absolute zero. The observed isotope effect [16], a dependence of T_c on the lattice atomic mass M, supports the involvement of lattice vibrations in the superconducting pairing mechanism, as described by BCS theory.

The coherence length ξ and the penetration depth λ are the basis for the definition of the Ginzburg-Landau parameter $\kappa = \lambda/\xi$. Physically, κ governs the sign of the surface energy σ at a normal–superconducting interface. Type-I superconductors have $\kappa < 1/\sqrt{2}$, $\sigma > 0$, so any boundary between superconducting and normal regions raises the free energy. Thus, the material minimises such interfaces and stays perfectly diamagnetic up to the critical field B_c, and at $B > B_c$ transits to the normal conducting state. Since B_c is typically of the order of a few mT, it makes Type-I superconductors unusable in technical applications [10].

Conversely, for Type-II superconductors $\kappa > 1/\sqrt{2}$, $\sigma < 0$, making it energetically favourable to create many interfaces. They are diamagnetic below the lower critical field B_{c1} and the superconducting state is broken above the upper critical field B_{c2}. When the material enters the mixed (Shubnikov) phase for $B_{c1} < B < B_{c2}$, the magnetic flux penetrates the material in the form of quantized flux tubes, Abrikosov vortices or flux-lines, surrounded by circulating superconducting currents [17]. Each flux-line carries a quantised magnetic flux $\Phi = h/2e$, where $h = 6.626 \times 10^{-34}$ J s is the Planck constant. In Type-II superconductors, the relationship between λ and ξ dictates the arrangement of quantized flux vortices within the mixed state.

Besides the critical temperature T_c and field B_c, the superconducting state is lost if the current running in the material exceeds the critical current density J_c. The applied current density increases the kinetic energy of superconducting electrons, which for $J = J_c$ exceeds the binding energy of the Cooper pairs. Additionally, in Type-II superconductors the flux-lines experience a

Lorentz force $\vec{F}_{\mathrm{L}}=\vec{J}\times\vec{B}$, when current density $\vec{J}$ is being transported along the superconductor. Thermal activation and quantum tunnelling are also known to contribute to vortex motion [18]. If the force is too high, the vortices start to move, leading to energy dissipation and hence the generation of resistance. The flux-flow resistivity ρ_f develops as $\rho_{\mathrm{f}}=\rho_{\mathrm{n}}B/B_{\mathrm{c2}}$, where ρ_{n} is the resistivity in the normal state which induces an electric field below B_{c2} [19]. The movement can be restricted by material defects, impurities, or grain boundaries, which exert a pinning force to hold them in place. These pinning centres enhance the ability of a superconductor to carry large currents in the presence of a magnetic field, a critical property for many practical applications.

Grain boundaries act as natural pinning centres for vortices, so increasing the number of grain boundaries creates more sites for vortex pinning. Grain boundaries are the interfaces between individual crystalline grains, regions where the regular atomic lattice of the material changes orientation or is disrupted. Because these boundaries introduce lattice imperfections and defects, they serve as effective sites where magnetic flux vortices can become pinned, thereby hindering their motion. However, too small grains may introduce defects, reducing overall material quality. The description of thermally activated vortex motion is given by the Anderson-Kim model [20]. According to this model, the electric field induced by vortex movement follows $E \propto E_0 \exp(-U(B,J)/(k_{\mathrm{B}}T))$. The effective pinning energy barrier $U(B,J)$ generally depends on the B and J. This thermally activated process leads to flux creep, which manifests as a slow, gradual movement of vortices and results in a small but finite resistance below the critical current. The effects of temperature, magnetic field, and strain on vortex pinning will be discussed in Section 1.4.

Type-II superconductors are of particular importance for applications due to their ability to sustain superconductivity in high magnetic fields. This property makes them suitable for of high-performance superconducting wires and magnets. The majority of superconductors, used in research and industry nowadays, are based on Niobium, such as Nb-Ti and Nb_3Sn. The two most widely used LTS are discussed in the following section.

1.2. Nb-Ti and Nb_3Sn superconductors

The critical quantities characterising the superconducting state were described in the previous section. While the T_c and B_c are intrinsic thermodynamic properties for each material, the critical current density J_c can be enhanced by means of metallurgical treatment [21]. This section focuses on properties and manufacturing processes of two materials: niobium-titanium (Nb-Ti) and niobium-tin (Nb_3Sn), whose production was mastered in the past to improve their J_c. Superconducting materials for current-carrying purposes are most commonly used in the form of micron-sized filaments embedded in a copper matrix to form a superconducting strand [22]. The focus will be given to the two specific types of strands based on Nb-Ti and Nb_3Sn, which are used in high-energy particle accelerators and will also be further investigated in the practical part of this work.

To understand the motivation for embedding superconducting filaments in a copper matrix, a couple of terms need to be defined first. A quench is the formation of an unrecoverable normal zone within a superconductor, which will transfer the energy supplied by current and energy stored in the magnetic field, in case of a strand wound into a coil, into heat. The minimum propagating zone (NPZ) is the minimum length of a conductor needed for this normal zone to start propagating; for Nb-Ti it is roughly 1 mm [23]. To expand this zone, copper is added, which acts as a stabiliser to conduct current during a quench, because at $T>T_c$ superconductors have a much higher resistivity than copper. The copper also helps to dissipate the heat generated during powering because of its excellent conduction properties.

The ability of a metal to transport the electrical current (and the heat) at low temperatures is governed by electrons rather than by phonons, which dominate at higher temperatures [24]. At zero magnetic field, the resistivity of a metal follows the Matthiessen rule $\rho(T)=\rho_0 + \rho_{lat}(T)$, where ρ_0 is the resistivity caused by electron scattering on impurities and lattice defects and $\rho_{lat}(T)$ is the resistivity from scattering on thermal vibrations. The dependence on scattering can be assessed quantitatively using the Residual Resistivity Ratio (RRR) defined as $RRR=\rho_{RT}/\rho_{T0}$ where ρ_{RT} is the electrical resistivity at room temperature and ρ_{T0} is the resistivity at a temperature close to absolute zero, typically liquid helium temperature. In the context of LTS superconductors, the temperature slightly above the critical temperature $T0=T_{sc}>T_c$ is used. A high RRR value indicates material with low impurity

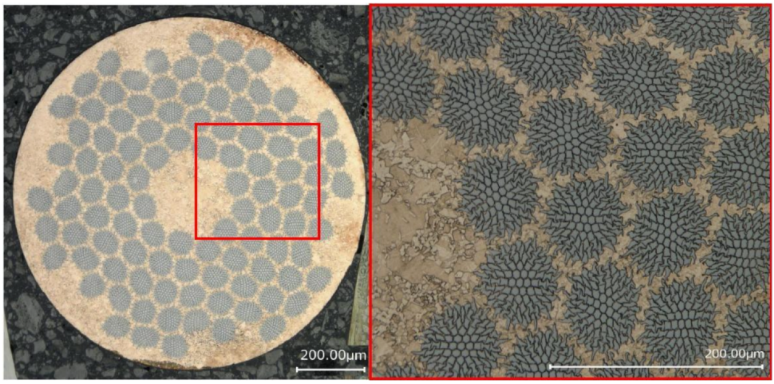

Figure 1.1.: *Left:* Cross section of the studied Nb-Ti strand where the bundles of filaments (grey) embedded in a copper matrix (brown) are visible. *Right:* Zoom on the filaments. Reproduced from [3]

and defect content, resulting in excellent electrical and thermal conductivity at low temperatures. It could be shown that $RRR \propto \sqrt{E_{\mathrm{MQE}}}$ where E_{MQE} is the minimum amount of energy required to quench a local region of the superconductor [25]. The low resistivity and high conductivity of copper make MQE and NPZ larger.

Copper also improves the mechanical properties, protecting the filaments from mechanical stress during manufacturing and handling. The filaments must be twisted with a twist pitch (the length over which the filament makes a full turn) of a few millimetres. This distributes the stresses more evenly and reduces coupling currents within the strand [26]. The filaments are made as small as possible to reduce the volume in which flux lines can move and to limit the eddy currents generated by alternating currents or varying magnetic fields. Small filaments also increase the contact area with the copper, improving electrical and thermal transfer. Generally, to compare superconducting strands with a different diameter, it is best to use the critical current density J_{c}=I_{c}/A, which is defined as the critical current I_{c} divided by the area of the cross-section A.

Nb-Ti outer dipole LHC strand

Niobium and titanium form a solid solution alloy, Nb-Ti, at temperatures above 650 K, where the atoms are randomly distributed on the lattice sites. It is the most widely used superconductor today. Nb-Ti emerged as the preferred material due to its favourable mechanical properties compared to other materials such as Nb_3Sn, which has a higher T_c but proved to be brittle and difficult to process [27]. The superconducting properties of the alloy are highly dependent on the stoichiometry: B_{c2} exhibits a sharp peak when the titanium weight content is between 40 % and 50 %, whereas the critical temperature undergoes a much smaller variation, peaking at a titanium content of 25 % [28]. The most common commercial standard Nb-Ti alloy has a composition of 47 % titanium [29]. The Nb-Ti alloy has two stable phases: the superconducting precipitate β-Nb-Ti phase and the resistive α-Ti phase, which enhances the superconducting critical current by acting as flux pinning centres below T_c.

The Nb-Ti strand studied in the practical part of this thesis is identical to those used in the dipole magnets of Large Hadron Collider, details about the different accelerator and magnet types is given in Section 2.3. The strands are made from Nb-Ti ingots produced by melting niobium and titanium. A layer of niobium and copper is welded around the ingot, and long hexagonal monofilaments are formed by drawing and extrusion. The monofilaments are stacked and surrounded by a copper tube. The complete strand is heat treated at temperatures of 650 K and 700 K, where the diffusion of titanium allows the formation of the α-Ti phase [27]. Heat treatment and drawing processes are carried out in such a way as to achieve the optimum size and spacing of the α-Ti precipitates.

The final cross-section of the strand is shown in Figure 1.1. It features polyimide insulation and has a diameter of 0.825 mm and a copper to superconductor volumetric ratio (Cu/SC) of 1.95 [30]. The superconducting filaments have an average diameter of 7 µm and there are thousands of them in the cross-section of the strand. The filaments are braided with a twist pitch of 15 mm. The strand has a T_c of about 9.2 K and an upper critical field at 0 K, $B_{c2,0}$, of about 14.5 T. The properties of the strand are summarised in Table 1.1. In the LHC dipole coils, 36 of these insulated strands are braided to form a Rutherford cable, which is the most effective cable geometry, prevent-

Strand	Diameter (mm)	Cu/SC	Filament size (μm)	$T_{c,0}$ (K)	$B_{c2,0}$ (T)	I_c (A)
Nb-Ti	0.825	1.95	6	9.2	14.5	>410*
Nb_3Sn	0.85	1.2 ± 0.1	<55	18	25	>632**

Table 1.1.: Characteristics of the Nb-Ti and Nb_3Sn strands utilized in the experimental campaign (sourced from [30] and [33]). * at 6 T external field and 4.2 K, ** at 12 T external field and 4.2 K.

ing uneven current distribution and minimising electromagnetic coupling effects.

Superconducting magnets were applied in an accelerator in the Intersecting Storage Ring (ISR) for the first time in 1983 [31]. The ISR was the world's first hadron collider. The first project to use Nb-Ti on a large scale was the Tevatron at Fermilab, United States. Since then, it has become the state of the art for high-energy particle accelerators such as the LHC dipole magnets based on the Nb-Ti strands which can reach an ultimate field of 9 T [32]. In addition to particle physics, Nb-Ti is also widely used in other technologies that rely on strong magnetic fields, such as medical MRI systems and fusion research magnets. While the technology can generate fields up to around 10 T, achieving higher fields requires the use of alternative superconducting materials.

Nb_3Sn HL-LHC inner triplet strand

The brittle intermetallic compound Nb_3Sn exhibits superconductivity at tin contents between 18 % and 25 % atomic percent, where it forms a cubic A15 lattice. Various techniques exist to produce a Nb_3Sn strand, but the most advanced technology today is the Restacked Rod Process® (RRP), which is also the type of process used for the strand investigated later in this thesis. The first Nb_3Sn strands were made by the Bronze Process method, similar to how the Nb-Ti strands are produced, as discussed above. During the Bronze Process method, the monofilaments are composed of a niobium core surrounded by a α-bronze (Sn solid solution) sheath. These hexagonal monofilaments are embedded in a α-bronze matrix with a diffusion barrier, either Nb or Ti, and a high-purity copper matrix around it. The diffusion barrier prevents contamination of the copper with tin, which would degrade the electrical and

thermal conductivity of the strand. The α-bronze lowers the Nb_3Sn formation temperature but reduces the RRR of the strand and has a tendency to deform plastically during drawing.

The RRP is a special type of internal tin process in which hexagonal monofilaments consisting of a niobium core and copper jacket are stacked in a copper matrix with copper and niobium diffusion barriers. The centre is filled with copper, which is subsequently drilled out and filled with tin to form a sub-element. The sub-elements can be stacked in various ways, but the HL-LHC quadrupole type utilizes the 108/127 geometry, meaning that the grid with 127 positions out of which 108 are filled with sub-elements and the remaining 19 positions in the centre of the strand are filled pure copper (see Figure 1.2). In addition, some sub-elements are replaced with tantalum to improve flux pinning capabilities, which effectively improves the B_{c2} [34].

The Nb_3Sn strand must be heat treated to form the superconducting A15 phase from the constituents. The reaction temperatures and times for the HL-LHC quadrupole strand, are 215 °C for 48 h, 400 °C for 48 h and 665 °C for 50 h, with ramps at 25 K h^{-1} to 215 °C, 50 K h^{-1} to 400 °C, and 50 K h^{-1} to 665 °C.

After heat treatment, the reacted Nb_3Sn strand is very fragile, and its use in an accelerator magnet could be risky because it can move under electromagnetic forces that could be harmful for the strand. To prevent this, the strand or the entire winding of the magnet is impregnated [35]. This means soaking the winding with a resin to improve its mechanical and thermal properties. This ensures that the strands are well supported, reducing the risk of damage during thermal or electromagnetic cycles. The impregnation process is usually carried out in a vacuum chamber to ensure complete filling and bonding of the strand to the neighbouring sections. The difference between the final heat-treatment temperature at 938.15 K and operating temperature at usually around 4 K or below and the fact that the copper, Nb_3Sn, and niobium have a different thermal contraction, leads to mechanical stresses.

The 108/127 RRP HL-LHC quadrupole strand has a diameter of 0.85 mm with a Cu/SC of 1.2±0.1. The filament size is of 55 µm with a twist pitch of 19±3 mm. The strand has a T_c of about 18 K and a $B_{c2,0}$ of about 25 T. The strand used in HL-LHC quadrupole is insulated with AGY S2 glass fibre, and 40 of these strands are braided together to form a Rutherford cable. The cabling of the brittle strands leads to degradation in critical current and RRR, but could be optimised [36], [37]. Table 1.1 summarises the properties of the

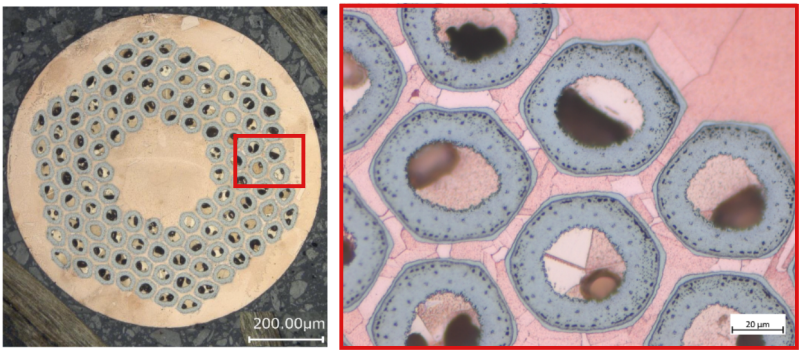

Figure 1.2.: *Left:* Cross section of the Nb_3Sn HL-LHC RRP strand after the heat treatment. The superconducting filaments embedded in the copper matrix are nicely visible. *Right:* Zoom on the superconducting filaments showing the Nb_3Sn phase (dark grey rings). Reproduced from [3]

HL-LHC quadrupole Nb_3Sn strand compared to the LHC outer dipole Nb-Ti ones discussed above.

1.3. Transport current measurements

This section outlines transport current measurements, which are considered the most versatile method for determining superconducting properties [38]. The measurement procedure is described and compared to other techniques used to qualify a superconductor's performance. The definition of different criteria for the definition of I_c, as well as the role of self-field correction of transport current measurements, is described.

The transport current measurement involves applying a current I through the superconductor at a temperature below its critical temperature T_c and measuring the resulting voltage U along its length. The voltage is measured using voltage taps, typically thin, insulated, and twisted copper wires soldered to the superconductor. The I-V curve exhibits a small sloped baseline, as the transport current entering the conductor through the resistive matrix and redistributes into the superconducting filaments over a characteristic current transfer length. If the voltage taps are located too close to the current contacts, the resistive voltage generated during this current redistribution

can appear in the measured signal. A rapid increase in the voltage is observed as the current approaches the critical current I_c, resulting from the thermally activated flux motion as discussed in Section 1.2.

Alternative techniques, such as magnetisation measurements, induce eddy currents generated by a varying magnetic field. Notably, the critical current estimated from the two techniques often differs [38]. Magnetisation measurements provide a volumetric average of the critical current, making them suitable only for small, uniform samples if high precision is required. In contrast, transport current measurements are sensitive to the weakest point in the strand, as the measured critical current is limited by any local bottleneck.

The critical current I_c can be extracted from the I-V curve using several methods, namely the electric field criterion, the resistivity criterion, or the offset criterion. The electric field criterion involves dividing the measured voltage by the distance between the voltage taps d to obtain the I-E curve, where E represents the electric field. Empirically, the relationship between I and E is described by

$$U(I)/d = E(I) = mI + E_c \left(\frac{I}{I_c}\right)^n , \tag{1.4}$$

where m is the Ohmic resistance and the parameter n characterises the sharpness of the superconducting transition. The parameter n is related to the activation energy of flux motion relative to the thermal energy. The above relation defines I_c as the current at which the electric field intercepts E_c. The value of E_c commonly used in the literature is either E_c=0.1 µV cm^{-1} or E_c=1.0 µV cm^{-1} [39].

The critical current of a conductor is dependent on the magnetic field in which the measurement is conducted. This dependency is used to reduce the critical current, thereby preventing the use of excessive currents during the measurement. Additionally, for the evaluation of measurements, the self-field generated by the strand or coil has to be taken into account. The amount of the magnetic field generated by a long straight wire carrying current I with a radius of r is derived from Ampère law for a long straight conductor B=$\mu_0 I/2\pi r$. For the superconducting strand with multi-filament geometry, the self-field generated in the outermost filament region, where the maximum B is observed, is taken into account [40]. In the case of the Nb_3Sn RRP strand,

the outermost layer is located at a distance of 0.375 mm. Therefore, the self-field can be approximated as $B_{self}=CI_c$ of $C=0.533\,T\,kA^{-1}$ must be added to the external magnetic field B_{ext} to obtain the total magnetic field B.

Sections 2.2, 2.3 will discuss the pre-stress that needs to be applied during the assembly of superconducting coils to combat the Lorentz stresses that occur during operation. The variation of I_c in LTS strands when subjected to mechanical strain can be derived from transport current measurements [41]–[45]. The critical current can be evaluated at different axial or transverse strain levels. This is helpful when designing superconducting magnets. The resilience of the Nb-Ti conductors, compared to Nb_3Sn, against strain will be discussed in the following.

Resistance of Nb-Ti to mechanical strain

The effect of different mechanical strains on I_c in a multi-filamentary Nb-Ti strand was experimentally measured at both cryogenic and room temperatures [41]. It was shown that, the strands can withstand axial strains of 2 % to 3 % with only slight degradation of I_c. The strain affects the B_{c2} and pinning, which become more critical at high magnetic fields. Transverse compressive stress has a reversible effect, with loads of 0.6 GPa temporarily lowering the I_c by less than 5 %. During the same campaign, a hairpin bend was performed at room temperature, and a very large bending resulted in almost no deterioration of I_c. Overall, transverse stress tends to degrade the conductor more strongly than axial stress. It was reported that, while the sample was held under a constant applied strain corresponding to a tensile stress of ~0.85 GPa, a thermal runaway occurred. The transient heating during this event partially annealed the conductor, redistributing the internal stress without altering the imposed strain. Following this stress redistribution, the measured critical current increased. This observation suggests that the superconducting performance of NbTi is strongly influenced by the internal strain state of the filaments. Stress relaxation processes, such as those occurring during thermal annealing, can modify this strain state and thereby improve the measured critical current. The author of [41] further suggests that targeted stress-relief treatments, such as controlled stress annealing, may offer a means to restore or enhance the performance of Nb-Ti conductors after mechanical loading.

Sensitivity of Nb_3Sn to mechanical strain

The performance of the Nb_3Sn strands can be modified in various ways. The influence of heat treatment and cabling on the I_c and RRR was discussed in Section 1.2. The brittle nature of Nb_3Sn and the relatively large size of filaments inside the RRP strands make it more prone to damage from strain. The dependence of I_c on axial strain ε_a is commonly characterised using a Walters spiral apparatus [46]. In this method, a strand is soldered onto a spring, and a tensile or compressive strain is induced by twisting the spring. Strand is usually strained in the axial direction, unloaded back, and measured for transport current. Up to a certain point the strain compensates the intrinsic compressive pre-strain, which improves the I_c. Beyond the strain corresponding to the maximum I_c further strain leads to a reversible degradation until the irreversible strain limit ε_{irr} is reached.

It was found that, for the Nb_3Sn which was discussed earlier (See Section 1.2), the I_c is reversible in range -0.25 %<ε_a<0.46 % [47]. The same strand was confined in a U-shaped groove and impregnated with the epoxy. The degradation is reversible until stress of ~175 MPa. The impact of transverse stresses is lower when the strand is impregnated with epoxy [42]. The epoxy distributes load and reduces local point contact stresses, thereby reducing the transverse stress affecting the strands directly. The response of the RRP strands to the stress applied in the transverse direction is also affected by the initial axial strain state of the strands [45]. During X-ray tomography measurements, the plastic deformation of the copper matrix was identified as the main damage mechanism of HL-LHC inner triples strands subjected to transverse load [48].

During transport current measurements, mechanical loading can be applied either in the axial or the transverse direction. These measurements are important for the mechanical design of LTS-based coils, as in the simulation, it is possible to make assumptions about the stress direction. However, if a coil is impacted by a particle beam, the strain develops in a timescale of μs due to heating.

The strain-induced degradation of I_c in Nb_3Sn can be reversible or permanent. The reversible degradation is caused by distortion of the crystal lattice, which modifies the electronic band structure and thus affects superconducting parameters. This degradation vanishes upon relaxation of the lattice. If the copper matrix deforms under the applied stress, it permanently changes the

stress state of the filaments. Those two effects will alter the B_{c2}, which results in a change in I_c. If the applied stress is even higher, the filaments start to break, which lowers the effective cross-section of the strand. The filament breaking lowers I_c leaving B_{c2} unaltered.

1.4. Critical current scaling laws

The determination of I_c using transport current measurements was described in the previous section. This section will discuss how I_c depends on external parameters such as the temperature T, magnetic field B, and the strain ε in superconducting strands. Critical surface J_c-B-T represents the boundary between the superconducting and normal states. The material is superconducting below the critical surface and normal conducting above it. The Nb_3Sn surface lies above that of Nb-Ti, indicating that Nb_3Sn remains superconducting at higher temperatures, magnetic fields, and applied currents simultaneously. Nb_3Sn strands exhibit a strong vulnerability of I_c on mechanical strain. Characterizing I_c therefore involves qualifying the conductor as a function of T, B, and ε. From a discrete set of measurements, the critical surface can be determined using a scaling law that allows interpolation and extrapolation of the data. The dependence of I_c on the magnetic field and temperature is discussed first.

The influence of the magnetic field on the critical current is significant, with a field of 20 T reducing the critical current in a Nb_3Sn strand from thousands to tens of amperes. The relationship between B and I_c is governed by magnetic vortex pinning as described in Section 1.1. When the Lorentz force acting on vortices exceeds the pinning force, the vortices begin to move. Thus, an effective de-pinning field $B^*_{c2} < B_{c2}$ is defined as the field at which I_c drops to zero due to the loss of pinning. Since $B^*_{c2} \approx B_{c2}$ in low-temperature superconductors (LTS) [38], the distinction between the two will be omitted hereafter. According to pinning theory [49], the critical Lorentz force F_L per unit length is given by

$$F_L = I_c B = k f(b) = k b^p (1-b)^q, \tag{1.5}$$

where b=B/B_{c2} is the reduced magnetic field, k is a constant, and $f(b)$ is a general pinning function. The empirically derived constants p and q are

almost independent of temperature and strain and determine the shape of $f(b)$, p in the low field regime and q in the high field regime [38]. The form of Equation 1.5 holds for superconductors with strong flux pinning like Nb-Ti and Nb_3Sn. The function $f(b)$ exhibits a maximum at parameter b equal to $\approx$0.6 over a wide range of temperatures.

The critical current of LTS strands exhibits a dependency on mechanical strain, a phenomenon of particular importance for accelerator magnet applications, where Lorentz forces can impart high stresses. In practice, the three-dimensional stress state within a strand is decomposed into axial stress, parallel to the strand's length, and transverse stress, acting across its cross-section. Axial tensile or compressive strain, which is the result of the stress, modifies the lattice parameters [50], and thus induces a change in the phonon spectrum, leading to significant changes in the critical superconducting parameters.

From the above-described theoretical and empirical findings, it is possible to deduce semi-empirical scaling laws, different for different materials, representing the critical surface in one analytical expression. These can be used to interpolate and extrapolate measured data.

Bottura scaling for Nb-Ti

The critical surface of Nb-Ti-based superconductors can be approximated using the Bottura scaling law [51]. Assuming a fixed temperature $T<T_c$ and neglecting strain effects, the critical current density can be expressed as

$$J_c(B) = \frac{C_0}{B} b^{0.57} (1-b)^{0.9}, \tag{1.6}$$

where $b=B/B_{c2}$ is the reduced magnetic field and C_0 is a scaling constant. For the LHC outer dipole strand (see Table 1.1), the values B_{c2}=14.5 T and $T_{c,0}$=9.2 K are assumed. Using C_0=27.04 T together with the exponents p=0.57 and q=0.9 provides a good description of the measured data. The Bottura scaling law reproduces the critical current density with an accuracy on the order of 5 % or better for magnetic fields above 1 T [51].

Extrapolative Scaling Expression for Nb_3Sn

Data from thousands of transport current measurements of different Nb_3Sn strands were used to define an Extrapolative Scaling Expression (ESE), which enables accurate extrapolation of limited data to predict how the critical current behaves under varying magnetic field, temperature, and strain [52]. It is based on the observation that the shape of the general pinning function remains unchanged as long as the dominant pinning behaviour is preserved.

Assuming that the pinning behaviour remains unchanged, that the strain dependence can be neglected, and that measurements are performed at a fixed temperature $T<T_c$, the critical current can be expressed as

$$I_c(B) = C^* \, b^{-1/2}(1-b)^2, \tag{1.7}$$

where $b=B/B_{c2}$ is the reduced magnetic field, with B_{c2} being the upper critical field at the given temperature, and C^* is an effective scaling constant. This expression corresponds to Kramer-type pinning, where grain-boundary pinning dominates in Nb_3Sn strands [53], leading to the characteristic exponents $-1/2$ and 2. It allows the determination of both C^* and B_{c2} from the linear relation

$$I_c^{0.5} B^{0.25} \propto (1-b),$$

which provides a good fit in the region $0.2<b<0.6$. Outside this range, deviations may occur due to changes in pinning behaviour or proximity to the critical limits. However, extracting B_{c2} from low-field data (typically in the range 12 T to 15 T) can lead to an overestimation of up to 3 % [54].

2. High-energy particle accelerators

2.1. The CERN accelerator complex

The European Organisation for Nuclear Research (CERN) operates a chain of particle accelerators that deliver high-energy proton beams for both collider and fixed-target experiments. Accelerators can be divided into two groups: LINear ACcelerators (LINACs) and circular ones. The CERN accelerator complex (see Figure 2.1) can accelerate either electrons, protons and ion nuclei, most often lead ions. In the following, only proton beams will be treated.

The production of the proton beam is as following. H^- ions coming from a plasma ion source are accelerated through a series of radiofrequency cavities

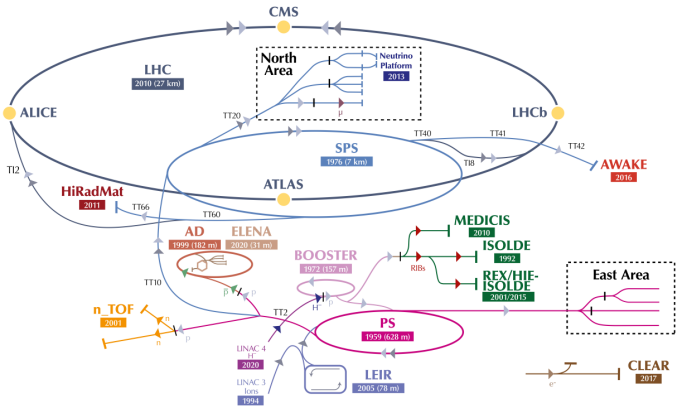

Figure 2.1.: Schema of the CERN accelerator complex. Adjusted from [55].

at LINAC4 linear accelerator, boosting them to an energy of 160 MeV over 86 m. The Proton Synchrotron Booster (PSB), the first circular accelerator in the chain, has a diameter of 50 m and consists of four rings which are stacked on each other within a single aperture. The two electrons from H^- are stripped during injection from LINAC4 to PSB using a stripping foil and consequently accelerated to 2 GeV.

The PSB is a synchrotron where accelerating RF cavities generate a longitudinal oscillating electric field to accelerate protons while the magnet current is ramped to adjust magnetic field strength, keeping pace with the increasing proton energy. A particle with charge q and velocity $\vec{v}$ in presence of electromagnetic field is experiencing the Lorentz force $\vec{F_L}=q(\vec{E}+\vec{v}\times\vec{B})$, parallel to the electric field $\vec{E}$ and perpendicular to the particle velocity $\vec{v}$ and magnetic field $\vec{B}$. In order to keep particles on the circular path, strong magnetic fields need to be used. These are generated either by normal conducting electromagnets or superconducting magnets, *e.g.* wound from the LTS strands discussed in Section 1.2, which can withstand very high currents (see Table 1.1). The bunched structure of the beam is introduced in the PSB, where six bunches are created from the four rings. The PSB was commissioned in 1972 to allow more protons to be injected from LINACs into the following accelerator, the Proton Synchrotron (PS), which has been in operation since 1959 [56]. With a circumference of 628 m, the PS has 100 normal-conducting magnets. The six bunches that arrive from the PSB are split first into 18 bunches and then into 72 bunches, with a spacing of 25 ns.

The Super Proton Synchrotron (SPS), with a circumference of 6.9 km, has been in operation since 1976. Particles from the PS are sent to SPS, where they are accelerated to energies up to 450 GeV. There are 1317 room-temperature electromagnets, including 744 dipoles for bending. The SPS was used as $p\overline{p}$ (proton-antiproton) collider in the past. To date, the main usage of the SPS is to supply beams for the Large Hadron Collider (LHC), but protons can also be sent to fix target experiments. One example is the HiRadMat facility, where beam-matter experiments are conducted. For safety reasons, protons to be injected into LHC are accelerated to 450 GeV while the energy of the proton beams sent to HiRadMat is 440 GeV. The different energies are a consequence of destinations being categorised by energy.

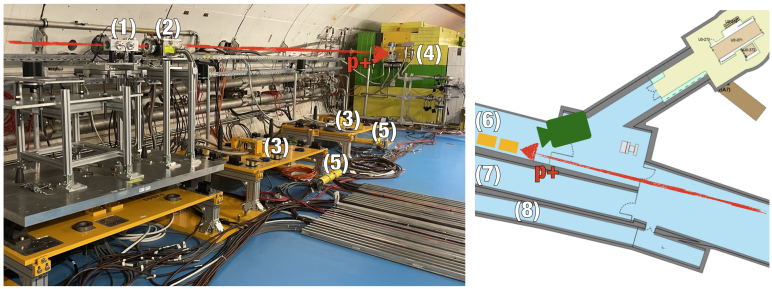

Figure 2.2.: *Left:* Photo of the HiRadMat tunnel, looking at the last part of the beam line, where beam diagnostic devices [BPKG (1), BTV (2)], experimental tables (3), the beam dump (4) and beam loss monitors (5) are visible. *Right:* Schematic view of the different tunnels in the HiRadMat facility: TNC tunnel (6) with experimental tables (yellow rectangles), access tunnel TT61 (7) and tunnel TI2 (8) connecting the SPS and the LHC. The green camera logo indicates the position from which the photo on the left side was taken and the red arrow shows the trajectory of the proton beam.

HiRadMat facility

The experiment discussed in this work was conducted in HiRadMat, a High Radiation to Materials facility at CERN [57]–[59]. HiRadMat (see Figure 2.2) is located in a tunnel branching off from the SPS main tunnel and is linked to the SPS by a beam transfer line. A parallel tunnel is available to house radiation-sensitive equipment, while an access tunnel allows material and personnel access to the experimental area. This area features multiple experimental tables, on which experiment-specific equipment can be installed. A beam dump is located downstream of the experimental tables.

A variety of proton and ion beams can be requested, either single bunches or multi-bunch trains (with bunch numbers as multiples of 12) with a bunch spacing of 25 ns which is the same beam structure as the one used for the LHC physics beams. A 440 GeV proton pulse of up to 288 bunches/pulse with 2.1×10^{11} protons per bunch can be delivered, making HiRadMat a fixed target experiment with the highest energy on Earth. This allows users to request the beam with the desired properties for their experiments. The first experiments in the now-called HiRadMat facility were to test the collimators for the LHC [60], and since then, it has been pushing the frontiers of beam-to-material physics.

HiRadMat is equipped with a variety of beam instrumentation devices used to measure properties of the experimental beams, as shown in Figure 2.2. A Beam TeleVision monitor (BTV), installed upstream of the experimental tables, measures the transverse beam profile and centroid [61] by imaging light emitted from a scintillating screen. Upstream of the BTV, a Beam Position Monitor (BPKG) determines the beam position from signals induced on symmetrically arranged electrodes. Bunch-by-bunch intensity is measured non-invasively using a Beam Current Transformer (BCT), which converts the beam current into an electrical signal proportional to its intensity [62]. The beam line is also equipped with LHC-type Beam-Loss Monitors (BLM), ionization chambers filled with nitrogen that detect secondary particles from beam losses [63]. Additionally, a polycrystalline chemical vapor deposition (pCVD) diamond detector can be installed to provide detailed bunch-by-bunch intensity and structure measurements [64]. These devices enable users to assess beam quality and accept or reject the beam accordingly.

2.2. The Large Hadron Collider

The LHC has been in operation since 10 September 2008, when the first proton beams circulated in the machine. Protons from the SPS are injected into the LHC, where they are accelerated to energies of up to 6.8 TeV. The LHC is also capable of accelerating heavy ions to energies up to 2.56 TeV per nucleon. The LHC is 50 m to 100 m below the ground and has a circumference of 26.7 km [65]. The LHC is a collider, so protons circulate in the LHC in both clockwise and counter-clockwise directions, colliding head-on at four Interaction Points (IP) in the LHC ring, where the main experiments are based. These are two general-purpose experiments, ATLAS and CMS, which discovered the Higgs boson in 2012 [66], [67]. The ALICE experiment focuses on ion-ion collisions, while the LHCb experiment investigates the origin of the matter-antimatter asymmetry in the universe by studying the decays of mesons containing beauty quarks. In addition to the four straight sections used by the experiments, two of the remaining four straight sections are dedicated to beam cleaning, one hosts the RF cavities, which accelerate the beam, and one houses the beam dumping system, which is required to safely extract the two beams. The eight straight sections are connected with eight nearly identical arc sectors, where the majority of the magnets required to steer the particle trajectories are located.

The total number of events produced for a given process over the duration of an experiment is determined by the integrated luminosity $L_{\text{int}}=\int \mathcal{L}\, dt$, which represents the time integral of the instantaneous luminosity $\mathcal{L}$. For a process $A \rightarrow B$ characterised by a cross section $\sigma_{A\rightarrow B}$, the expected number of events N is given by $N=L_{\text{int}}\, \sigma_{A\rightarrow B}$. In a collider with Gaussian transverse beam profiles, the instantaneous luminosity can be expressed as

$$\mathcal{L} = f_{\text{rev}} \frac{N_1 N_2 n_{\text{b}}}{4\pi\sigma^2} = f_{\text{rev}} \frac{N_1 N_2 n_{\text{b}}}{4\varepsilon\beta^*}, \tag{2.1}$$

where f_{rev} is the revolution frequency, N_1 and N_2 are the number of particles per bunch in each beam, and n_{b} is the number of bunches per beam. The quantity σ denotes the transverse RMS beam size at the interaction point. Under the assumption of negligible dispersion and round beams, the second equality in Equation 2.1 follows from

$$\sigma = \sqrt{\varepsilon\beta^*}, \tag{2.2}$$

where ε is the geometric transverse emittance and β^* is the value of the betatron function at the interaction point. The β function is determined by the machine optics, mainly the quadrupole magnet configuration. The emittance ε is proportional to the area in the momentum-position phase-space. It is a constant if the energy of the beam is constant and under the assumption of only conservative forces acting on the beam. The normalised emittance $\varepsilon_{\text{n}}=\varepsilon\beta_{\text{rel.}}\gamma$ is introduced by multiplication of ε by relativistic velocity $\beta_{\text{rel.}}$ (velocity in units of light-speed c) and relativistic factor $\gamma=E/E_0$ (ratio of total E to rest-mass energy E_0).

The LHC was designed to store up to 2808 bunches, each containing 1.15×10^{11} protons. This yields a stored energy of 360 MJ per beam. During the year 2025 the stored energy per beam reached 457 MJ. Section 4 discusses the risks associated with the enormous beam energy and how some of this energy can be dissipated in a superconducting magnet.

Accelerator magnets are classified by their cylindrical multipole order, which describes how the magnetic field varies around the beam axis in the transverse plane. Dipole magnets (first-order multipoles) provide a uniform field that bends the particle trajectory. Quadrupole magnets (second-order multipoles) focus the beam in one transverse direction while defocusing it in the other.

Sextupole magnets correct for chromatic aberrations in the quadrupole focusing due to the finite momentum spread of the beam. There are also magnets with higher numbers of poles that correct the higher-order deviations.

Each of the four large LHC experiments is equipped with a pair of inner triplets, arrangements of three quadrupole magnets installed symmetrically around the interaction point. These triplets focus the beam strongly in both transverse directions, lowering the beam size at the collision point to maximize luminosity. The triplets are also designed to match the beam optics between the interaction region and the surrounding accelerator arcs.

LHC dipole magnet

The LHC is composed of 1232 superconducting twin-aperture dipole magnets, which fill more than two-thirds of its circumference. These magnets have a length of 14.3 m and operate at 1.9 K [68]. To follow the curved trajectory of the beam, the magnets are curved with a sagitta of almost 1 cm.

Superconducting magnets need to be trained by gradually increasing the magnet's current to its operational level, which is one of the main disadvantages compared to normal-conducting magnets. During the first powering cycles, the magnets quench at lower currents, which releases energy and causes local heating and minor structural adjustments within the magnet [69]. Through repeated cycles of quenching, the magnet's performance stabilises, allowing it to reach its intended operational current without further quenching. This depends on the type of winding. For an LHC dipole magnet, it can take up to several days to reach the nominal current. Therefore, ongoing research aims to understand the processes during the training that can help to minimize or eliminate it.

Magnets operating in the superconducting regime can be easily quenched if a relatively small energy (in the order of $1\,\mathrm{mJ\,cm^{-3}}$) is lost from the circulating beam to the magnet coils [25]. The beam losses could be classified into two types. Continuous (steady-state) losses occur whenever the accelerator stores the beam, which then collide at the interaction points and produce collision debris. Simultaneously, the beam interacts with the beam pipe or with remaining gas molecules inside it. Finally, it emits synchrotron radiation (see Section 3.1). The second type of beam loss is accidental, occurring, for example, due to a sudden magnet power failure. Some failure cases relevant

for this thesis will be detailed in Section 4. Both continuous and accidental beam losses can damage the accelerator and lead to unwanted downtime. To prevent this, a collimation system was designed to protect the machine from both types of losses. It serves as the first line of passive defence, guiding and absorbing stray particles at predefined locations around the machine.

Injection and extraction

Each accelerator has a limited dynamic range of energies in which it can operate, which is the main reason why a chain of accelerators is required to reach TeV-scale energies (see Figure 2.1). The beam which is injected from the preceding machine, must have properties suitable for both machines; furthermore, the emittance of the beam is defined in the early stages of the acceleration, and therefore, if the beam is injected wrongly, the emittance cannot be further reduced.

To inject or extract the beams from the ring, an interplay of three types of magnets is used. Septum magnets are pulsed or DC dipole magnets with a field-free region (area of the circulating beam) and a high field region (area of the injecting beam). The septum injects the beam onto the closed orbit in the centre of the kicker magnet. Kicker magnets are pulsed dipole magnets with fast rise time (below 0.1 μs), which allows them to deflect particles into or out of the main ring. The kicker magnet compensates for the remaining angle after the septum. A defocusing quadrupole is placed before the kicker to defocus the circulating beam in the given plane and thus reduce the required strength of the kicker. Malfunction of any of these components can cause loss of the injected (or extracted) beam into the machine aperture, as will be further discussed in Section 4.

2.3. The High-Luminosity LHC upgrade

The High Luminosity Large Hadron Collider (HL-LHC) is an upgrade to the LHC, which will extend its physics potential by increasing the integrated luminosity per year by one order of magnitude [70]. The current Nb-Ti magnets are not capable of producing field above 10 T as discussed in Section 1.2. A modification to the inner triplet regions surrounding the ATLAS and CMS experiments will involve incorporating Nb_3Sn quadrupole, for the first time

in a particle accelerator. In addition to the new magnets, the installation of superconducting crab cavities is planned. Furthermore, the LHC experiments will upgrade their detectors to cope with the increase in the mean number of collisions per bunch crossing from 60 up to 200 [71].

HL-LHC final-focusing quadrupole magnet

The increase of the bunch intensity in the HL-LHC will be achieved by upgrading the inner triplet region with Nb_3Sn quadrupoles with larger apertures and high magnetic field gradients. This will allow for a significant reduction of the beam size at the interaction points. The peak field will increase to 11.4 T from 8.6 T reachable with the LHC quadrupoles. The triplets will be wound with a Rutherford cable composed of 40 Nb_3Sn RRP 108/127 strands (described in Section 1.2), while a strand based on Powder-in-Tube technology with a lower J_c but favoured for its mechanical robustness compared to RRP was also considered.

The winding of new inner triplet consists of 50 turns in two layers with a winding tension of 25 kg. The binder CTD-1202 is applied to the S2 glass insulation of the strands, and the curing of every layer for several hours at temperatures below 170 °C is performed. The curing stabilises the coil geometry before the next step. The complete winding is heat-treated in a mould with the temperature profile described in Section 1.2. Following the heat treatment, the voltage taps are added together with quench heaters. Finally, the coil is inserted into an impregnation mould and subsequently placed into a vacuum tank for impregnation with CTD-101K epoxy [72].

Impregnated coils of an HL-LHC inner triplet quadrupole are surrounded by an aluminium collar pre-loaded using bladder and key technology, and embedded in a laminated iron yoke. Half of the axial compression is provided by welding the stainless steel outer shell, and the other half by inserting load keys into inflatable bladders. The entire coil, yoke, and support assembly is housed inside a stainless steel helium vessel cooled to 1.9 K. Metallurgical inspection was performed on a coil prototype after cold power tests [73]. The coil are cut open with a diamond cutting wire, polished, and examined with an optical microscope. Shrinkage cavities and metal-to-metal cracks were observed. Section 4.2 discusses the evolution of the properties of CTD-101K epoxy under radiation.

3. Interaction of particles with matter

3.1. Physics of particle-matter interaction

The first part of this chapter describes how particles interact with matter, focusing on particle showers which transfer energy from the beam to the material and can alter its properties. The effect of the rapid beam heating and the resulting deformation is also mentioned. The following section begins with a discussion of failures that can lead to an impact of a high-energy, high-intensity beam in a superconducting magnet. A summary of previous studies on magnet component damage closes this chapter.

As a particle passes through matter, it can be deflected from its original path, transfer energy and create shower particles, or damage the structure of the material. When dealing with particle interactions, it is useful to classify particles according to their charge and rest mass. The electrons and positrons with a rest mass of 511 keV are considered light, and particles with a higher rest mass are considered heavy. Collisions can be elastic, where all the kinetic energy is conserved, resulting only in a change of direction, or inelastic, where some of the energy is transferred to the target, causing effects such as excitation, ionisation, or, if the energy transfer is sufficient, it can alter the structure of the target material. On a macroscopic scale, there are many inelastic interactions and the fluctuations in the total energy loss are small [74]. It is therefore useful to define the average energy loss per unit path length $\left\langle \frac{dE}{dx} \right\rangle$, also called the stopping power [75].

The formula for the stopping power of a heavy charged particle was first derived by M. Born [76]. Later, H. Bethe and F. Bloch derived a quantum mechanical formulation [77], [78]. Born's equation is based on an impact parameter, which is not measurable, whereas the Bethe-Bloch formula is

based on the measurable momentum transfer. The average rate of energy loss from heavy relativistic charged particles is

$$-\left\langle \frac{dE}{dx} \right\rangle = Kz^2 \frac{Z}{A} \frac{1}{\beta_{\text{rel}}^2} \left[\frac{1}{2} \ln \frac{2m_e c^2 \beta_{\text{rel}}^2 \gamma^2 T_{\text{max}}}{I^2} - \beta_{\text{rel}}^2 - \delta - 2\frac{C}{Z} \right], \tag{3.1}$$

where the constant K has a value of 0.1535 MeV cm^2 s^{-1}, z is the charge of the incident particle in units of the elementary charge e. Z (A) is the proton (nucleon) number of the target material. When this equation is derived, the integral over the possible energy transferred to the atomic electrons is performed, and then T_{max} is a cut-off parameter indicating the maximum energy transfer per collision. I is the average energy required to ionise an atom. The quantities δ and C are corrections that are important at high and low energies, respectively. The formula is accurate to within a few per cent for intermediate Z materials in the $\beta_{\text{rel}}\gamma$ range between 0.1 and 1000 [79].

The ionising energy loss depends on the speed of the particle and not directly on its mass, besides T_{max}=$T_{\text{max}}(m)$ which gives rise to many applications for particle identification. At non-relativistic energies, the Bethe-Bloch formula is dominated by $1/\beta_{\text{rel}}^2$ up to $\beta_{\text{rel}}\gamma \approx 3.4$. At this point, the function has a local minimum, and particles with the corresponding energy are called minimum ionising particles. If the energy of a particle is further increased, its energy loss grows logarithmically. When the material consists of various elements, a good approximation is to average over all elements in the compound weighted by the fraction of electrons belonging to each element.

When a charged particle experiences a change in velocity, it perturbs the surrounding electromagnetic (EM) field, causing the emission of photons. The Bethe-Bloch formula only considers particle interactions with atomic electrons and nuclei, but radiation becomes relevant above $\beta_{\text{rel}}\gamma$>1000. For each particle, there is a critical energy E_c at which the ionisation losses are equal to the radiation losses. The magnitude of radiation losses depends on the particle's charge and mass. Acceleration due to a magnetic field is called synchrotron radiation [80], while deceleration due to interaction with another charge is called Bremsstrahlung [79]. The energy loss due to Bremsstrahlung per unit distance in a material scales roughly as $dE/dx \propto 1/m^2$, so lighter particles radiate much more than heavy ones [79]. Charged particles also radiate as they pass between materials with different refractive indices during a process referred to as transition radiation.

Electrons and positrons cannot be described by the above-mentioned Bethe-Bloch formula (see Equation 3.1) as they have identical mass as atomic electrons, which changes kinematics. Additionally, the indistinguishability between impacting and target electrons needs to be taken into account. The adjusted Bethe-Bloch formula for electrons can be found in literature [81]. Light charged particles with energies below a few MeV lose most of their energy by ionisation. Above a few tens of MeV in low-Z materials, and above a few MeV in high-Z materials, radiative losses begin to dominate. At high energies, the radiative stopping power is linear with the electron energy $<dE/dx>=E/X_0$, which defines the radiation length X_0 as the average distance over which the energy is reduced by a factor $1/e$, where e is Euler's number.

Neutrons are neutral particles, so they do not interact via the Coulomb interaction. As for other particles, reactions are dependent on the energy of the neutrons. The most significant reaction in the MeV range is elastic scattering at the material's nuclei. This process is used for moderating (slowing down) neutrons. Neutrons can also excite a whole atom or knock out a neutron and hence transform an atom into a different isotope. At energies of hundreds of MeVs, the production of hadron showers becomes possible as discussed later in this section.

Photon-induced interactions in matter are different from those induced by charged particles. Since photons are massless and uncharged, they do not lose energy through continuous electromagnetic interactions along a path, as charged particles do. Instead, they interact discretely. When a burst of photons passes through a layer of material, there is no loss of energy, but the intensity is reduced. The loss of photon intensity I follows $dI=\mu I dx$, μdx is the probability that the photon will interact within the depth x. The coefficient μ is called the photon attenuation coefficient. The number of photons passing through matter decreases $I=I_0 \exp(-\mu x)$. The type of photon interaction strongly depends on the photon energy.

EM showers are the result of bremsstrahlung of electrons or positrons in matter combined with the production of electron-positron pairs by photons. When an incident energetic photon, electron or positron travels in the material, it produces a cascade of new particles until the energy of the photons produced by the radiation is below the threshold for pair production. The cross section for pair production σ_{pair} of photons with high energy scales as $\sigma_{\text{pair}} \propto 1/X_0$, showing that X_0 is a characteristic length for both

bremsstrahlung and pair production [79]. The longitudinal profile of the EM shower can be described by the Heitler model [82], which assumes that bremsstrahlung or pair production always occurs after a distance of X_0. The depth of the shower is proportional to $A/(Z^2\rho)$, where A and Z are the nucleon and proton number and ρ is the density of the material, and depends logarithmically on the initial energy. The transverse profile of the shower is almost independent of the energy of the incident particle and can be described by the Moliere radius $R_M \propto X_0/E_c$, which gives a cylinder with a radius of R_M where 90 % of the energy is deposited by the shower [79].

Hadron showers develop when an incident energetic hadron undergoes an inelastic nuclear collision in a material. In addition to the EM force, which mediates the interaction between the nucleus and the electron shell, the strong force binds constituents of nucleons, quarks and gluons. The residual strong force then binds the nucleons within the nucleus. An important property of the strong force is the confinement of quarks [83]. This is very different from the EM force, where the strength of the force exerted by two electrically charged objects becomes weaker as the charges are further apart. In contrast, when two particles with a colour charge (*e.g.* $q\overline{q}$) are separated by an energy greater than a threshold, two new quarks are created. This leads to the fact that all physically observed particles have no colour charge. If the energy of the bombarding particle is sufficient to interact with nucleons inside the nucleus, the kinetic energy is transferred to the rest mass energy of the newly produced hadrons. This leads to a hadronic shower.

When a high-energy particle (usually a hadron) collides with the nucleus of the target material, it can excite the nucleus, causing it to decay by emitting nucleons or photons. If the energy is above 1 GeV, it might undergo an inelastic nuclear collision, producing new hadrons, mostly nucleons and mesons. The chain reaction continues until the energy of the particles falls below the pion production threshold, which is just above the pion's rest mass ~140 MeV) [84]. The total cross-session of an interaction σ_T has two parts, elastic σ_{el} and inelastic σ_{in}. Only the latter is susceptible to induce a hadronic shower. It can be geometrically approximated as $\sigma_{in.} \propto A^{2/3}$, where A is the nucleon number. A longitudinal evolution of the hadron shower is described by the mean free path λ, inverse of $n\sigma_{in}$ where n is the number of nuclei per unit volume. The λ follows

$$\lambda \propto A^{1/3}/\rho \tag{3.2}$$

where A and ρ is is the proton number and density, respectively. The interpretation of Equation 3.2 is that the short mean free path comes mostly from high density. For dense materials $\lambda > X_0$ [79]. Hadron showers are always accompanied by an EM shower, because some hadrons decay electromagnetically, *e.g.* the neutral pion π^0 decays into two photons, most of the time. Since EM showers are narrower than hadronic ones, the EM component of the shower is mainly concentrated around the shower core. Models that describe hadronic showers have been embedded in particle transport codes such as FLUKA, which will be described in the next section.

The above-described zoo of particle interactions with matter will be useful to understand how the energy deposition is calculated in practice. Physics models are embedded in particle transport codes (*e.g.* FLUKA described in the following section), based on the Monte Carlo technique, which can describe the probabilistic nature of this problem.

3.2. The simulation code FLUKA

The different particle interactions, discussed in the preceding section, make the calculation propagation of particles through a material complex. The particle transport problem can be defined as the calculation of the change in particle number density after a particle has propagated through a bulk of material [85]. The Monte Carlo method, a type of algorithm that relies on repeated random sampling [86], is a highly effective approach for this purpose. The energy and direction of a single particle are initialised. If the particle is in a vacuum, it is transported to the boundary of the next material. Otherwise, the total cross-section for the interaction of the particle with the material is calculated according to the type and energy of the particle. The position of the first interaction and its type are then randomly sampled, taking into account the energy loss, the change in direction, and the number of secondary particles created by this interaction. The procedure is then repeated for all primary and secondary particles until they all exit the region of interest or their energy falls below the user-defined threshold. The aforementioned steps are carried out using particle transport codes that are equipped with a pseudo-random number generator and libraries of measured cross-sections for a wide range of particle interactions with matter.

FLUKA is a general-purpose tool for calculating particle transport in matter [87], [88] and is used in many related fields such as accelerator science, radiotherapy or space science. With high accuracy, FLUKA can simulate the propagation of about 60 different particle types in matter. Complex geometries can be defined in FLUKA. External magnetic or electric fields can be applied to simulated particles. In FLUKA, single events are simulated, initiated by a primary particle or collision event. The output is automatically averaged over all simulated primary events and normalised per primary particle.

The FLUKA geometric modelling is based on various 3D bodies like spheres, boxes, and cylinders, which are combined using Boolean operators (+ union, – difference, and | intersection) to form a region. Regions can be non-continuous but must have a uniform material composition and be enclosed by an infinitely absorbing "blackhole" material. While complex regions can be constructed, simplification is common to reduce simulation time. Regions cannot overlap, as particles must belong to only one material. Besides the available list of pre-defined materials, materials with arbitrary properties can be defined by specifying composition and density.

Before the start of a FLUKA simulation, scoring regions of interest must be defined. A scoring routine is triggered each time a particle satisfies the specific conditions associated with a given scoring card. These routines enable the estimation of radiometric quantities, yielding statistical averages over the simulation histories of primary particles. In addition to the mean value, FLUKA also provides standard deviations and statistical uncertainties.

In this work, the main radiometric quantities of interest are fluence and dose. Fluence in a given point in space refers to the number of particles crossing a unit cross-sectional area per unit time. It can be interpreted as the number of particles passing through a hypothetical small sphere centred at the given point. Fluence is usually weighted with the track length to account for the actual length the particle travels inside the volume. Dose represents the energy deposited per unit mass of material. Two FLUKA scoring cards primarily employed in this study are USRBIN and USRTRACK.

USRBIN applies a spatial mesh, either Cartesian or cylindrical, over the volume of interest. This mesh divides the volume into bins where FLUKA records quantities such as the fluence or the energy deposited (dose). The result is a three-dimensional distribution, which can be projected onto two-dimensional flux maps or reduced to one-dimensional profiles, depending on the analysis needs. USRTRACK, on the other hand, does not rely on a fixed spatial mesh.

Instead, it accumulates the total track length of particles within a defined region and normalises it by its volume. Both USRBIN and USRTRACK allow for the selection of specific particle types or groups, such as electromagnetic particles or neutral hadrons.

3.3. Beam-induced damage

The FLUKA code will be used in the next part of this thesis to calculate the amount of energy deposited by the 440 GeV proton beam in the superconducting coils made of Nb-Ti and Nb_3Sn. In the following, only solid materials will be treated. In case the beam has a high energy and intensity, the material's temperature will rise quickly, which can even cause a change in the material's phase. The induced thermal deformations are accelerated by the softening of the material, but conversely, the mass inertia of the ions initially restricts the expansion [89]. The quantity that reliably describes the beam-induced damage is the density of the deposited energy. Low deposited energy leads to linear and quasi-static mechanical and thermal response of the material, and this can be solved by finite element methods. For higher deposited energy or shorter times, however, dynamic effects start to be important.

In the following, only metals will be treated as that is relevant for the experiment with the LTS coils discussed in the following chapter. Deposited energy below $0.1\,\mathrm{kJ\,cm^{-3}}$ leads to dynamic processes in an elastic regime, so the material slowly returns to its initial state after the end of the heating. In the range between $0.1\,\mathrm{kJ\,cm^{-3}}$ to $10\,\mathrm{kJ\,cm^{-3}}$, the plastic dynamic regime is entered, *i.e.* the dynamic processes leave the material deformed [90]. The beam damage experiment with the sample coils was conducted in this plastic regime. Above about $10\,\mathrm{kJ\,cm^{-3}}$, the stress wave generated will locally change the material density and cause phase transitions to liquid, gas or plasma. In addition, the impact of a bunched beam can lead to a phenomenon called hydrodynamic tunnelling, which further increases the structural damage to the material [91].

The energy deposited by the beam is into heat. If the heating happens so rapidly that there is no time for significant thermal diffusion, the diffusion process can be neglected. The thermal diffusion time in copper, which is the time it takes for a region to reach an even temperature, is approximately $9.5\,\mathrm{ms\,mm^{-1}}$. This supports the use of adiabatic assumption because during

the experiment, the heating took less than 1 µs. Under the assumption of adiabatic heating, the temperature increase can be calculated as

$$\frac{E_{\mathrm{dep}}(x)}{\rho} = \int_{T_0}^{T_\mathrm{F}} C_p(T)dT, \tag{3.3}$$

where the left-hand side is the deposited energy $E_{\mathrm{dep}}(x)$ divided by density ρ. The rise from the initial T_0 to final temperature T_F is given by the integral of specific heat $C_\mathrm{p}(T)$ as a function of temperature T on the right-hand side of the Equation 3.3. The temperature evolution over time is governed by the heat equation, which will not be discussed here.

An unconstrained body deforms when subjected to a change in temperature. In the case of a homogeneous and isotropic temperature change, the thermal deformation is hydrostatic and does not result in a change of shape. The coefficient of linear thermal expansion α, defined by $\alpha L{=}dL/dT$ describes how the size of an object L changes in one dimension with a change in temperature T. At low temperatures, α approaches zero, while at temperatures above or around room temperature, it is almost constant.

The thermal expansion can be described by the material strain. The fundamental principle of Hooke's law, which gives a direct proportionality between small strains, denoted by ε, and the corresponding mechanical stresses, denoted by σ, with a proportionality constant known as Young's modulus, E, was further developed by Duhamel and Neumann to encompass the first-order effects of thermal stress [92].

The calculation of permanent defects resulting from rapid beam heating can be achieved through the use of finite element tools. In this thesis, the finite element method multi-physics engineering simulation software ANSYS® (product version 2020 R2) will be applied [93]. In the FEM simulations, the physics problem, typically described by partial differential equations, is discretised and solved locally for each node. The set of nodes is called the mesh, and by calculating the properties at each node within the mesh, the behaviour of the entire structure can be determined. The time evolution can be asserted by using the solution calculated for the i-th time step as the load for the $(i + 1)$-th step. The Courant–Friedrichs–Lewy condition [94] is typically utilised to ensure numerical convergence, which states that the mesh spacing Δx must be not lower than the velocity magnitude v (speed of sound in the given material) times the time-step, t.

4. Machine protection

This section concludes the theoretical part of the thesis. The protection systems of the LHC are discussed together with their updates for HL-LHC. Despite their robustness and extensive redundancy, the LHC machine protection systems are not immune to failure. In rare cases, a combination of failures or a malfunction occurring faster than the reaction time of the protection systems can lead to unwanted interaction of the beam with accelerator components such as superconducting magnets. An injection failure, identified as a critical failure case for HL-LHC, is discussed in detail.

One of the main challenges of operating a high-energy particle accelerator today is to protect the machine from uncontrolled self-damage. An enormous amount of energy is stored both in the particle beam and in the electrical circuits of the magnets, posing a risk to neighbouring equipment. The energy stored in a single nominal LHC beam is 0.36 GJ and will be further increased to almost 0.7 GJ in the HL-LHC upgrade. In addition, each LHC dipole with a nominal current of 11.6 kA and an inductance of 0.1 H [95] stores $I^2L/2$=6.7 MJ of magnetic energy. In a main dipole circuit, 154 dipole magnets are connected in series, and when the stored energy is summed up, the value is comparable to the energy required to melt a ton of copper at room temperature, demonstrating the criticality of the deposition of even a small fraction of the energy to the machine equipment. In practice, however, it is not the total energy that is critical, but the local density of energy deposition. Only a small energy density on the order of 10 mJ cm^{-3} is sufficient to quench a superconducting magnet [25]. This work aims to find the threshold energy density that will not only quench the superconducting magnet but also cause permanent damage. This is the primary research question that will be addressed in the forthcoming final chapter.

The safe operation of the LHC and its injector chain relies on a Machine Protection System (MPS), which is designed to detect faults, failures, and potentially hazardous conditions, to ensure a rapid response to prevent machine

damage [96]–[98]. The MPS monitors parameters that indicate the occurrence of a fault and initiates an energy recovery procedure. The main objective of the MPS is to protect the machine, protect the beam, and provide evidence. The Quench Protection System (QPS) and Powering Interlock Controllers (PIC) are designed to protect against the risks associated with stored energy in the superconducting circuits. The Beam Interlock System (BIS) links all accelerator systems to the beam dumping system to protect the machine from hazards associated with the beam energy deposition. In addition, all systems in the LHC that can stop operation (initiate beam dump) have a post-mortem record to assess whether the MPS worked as expected [99].

Quench Protection System

If a small region of the superconducting coil transitions to the normal state, a part of the strand becomes resistive. Due to the large current flow in the magnet, the concerned region heats up rapidly (see Section 1.2). This can cause catastrophic damage, resulting in replacement and unwanted downtime of the machine. The QPS is designed to detect and mitigate quenching in superconducting magnets. The voltage is continuously monitored, and if it exceeds ~100 mV for longer than a few ms, the power supply to the circuit is turned off, and an energy extraction system is triggered [100]. The quench heaters, which consist of metal strips attached to the coils, are triggered. The purpose of the heaters is to homogeneously heat up the coil and increase the size of the resistive zone. The circuit of the magnets is additionally equipped with bypass diodes, which allow current to bypass a quenched magnet and limit the voltage across the coil. For the HL-LHC, the QPS in the new HL circuits will be upgraded to speed up quench detection and to make the system more redundant and therefore more robust [101].

Powering Interlock Controllers

The eight arcs of the LHC together with the adjacent straight sections contain cryostats and associated power converters. Each electrical circuit powers magnets distributed over several cryostats, forming a powering subsector, which is managed by a Powering Interlock Controller (PIC) [102]. This design allows independent operation and protection of each subsector, including controlled energy extraction in case of failures. Long arc cryostats, spanning

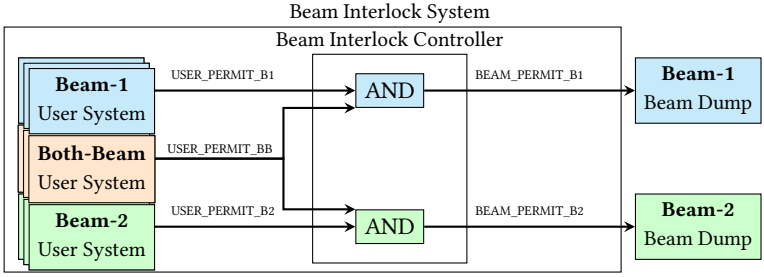

Figure 4.1.: Schema illustrating the working principle of BIS. Signals from user systems for Beam-1 (blue boxes) and Beam-2 (green boxes) and both beams (orange boxes) are evaluated inside a BIC, which sends the beam permit signal to the Beam Dump System.

much of a sector, are powered from both ends and require two PICs, which coordinate signals from hundreds of quench detectors distributed along the magnets.

Beam Interlock System

The BIS is the backbone of the beam-related machine protection, providing interlock control of the accelerators [103]. It receives data from hundreds of systems (User Permit signals) and decides whether the beam can circulate or be injected into an accelerator or a transfer line [104]. If there is a problem in relevant accelerator systems, the BIS will send a request to the LHC Beam Dumping System to abort the beam(s). Examples of interlocks are systems that monitor: the cooling or power supply of magnets, the position of collimators, or the pressure in the beam pipe. The Beam Interlock Controller (BIC), which User Permit signals and generates Beam Permit signals [103]. A simple diagram of the BIS operating principle is shown in Figure 4.1. The response time of the BIS is fixed, but the detection time depends on the system. The time required to respond is the sum of the time taken to detect the fault, transmit the signal through the relevant systems, disable the source, and eject the beam [105].

4.1. Failures

The huge number of components in an accelerator that must work simultaneously poses a risk of failure. A failure can be any event where the required system is not operational. A textbook example of a failure is the 19 September 2008 accident, where an electric arc provoked the release of several 100 MJ of energy, resulting in a pressure wave from the expanded helium that damaged 53 magnets accompanied by a loss of vacuum over more than 2 km [106]. Failures in particle accelerators are classified according to the time they take to develop. This time is usually expressed in units of turns, which is the time for the beam to make a complete loop around the accelerator, for the LHC equal to 89 µs. Failures are then classified as:

1. Single-passage failures: beam lost in LINACs, transfer lines, during injection/extraction
2. Ultra-fast failures, faster than 3 turns (270 µs).
3. Fast failures, faster that 120 turns (10 ms).
4. Slow failures, slower than the Fast failures.

While the beam interlocks work very well for the slow to fast failures, their response time is too slow to protect the machine in the case of single-pass failures or ultra-fast failures [107]. Therefore, protection against ultra-fast failures relies on passive elements such as collimators or other protective elements, like absorbers and masks. Failures can also be quantified in terms of the criticality of a failure and the resulting downtime, and the probability of the given failure occurring, which can be studied by Monte Carlo simulations. Risk quantification is performed in the form of Failure Modes, Effects, and Criticality Analysis (FMECA), Fault Tree Analysis, and Probabilistic Failure Simulation [86].

Injection failure

As mentioned above, the injection or extraction exposes superconducting magnets to a great risk of beam impact [108]–[110]. The scheme of the beam injection system is shown in Figure 4.2. The injected beam must be synchronised with the fast-rising Injection Kicker Magnets (MKIs), and there are four of them per beam. Upstream of the MKIs, which deflect the injected

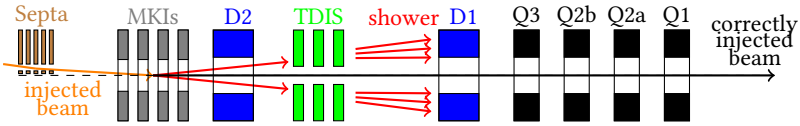

Figure 4.2.: Simplified schematic view of the failure during injection to HL-LHC. The beam passes through five septum magnets (orange boxes) and is further deflected by four kickers (grey boxes). If there is a malfunction, part of the beam hits the TDIS (green boxes), and if the deposited energy is high enough, the particle shower propagates to the downstream mask (red box), dipole (blue box), and quadrupole (black boxes) magnets.

beam vertically, the beam passes through five horizontal septum magnets. The Target Dump Injection Segmented (TDIS) absorber consists of three modules, each of which is individually movable and has a total length of 5.74 m [111]. It is made of graphite, titanium, and copper. The TDIS is installed between the D2 and D1 dipole magnets (separation dipole). The absorber is located 70 m downstream of the MKI, a distance that maximises the angular kick imparted by the MKI and thus the transverse beam displacement at the absorber location. This allows for the efficient interception of beam halo or mis-steered particles. Each module consists of two collimator-like jaws which are designed to absorb misdirected bunches. Consequently, a 1 m-long copper protective mask (TCDD) has also been installed between the MKI and the D2 dipole for the HL-LHC.

Either the injected beam or the stored beam (or both) could be affected by a malfunction of the MKI. Failure modes result in different kick strengths, which in turn result in different impact positions of the beam on the TDIS jaws. If a bunch is injected and no kick is applied, or if circulating bunches are deflected at 100% of the MKI kick strength during a malfunction, the centre of the beam will impact 30 cm to 35 cm from the edge of the TDIS. The resulting energy deposition will be greater if the beam impacts are closer to the edge, or if they graze along the jaws, and particle showers can escape through the TDIS gap. This happens when the kick strength applied to the injected beam is 10% greater or smaller (upper or lower jaw impact) or when the stored beam is deflected by just 10% of MKI strength (lower jaw impact).

During the first years of LHC operation, several injection kicker failures occurred, resulting in magnet quenching. A severity of such failures was

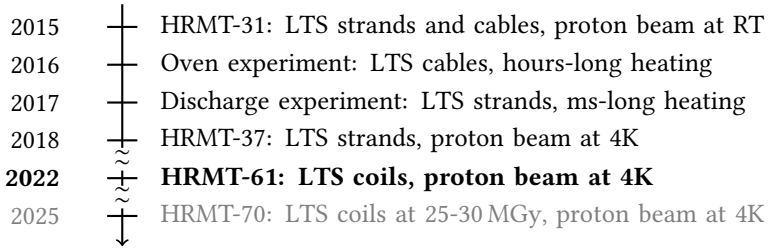

Figure 4.3.: Timeline of the experimental campaign studying damage limits due to beam impact on Nb-Ti and Nb_3Sn Rutherford cables, strands and their insulation. The key elements of the methodology are shown. The experiments performed in the HiRadMat facility at CERN are denoted as HRMTXX. The damage experiment with LTS coils, which will be discussed in the second part of this work, is shown in bold, while the experiment currently in preparation is shown in grey.

evaluated for the HL-LHC [108], [109]. It has been shown that, up to 288 bunches with 2.3×10^{11} protons per bunch could be affected, equivalent to 6.624×10^{13} protons with an energy of 450 GeV hitting the TDIS and producing strong particle showers. This would lead to a peak energy deposited in the superconducting coil of up to $115\,\mathrm{J\,cm^{-3}}$. Assuming the material is pure copper, the energy is equivalent to a temperature rise from 1.9 K to about 100 K and a maximum temperature gradient of up to $41\,\mathrm{K\,mm^{-1}}$ [108].

4.2. Beam-induced damage of magnet components

The strands and their insulation were identified as the parts of superconducting magnets that are most susceptible to damage due to beam-induced energy deposition in the µs regime. Their microstructure can be altered by elevated temperatures, thermomechanical stress or radiation. This can degrade the performance of the strands in terms of their critical superconducting properties (I_c, B_{c2}, T_c) and their overall performance in terms of RRR. It can also reduce the dielectric strength of their insulations and the mechanical properties of the impregnation.

The work presented in this thesis forms part of an extensive experimental campaign, and Figure 4.3 illustrates its timeline. The campaign aims to understand the main damage mechanisms of superconducting magnets impacted by a particle beam. Based on the identified mechanisms, damage limits can be

derived. Incorporating these limits into the machine protection strategies of high-energy hadron accelerators enables them to operate at maximum capacity. This boosts performance by operating close to the damage limits while ruling out damage. The main results of each experiment will be summarised below.

Degradation of LTS strands due to thermomechanical stress

In the 2015 HRMT-31 experiment [1], [2], the Nb-Ti inner layer cables and Nb_3Sn HL-LHC inner triplet quadrupole strands were subjected to a 440 GeV/c proton pulse in an argon atmosphere at room temperature. The tank filled with argon housed the Nb-Ti cable stacks and Nb_3Sn strands. The beam was passing through the tank, and the particle shower heated the cables to peak temperatures of from 1157 K to 1264 K in the Nb-Ti inner layer cables and Nb_3Sn strands, respectively. A degradation of critical current was observed for hotspot temperatures above 900 K for Nb-Ti and 700 K for Nb_3Sn. The primary mechanism of damage in Nb-Ti was attributed to changes in its microstructure, mainly due to diffusion processes that depend on peak temperature and exposure time. Specifically, titanium was observed to diffuse into the copper matrix, which altered the original α-Ti substructure within the filaments [3]. This diffusion also led to a shift in the pinning curve, indicating a modification in the pinning behaviour of the material.

To study the thermomechanical stresses over slightly longer timescales, the Nb-Ti inner dipole and Nb_3Sn HL-LHC inner triplet quadrupole strands were heated up from room temperature in air with the help of a capacitive discharge [2]. The strands were cut to 8 cm long pieces, and discharge of a capacitor bank led to peak temperatures in the strands from 649 K to 1264 K. The maximum temperature was archived ~11 ms after the start of the discharge. The Nb-Ti strands, which reached a peak temperature above 651 K, were found to be degraded during magnetisation measurements. This damage was attributed to variations in the size and spacing of the α-Ti precipitates because pinning behaviour was observed to change as the maximum of the pinning curve was shifted. For samples heated up to a temperature of 1157 K, diffusion of niobium and titanium into the copper matrix was observed. The Nb_3Sn strands started to degrade above 823 K. It was observed that for Nb_3Sn heating with discharge and beam impact induced a comparable critical current density degradation, unlike for the Nb-Ti strands. The comparison indicates

that, unlike at high uniform heating, the degradation after beam impact is not governed by diffusion. Instead, it is dominated by mechanical stresses and crack formation, which are caused by the rapid heating and large thermal gradients localised at the impact position.

Before this work, a beam experiment referred to as strand damage experiment [3]–[5] was conducted in HiRadMat. The Nb-Ti outer layer dipole and Nb_3Sn HL-LHC inner triplet quadrupole strands were cut to a length of 4.8 cm and impacted by the beam. The Nb_3Sn strands were heat-treated with the standard HL-LHC temperature profile (see Section 1.2) in quartz tubes to prevent bending during the heat treatment. The strands were then attached into grooves in a solid copper sample holder using vacuum grease. Three batches of 10 Nb_3Sn samples each and two batches of Nb-Ti were arranged along the beam path. The sample holder was placed in a cryogen-free cryostat and cooled to below 4 K. A proton beam with an energy of 440 GeV systematically impacted each batch with a vertical offset of ~1 mm. Particle showers created by the primary beam induced peak temperatures from 1192 K and 1335 K as well as temperature gradients of up to 346 $K\,mm^{-1}$ and 451 $K\,mm^{-1}$ in the Nb-Ti and Nb_3Sn strands, respectively.

A subset of samples was qualified for critical transport current. No critical current degradation was observed for the Nb-Ti strands up to 1192 K. However, the thermal stability of the Nb-Ti samples was affected by a higher applied current. Thermal stability is the ability to withstand small, localised heat disturbances without irreversibly transitioning to the normal state. It is mainly determined by the temperature margin, the properties of the copper stabiliser and the minimum quench energy. From the sample that experienced a hotspot temperature above 490 K onwards, the critical current was degraded at all fields by 20 to 85 %. Thermo-mechanical FEM simulations were performed to simulate the plastic strain inside the strands. In those simulations, the properties as density and specific heat, reflected the Cu/SC ratio of the HL-LHC inner triplet quadrupole strand. The region of the plastic strain where the degradation started was identified as 0.31 to 0.51 %. Cracks in the filaments of the impacted Nb_3Sn strands were observed using an electron microscope.

This experiment campaign provided important insights into beam-induced damage in different parts of superconducting magnets. However, the applicability of single-strand data to full coil configurations had not been investigated.

Insulation degradation

The strands in the coil are insulated, and damage to the insulation, in terms of dielectric strength, could cause cable-to-ground or inter-turn shorts. These could cause fatal damage to the coil/magnet in case of a quench

The Nb-Ti strands are insulated with polyimide Kapton®, which is a polyimide. This material can decompose when exposed to high temperatures or radiation. The decomposition produces glassy carbon with good conductivity [112]. The dielectric strength of Nb-Ti inner-layer dipole cables was measured during the oven experiment [1], [2]. Six-24 cm-long cables were stacked and secured together in a 10 cm long stainless steel clamp. A pressure of 80 MPa was applied via eight bolts on the stack to simulate the maximum pressure experienced in a LHC dipole during nominal powering. As a cross-check, two stacks were always heated from room to six different final temperatures in the range 461 K to 821 K. The peak temperature was reached in from 3 h to 5 h and cooling back to room temperature took another 13 h to 20 h. The investigation of cables showed that the dielectric strength of the polyimide insulation decreased above 728 K. This was due to a chemical decomposition process that is strongly dependent on temperature and length of exposure. Above 821 K, the insulation was completely lost. The aforementioned beam damage experiment at RT also investigated the degradation of polyimide, and no reduction in dielectric strength was observed except for the weakening of the insulation above a hot spot temperature of 850 K.

Mica S2 glass fibre is used to insulate the Nb_3Sn strands in the HL-LHC inner triplet magnets (see Section 2.3). It provides a continuous conductor spacing, facilitates impregnation and limits crack propagation in resin [113]. The S2-glass increases the stiffness of the epoxy-impregnated strands. However, the heat treatment makes the fibres softer and more conductive, potentially affecting electrical insulation properties [114]. Nevertheless, the dielectric strength remains within the specification.

Epoxy degradation

As outlined in Section 2.1, the HL-LHC magnets will be impregnated with CTD101k, which has been developed and tested for cryogenic applications [115]. The CTD101k is a polymer with a glass transition temperature T_g, which reflects the temperature range over which molecular chain mobility

increases significantly. Accordingly, for CTD101K cured for 5 h at 110 °C and 16 h at 125 °C the glass transition ranges from 115 °C to 146 °C [114].

The irradiation of polymers is well-studied, and the breaking of covalent bonds (scission) or the connection of two polymer chains (cross-linking) has been observed as the irradiation produces free radicals [116]. The alternation in their structure affects their viscoelastic behaviour, leading to a change in their mechanical properties such as storage moduli G', which describe the reversible deformation of a material.

During an irradiation experiment [117], CTD101K was exposed to γ-rays from a ^{60}Co source at an average dose rate of 2 kGy h^{-1} at room temperature in air. In addition, the material was irradiated with 24 GeV protons at the IRRAD facility with a fluence of approximately 1.4×10^{16} p$^+$/cm^2/week, under different conditions: in air at room temperature, in an inert atmosphere at room temperature, and in liquid helium at 4.2 K [117]. The evolution of both T_g and the storage modulus G' was found to be qualitatively similar for the different irradiation conditions and radiation types. An increase of T_g and G' was observed up to doses of about 7.3 MGy, attributed to radiation-induced cross-linking, followed by a decrease at higher doses. At doses relevant for HL-LHC applications (25 MGy to 30 MGy), the reduction of T_g and G' indicates the onset of radiation-induced degradation mechanisms.

Part II.

Experimental study of damage limits in superconducting coils

5. Sample coil preparation and qualification of virgin samples

This part will discuss the estimation of the damage limits for superconducting coils when impacted by high-intensity proton beams. These limits are derived by impacting the LTS coils with a 440 GeV proton beam and subsequently qualifying their critical current in order to ascertain any potential degradation of their superconducting properties. This part is structured into two chapters. Chapter 5 details the preparation of the coil damage experiment and the measurements performed prior to irradiation. Chapter 6 covers the experiment design and measurements performed during and after the beam impact. It concludes with the interpretation of the results and the preparation for an upcoming experiment with radiation-aged Nb_3Sn coils is discussed. The preparation and execution of the beam impact experiment have been reported in [6]–[8], and is integral part of this thesis. To maintain readability, citations are not explicitly marked in these two chapters.

The production steps - assembly, winding, and impregnation - of the sample coils are explained in Section 5.1. The following section, Section 5.2, elaborates on the transport current measurements, which were performed to qualify the samples before the beam impact. The placement of coils during the experiment and the experimental setup in the HiRadMat facility is described in Section 5.3.

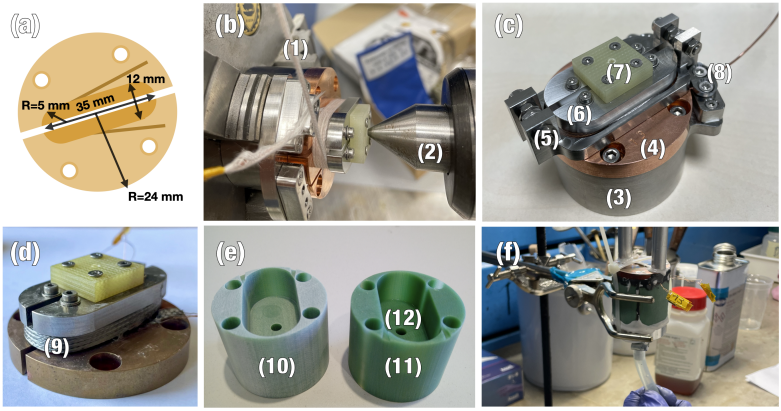

Figure 5.1.: Production steps of a Nb_3Sn sample. (a) Schematic of a core consisting of two semi-circular pieces insulated with Macor® ceramics (same for both types of coils) with dimensions indicated in the schema. (b) Coil winding: (1) unreacted Nb_3Sn strand insulated with AGY S2 fibre glass, (2) needle of the winding machine arm. (c) Wound Nb_3Sn coil: (3) winding structure, (4) semicircular piece, (5) heat-treatment clamp, (6) blocking piece, (7) holding piece, (8) strand holding piece. (d) Reacted Nb_3Sn coil with a view on the reacted Nb_3Sn strand. (e) Protection clamp with the view on the (12) central hole for impregnation: (10) virgin protection clamp, (11) impregnated protection clamp. (f) Impregnation of a sample with CTD101k epoxy, which is injected through the central hole of the protection clamp.

5.1. Sample preparation

The sample coils are based on the two LTS strands (Nb-Ti and Nb_3Sn) introduced in Section 1.2, and their design reflects key aspects of the coils used in the LHC dipoles and HL-LHC inner triplets, in particular the use of materials, epoxy impregnation, and turn geometry (see Sections 2.2, 2.3). The coil layout was proposed in earlier work [3] and has been adapted here.

The coils were assembled and wound in-house[1]. Most of the parts (except the G10 protection clamps) were produced in-house. Figure 5.1 shows a compilation of photos that illustrate the fabrication of a Nb_3Sn coil. In the following, the parts of the sample coil, visible in Figure 5.1, will be discussed.

[1] The technical drawings were created by N. Glamann from Institute for Beam Physics and Technology, and the parts were produced by KIT workshop of the Institut für Biologische Grenzflächen, both part of Karlsruhe Institute of Technology, Karlsruhe, Germany

The non-magnetic winding core consists of two copper pieces and a Macor® ceramic sheet. The winding has a racetrack shape with straight sections of 25 mm and a bending radius of 5 mm. The ceramic sheet is positioned vertically within the core mid-plane to provide electrical insulation between the copper halves. The extension of the copper pieces features a machined groove to accommodate the superconductor strand terminal. This extension has a semicircular shape. The semicircular pieces serve as a power connection during the qualification measurements before and after the beam impact. The coil is then fixed during qualification and during the beam experiment with the four holes, two on each piece. To secure the structure and prevent strand movement, two stainless steel wire-blocking pieces were positioned at the top of the winding core. Additionally, a stainless steel winding structure was attached below the copper body to enhance stability during the winding process. Small stainless steel pieces were utilized to hold the strand and end wire terminals in place during winding. A rectangular G10 holding piece was positioned on top of the assembled body to attach the two sides together and support the needle of the winding machine arm. The complete coil body has a diameter of 48 mm and a height of 23 mm.

Following the assembly, the coil winding was initiated, using two types of LTS strands with a length of 1.7 m. In total, 15 coils were constructed with 0.825 mm Nb-Ti strands insulated with polyimide. Another 15 samples used AGY S2 glass fibre insulated Nb_3Sn MQFX strand with a diameter of 0.85 mm. Details on the strands are given in Section 1.2.

The coils were wound on a LW90 linear winding machine manufactured by RUFF GmbH, Germany. A consistent procedure was followed for both types of coils, with variations in the force settings due to the ductility of the materials. A force of 80 N was applied for Nb-Ti and 50 N for Nb_3Sn. The initial phase involved programming the machine to optimise parameters such as the number of turns and movement coordinates. This was verified using a test coil with copper wire. The winding has 5 turns in the first and third layers and four turns in the second and fourth layers to maintain geometric symmetry. Although using the same winding procedure for all samples, some variation in performance are observed during qualification measurements (see Section 5.2).

The end of the strand of the Nb-Ti coils was soldered to the semicircular pieces, and two sets of voltage taps were installed to allow for efficient critical current measurements. The voltage taps are made from twisted pair of copper

wires with a diameter of 0.2 mm. They were soldered directly to the LTS strands. The total length of the strand used for one coil is 1.5 m. The longer and shorter tap pair, labelled AB and CD, have a length of 1.45 m and 1.4 m, respectively. A LEMO connector was fixed at the end of the taps.

The coil was preheated to 200 °C with a heating plate to facilitate the soldering process. The complete Nb-Ti coil is visible in Figure 5.7. The same was done with a heating oven preheated to 165 °C for the Nb_3Sn based coils following the heat-treatment process that will be described below.

The coils using Nb_3Sn strands underwent a heat treatment[2] to ensure the formation of the superconducting A15 phase, following the standard HL-LHC temperature profile including dwell times at 210 °C for 48 h, at 400 °C for 48 h and at 665 °C for 50 h (see Section 1.2). In order to accommodate the volume expansion of the strands during this process and to prevent bending due to inhomogeneous heating and cooling, stainless steel heat-treatment clamps were used. These were subsequently removed so the voltage taps could be soldered to the semicircular pieces.

The Nb_3Sn strands, which become brittle and fragile after heat treatment, were stabilised by impregnation with CTD101k epoxy resin[3]. To protect the strands during powering, which comes with high electromagnetic forces acting on the strands, a G10 clamp was installed. Additionally, the clamp facilitated an impregnation process where it acted as a mould. The protective clamp has a height of 40 mm and contains five holes, four to fix the coil during the measurements and a central hole to inject the epoxy. The process began with the separate impregnation of the clamp, which was porous and released the epoxy during the first trials. The clamp was glued to the coil to prevent it from moving. The epoxy components were heated, mixed and placed in a gas bubbler to remove air. The mixture was then injected into the preheated coil through the centre hole of the clamp, ensuring that all voids were filled as the remaining air was evacuated. The epoxy was injected with resin and the mould heated to a temperature of 60 °C. The curing of the epoxy was conducted in two isothermal steps: the first at 110 °C for 6 h and the second at 125 °C for 16 h. After impregnation, some voltage taps were found to be

[2] Heat treatment was performed by D. Zurmuehle Group of applied Superconductivity at Department of Quantum matter Physics, University of Geneva, Switzerland

[3] The impregnation was performed by S. Clement and C. Urscheler from Polymer laboratory, CERN, Switzerland

non-conductive and were subsequently soldered to the side of the copper terminals. A complete Nb_3Sn coil with the protection clamp installed will is shown in Figure 5.1 (or see Figure 5.7).

5.2. Qualification of samples

This section describes the transport current measurements[4], introduced in Section 1.3, performed before the beam impact. Based on the measurement data, the quality of each coil was assessed, which determined both its suitability for use and its position in the experiment (see Section 5.3).

Short-sample limit

The following calculation of the short-sample limit is based on the connecting measurements and simulations of others. Dedicated Opera simulations [118] were carried out to determine the magnetic field generated by the current I for both coil types. These simulations provided a scaling constant between the peak magnetic field in the coil winding and the applied current I as $B{=}CI$, usually called the load-line. The coefficient was determined as 2.50 T/kA and 2.44 T/kA for Nb-Ti and Nb_3Sn coils, respectively. These values were adopted with 5 % relative uncertainty.

In the strand damage experiment (see Section 4.2) [3]–[5], 48 mm long strand samples of the identical type were measured for the critical transport current with the same setup as used for the coils. The strand samples were soldered onto copper supports, which provided both mechanical and thermal stabilisation. The distance between voltage taps soldered on the strands was 15 mm and the electric field criterion with E_c of 1.0 μV/cm was used to determine the critical current. They were qualified at various external magnetic fields, and the results of these measurements were used to derive the expected critical current for the sample coils as shown in Figure 5.2.

The scaling laws for Nb-Ti (see Equation 1.6) and Nb_3Sn (see Equation 1.7) were utilised to extrapolate the strand data. The intersection of the load-line

[4] Transport current measurements were performed by M. Bonura, Group of applied Superconductivity, Department of Quantum matter Physics, University of Geneva, Switzerland

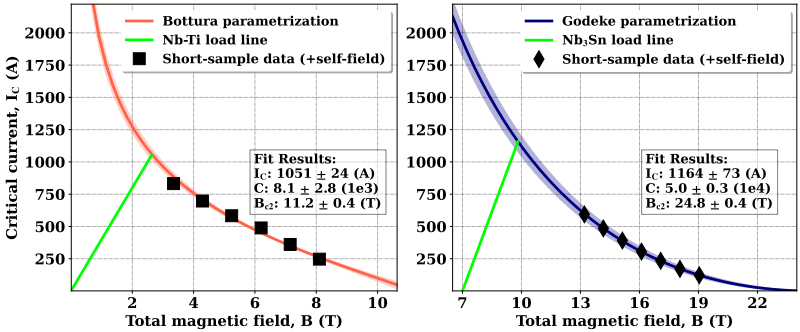

Figure 5.2.: Short-sample measurements of Nb-Ti (left plot, black squares) and Nb_3Sn (right plot, black diamonds) strands for the strand damage experiment ([3]–[5], blue and red squares) fitted with Equation 1.6 and Equation 1.7, respectively. The measurements presented here were analysed using the electric field criterion with critical electric field E_c of 1.0 µV/cm. The cross-section of the load-line simulated with Opera [118] (green line) with the parametrization gave the short-sample limit of 1051±24 A for the Nb-Ti coils at self-field and 1164±73 A for the Nb_3Sn samples at 7 T external magnetic field.

for each coil type and the respective parametrization, yielded Short-Sample Limits (SSL) which is the maximum current that can, in principle, be achieved in a coil based on the single strand performance and simulated load-line for a coil. Evaluating the measured current for a coil against the SSL allows for a meaningful assessment of the coil's performance, either individually or in comparison to other samples, by indicating how closely it approaches its theoretical maximum. The Nb_3Sn coils were measured in an external field to reduce the critical current (see Section 5.2). The load-line was found as 1023±24 A for Nb-Ti at self-field and 1129±70 A for Nb_3Sn at 7 T external magnetic field.

Measurement preparation

After impregnation, excess epoxy and glue were removed, and the underside of each Nb_3Sn coil was carefully polished to maintain a straight surface. This step is critical because any impurities or irregularities on the surface through which the coil is powered increase the contact voltage, which can cause probe vibration or heat loss, resulting in reduced helium levels in the measurement setup. In addition, the underneath surface of the coils was

subjected to prolonged etching in a solution of 50 % acetic acid and 50 % water for more than a day. The etching was performed for all Nb_3Sn coils before and after the beam impact, but for Nb-Ti only after the beam impact as they were characterized earlier in the campaign, before the implementation of the etching procedure.

Transport current measurements of virgin samples

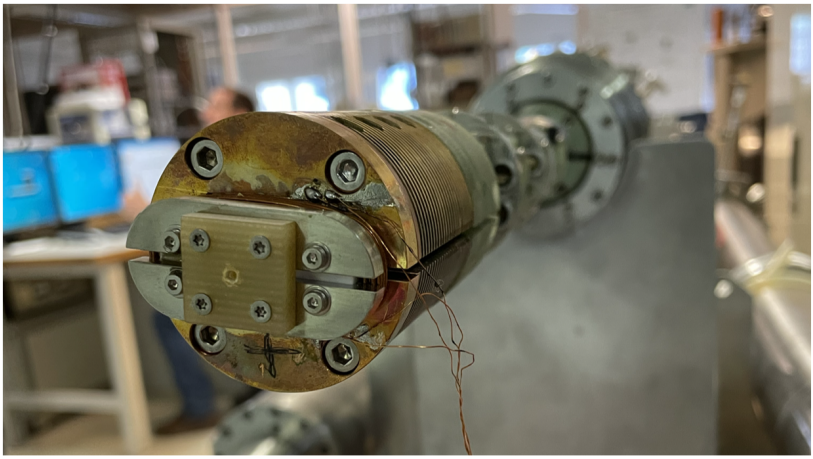

Figure 5.3.: A Nb-Ti sample installed on the high-current probe before the transport current measurement at the University of Geneva.

Figure 5.3 shows a coil installed on the high-current probe. The voltage taps were plugged into an enclosed connector. The probe, together with the sample, was then inserted into a cryostat filled with liquid helium and equipped with a magnet that can provide an external magnetic field. The coils were installed so that the magnetic field they produce was parallel to the magnetic field generated by the magnet inside the cryostat. This prevents the risk of magnetic torque being created, which could result if the vectors of magnetic fields are not directly parallel. Additionally, in this way the applied magnetic field adds up to the produced self-field. thus reducing the critical current (see Section 1.4). This simplifies and shortens the measurement.

After the temperature of the samples reached a stable temperature around 4 K, multiple current sweeps were performed. During each sweep, the current was increased at a rate of 1 A/s, then it was reduced to 0.25 A/s, at 650 A for Nb-Ti and around 950 A for the Nb_3Sn samples. For the pre-irradiation measurements, this procedure was followed as described. After the beam impact, the nominal current was already known, and a higher ramp rate was used up to 90 % of the pre-irradiation nominal current. The higher speed at the beginning of the measurement was used to reduce measurement time. At the higher current ramp rate, the voltage and its noise are higher due to the increased inductive voltage. However, the ohmic resistance component remains the same for each ramp rate. The current sweep was continued until the voltage across the coil exceeded 0.1 μV and 0.15 μV for Nb-Ti and Nb_3Sn samples, respectively.

The different approaches to defining the critical current from transport current measurements were discussed in Section 1.3. During the analysis of the critical current measurements, the electric field criterion was used with the critical electric field set to E_c=1.0 mV/cm. During the transition, only a small part of the wire becomes normal conducting, creating a resistive voltage. The best approach would be to simulate how large the normal conducting zone is and divide the voltage by this value to get the electric field. In the strand experiment [3]–[5], the voltage measured by the voltage taps was divided by the distance of 15 mm between the taps, assuming that the whole area between the taps is quenched. As the results from the strand experiment and here-presented coil experiment should be directly comparable, it was decided to divide all measured voltages by the same value, thus assuming that the quenched region of the strand and coil is similar.

Results for Nb-Ti coils

In total 5 Nb-Ti coils were qualified before and after the beam impact in their self-generated magnetic field. For the purpose of the experiment, they were grouped in batches and ordered. All 5 Nb-Ti coils were used in batch 1, therefore they have the labels B1Ti1-5.

Figure 5.4 shows two examples of critical transport current measurements. The data shown were recorded for the Nb-Ti coil sample B1Ti3. The left plot of Figure 5.4 shows the second current sweep of the coil, where no transition was observed, and the measurement was stopped because of a thermal runaway, which caused a trip of the power supply. A thermal runaway is the uncontrolled rise in temperature due to a feedback loop between local heating and resistivity, where loss of superconductivity initiates Joule heating, which causes further loss of superconductivity. Therefore, the maximum current at the moment the thermal runaway was recorded as I_Q=987 A and denoted as a quench current I_Q. After the current I_Q was reached, the voltage across the coil leapt over the threshold voltage, and the measurement was stopped.

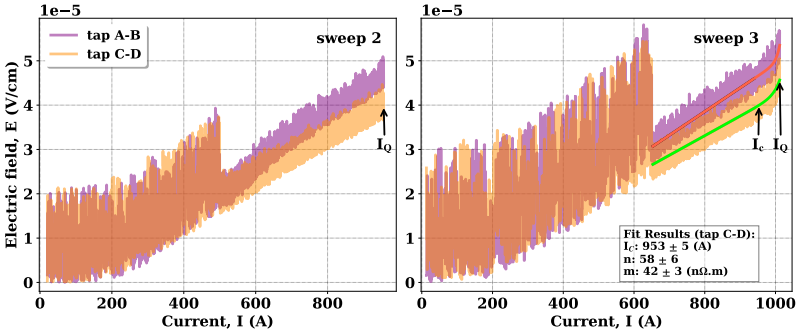

Figure 5.4.: The electric field in the Nb-Ti coil B1Ti3 is plotted as a function of the applied current during the transport current measurements. The left and right plots show the second and third current sweeps, respectively. During the second current sweep, no transition was observed. Therefore, I_Q is denoted, while during the third sweep, the transition from superconducting to normal state is clearly visible. For the third sweep, the signal from both voltage taps was fitted with Equation 1.4 (green and black solid lines), and the fit results of I_c, parameter-n, and m are shown.

The right plot of Figure 5.4 shows the third current sweep with I_Q=1026 A, where the transition is clearly visible, and I_c=953±5 A, n and m parameters were derived from fitting the free parameters of the Equation 1.4 to the data, where the uncertainty denotes the standard error from the fit. During the analysis of I_c, the data from both voltage tap pairs were averaged.

The training of the Nb-Ti coils before beam impact is shown in Figure 5.5. For the current sweeps, which led to a transition, the critical current I_c is shown. During the first current sweep right after the winding, the coils reached more

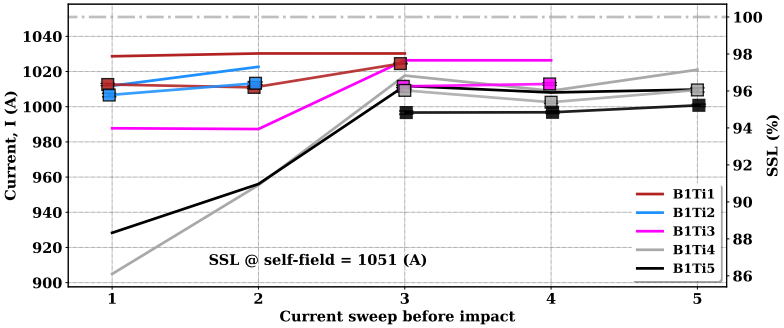

Figure 5.5.: Training of Nb-Ti coils B1Ti1-5 before the beam impact. The quench current I_Q for each coil is shown (solid lines). For the current sweeps, which led to a quench, the critical current I_c found from the fit with Equation 1.4 are shown in terms of current I and as a fraction of SSL (right y axis)

than 900 A. Before the beam impact, the Nb-Ti coils required 1-3 current sweeps to reach more than SI95 of SSL. After training, all Nb-Ti coils reached critical currents between 997 and 1024 A (95 % to 97 % of SSL). This shows the high quality and reproducibility of the winding procedure.

Results for Nb_3Sn coils

From a total of 15 samples which were produced, the first 7 Nb_3Sn coils, which performed well, were used in the experiment. Two of these samples were installed in batch 2 and five of them in batch 3. Therefore, they are labelled as B2Sn1-2 and B3Sn1-5, respectively.

During the first current sweep, the coils reached 593 A to 678 A except sample B2Sn1, reaching 888 A. Before the beam impact, the Nb_3Sn coils required 2 to 13 current sweeps to reach critical currents from 1029 A to 1155 A (88 % to 99 % of SSL) as shown in Figure 5.6. This is significantly longer training than for Nb-Ti coils. The reason is most probably a combination of two things. First, the lower winding tension applied to the Nb_3Sn samples resulted in a reduced effective elastic modulus of the winding pack, making it more susceptible to microscopic conductor and cable motions under Lorentz forces and thus to mechanically induced quenches. Second, the Nb_3Sn coils were epoxy-impregnated. The impregnation is expected to suppress large-scale

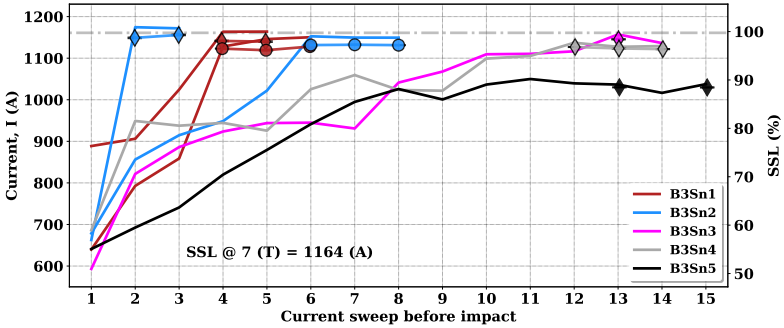

Figure 5.6.: Training of Nb_3Sn coils B2Sn1-2 (circles) and B3Sn1-5 (diamonds) before the beam impact. The quench current I_Q for each coil is shown (solid lines). For the current sweeps, which led to a quench, the critical current I_c found from the fit with Equation 1.4 is shown in terms of current I and as a fraction of SSL (right y axis).

turn motion, but it also freezes in local stress concentrations and small construction imperfections in the brittle Nb_3Sn conductor. These locked-in weak spots can progressively release stress or degrade during successive quenching, giving rise to additional training quenches. In contrast, the more mechanically tolerant Nb-Ti coils, wound with higher tension and without impregnation, can settle and redistribute stresses more readily during the first few ramps, which explains their much shorter training.

Firstly, the use of a lower tension for Nb_3Sn samples likely led to a lower elastic modulus of the entire winding, which made the winding more prone to microscopic movements, causing mechanically induced quenches. Secondly, the Nb_3Sn coils had to be impregnated, and therefore, there were additional training quenches caused by the cracking of the epoxy. Likely the impregnation reduced macroscopic turn motion but locked in microscopic mechanical imperfections in a brittle conductor, leading to many training quenches, whereas the more mechanically tolerant Nb-Ti coil can settle quickly and exhibited only limited training.

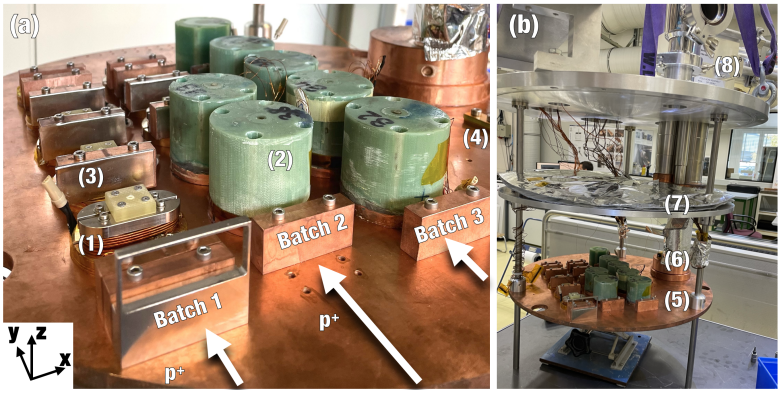

Figure 5.7.: *Left:* Experimental setup: (1) complete Nb-Ti coil and (2) complete Nb_3Sn coil protected by protection clamp, (3) shower block covered with witness foil, (4) temperature sensor. The direction of the incident beam for all three batches is indicated by white arrows and the metrology reference coordinate system is shown in the lower left corner. *Right:* Installations inside the vacuum vessel of the vacuum vessel: coil samples installed on (5) the second cooling stage, (6) cryo-cooler head, (7) the first cooling stage, (8) the outer part of the cryocooler head (compare to Figure 5.9).

5.3. Experimental setup for damage experiment

The severity of the damage caused by the high-intensity beam depends on the number of secondary particles in the shower, which can be amplified by increasing intensity and lowering the transverse size of the primary beam, or placing material upstream of the sample. Preliminary energy deposition simulations were conducted to match the energy deposition in the samples to the desired range, and the experimental setup was designed and built based on these simulations. This section describes the coil sample arrangements inside a dry-cooled cryostat. The metrology and survey measurements are detailed, which ensured the samples are correctly aligned with the incoming beam. Finally, the instrumentation inside and outside the vessel will be discussed.

In total, 15 coils were selected for the experiment and grouped in three batches as shown in Figure 5.7. All coils were mounted on a copper plate, serving as the sample holder and conducting cooled plate. Batch one included 5 Nb-Ti coils. Blocks of copper with a thickness of 1 cm were used to enhance the particle shower development, leading to a higher energy deposition in the

coil windings. Selected shower blocks were wrapped in 0.1 mm thick tin witness foil to enable visualisation of the beam trajectory (see Section 6.3) and benchmark the energy deposition simulations (see Section 6.5). The seven blocks and six foils in batch one were assigned labels B1B1-7 and B1F1-6, respectively. The position of each coil within a batch was determined by the number of quenches it had undergone and its critical current (see Section 5.2). Those that had undergone fewer quenches during training and reached higher critical currents were placed upstream.

Batch two consisted of two Nb_3Sn coils followed by three Nb-Ti coils and one shower block in front of the batch. There were four blocks fixed on the Nb-Ti samples. Finally, batch three consisted solely of Nb_3Sn samples, featuring one shower block in front the batch and one upstream the last sample.

To mimic a real accelerator failure, where a superconducting magnet is impacted by a high-intensity beam during an ultra-fast failure, the coils were irradiated at cryogenic temperatures. A dry-cooled cryogenic vessel featuring a Sumitomo RP-82B2 cryocooler head was used as visible in Figure 5.7. The first and the second cooling stage plates were cooled below 32 K and 5.5 K, respectively. The second stage plate, with a diameter of 45.5 cm, was adjusted to enable fixing the coil samples. This plate was enclosed inside a radiation shield connected to the first stage. Both cooling stages and the radiation shield were wrapped in multilayer insulation to suppress radiation losses. The vessel measures 82 cm in height and 52.5 cm in diameter and weighs 125 kg with samples inside.

Prior to the experiment, metrology measurements were performed to accurately map the position of each coil in the vessel with respect to fiducial spheres on the top of the vessel. Based on these measurements, the reference coordinate system was established and used throughout the experiment and post-irradiation investigations. The horizontal and longitudinal position of each sample was determined by scanning its circular perimeter. The left side of Figure 5.8 shows the offset of each coil with respect to the mean horizontal position of its batch. The horizontal distance between batch one and two was measured as 62.7 mm and 62.9 mm between batches 2 and 3. The horizontal centres of the coils in one batch differ by a maximum of 0.4 mm, which is plausible as the horizontal width of winding is more than 25 mm. The position of the coils in the longitudinal direction (along the beam path) was used in the model for the energy deposition simulations.

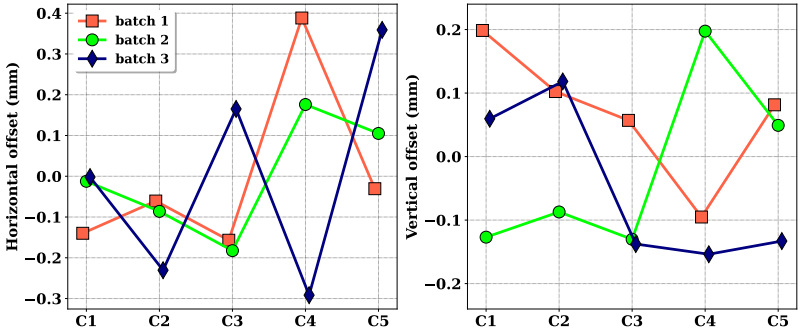

Figure 5.8.: *Left:* Horizontal offsets from the mean vertical position in the metrology coordinate system for each batch: batch 1 (red squares) at -0.2 mm, batch 2 (green circles) at 62.5 mm, and batch 3 (blue diamonds) at 125.4 mm. *Right:* Vertical offsets of the winding centre relative to the mean vertical position of -0.2 mm, calculated as the mean across all samples.

In the vertical plane, the top of a semicircular piece and the top of a protective clamp were measured for Nb-Ti and Nb_3Sn coils, respectively. For the Nb_3Sn samples, the vertical position of the winding for each coil was obtained by subtracting the height of the clamp. The vertical position of the winding of all coil samples is presented on the right side of Figure 5.8). The mean vertical centre of the winding of all 15 samples was measured as -0.2 mm, and the vertical offset of each sample is reported with respect to this mean value. The vertical position of the winding centres of all samples lies within a range of 0.4 mm. Based on these measurements, the centre of the coil winding was derived for both planes and subsequently used for the experiment. During the metrology measurements, a bending of the second stage plate was found, which is most likely caused by the stresses generated from the different thermal expansion of the copper plate and stainless steel rods holding it during the thermal cycle of the vessel. A bending of 0.3 mm was measured at room temperature. This value may be different at 4 K.

The vessel was installed in the HiRadMat TT60 tunnel as visible on Figure 5.9. The schema of the facility was shown in Figure 2.2 in Section 2.1. The cryo-head was connected to a Sumitomo F-70L helium compressor via high-pressure helium gas flex lines. During the beam-impact experiment, the compressor was located in a side tunnel, TJ7, to protect its electronics from radiation. The setup was mounted on a horizontally and vertically movable stage. This allowed for a precise alignment of each batch of samples with the

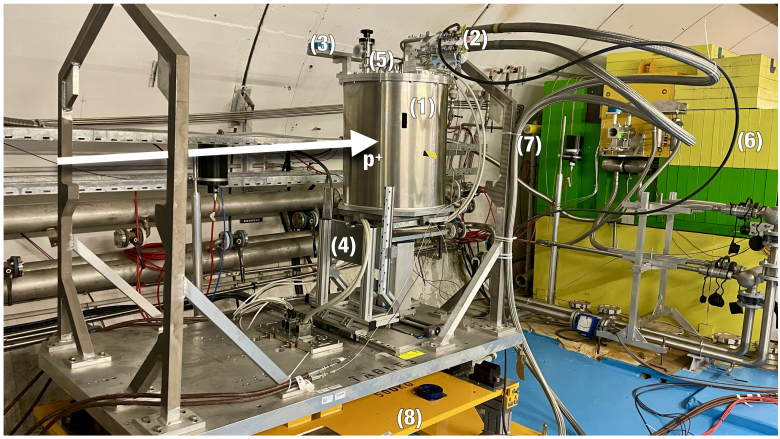

Figure 5.9.: Experimental setup in the HiRadMat tunnel: (1) dry cooled vessel, (2) helium flex lines connected to the cryocooler head, (3) fiducial point, (4) horizontal and vertical movable stages, (6) beam dump and (7) beam loss monitor. Diamond detectors on the top of the vessel (5) and on its side are not visible. The direction of the incoming beam for all three batches is indicated by the white arrow.

beam for impact and also provided the possibility to move the vessel of the beam during beam setup.

Temperature monitoring during the experiment was achieved using two PT100 and two Cernox sensors, which were mounted on the first and second stage plates, respectively. For beam-based alignment purposes, as described in the following Section 6.1, polycrystalline diamond (pCVD) detectors were mounted on the outside of the vacuum vessel. Their outputs were connected to an oscilloscope, located in the neighbouring TT61 tunnel, with a coaxial shunt resistor to protect the inputs of the oscilloscope against high voltages. These detectors were complemented by an LHC-type Beam Loss Monitor (BLM) positioned downstream of the vessel. The combination of data from these instruments was used to align the samples with the incoming beam.

Once the vessel was installed on the experimental table, survey measurements were carried out to establish the relationship between the metrology reference coordinate system, the position of the moving stages and the trajectory of the beam in the tunnel. The inclination of the movable stages was measured during the survey, which causes the laboratory coordinate system and the

coordinate system of the moving stages to be rotated against each other. As a consequence of this inclination, a purely horizontal displacement of the stages results in a change of the vertical position of the vessel. Most importantly, the vertical position of the vessel was different during pure horizontal movements. When impact position for batches 2 and 3 was selected on horizontal stage, the vessel was 0.27 mm and 0.69 mm higher compared to when batch 1 position was selected, respectively.

6. Response of superconducting coils to beam impact

This chapter begins with Section 6.1, which describes the procedure of the beam impact experiment. Section 6.2 outlines the inspection of the samples after the impact, and the information from these inspections is used in Section 6.3 to estimate the trajectory of the beam during the experiment. Section 6.4 discusses the degradation of the samples based on post-irradiation transport current measurements. The superconducting properties after beam impact are correlated with the deposited energy, temperature, and strain experienced by each sample, which were derived using MC and FEM simulations discussed in Sections 6.5 and 6.6, respectively.

6.1. Experimental procedures

In the first phase of the experiment, the correct positioning of the samples in relation to the incoming beam was confirmed during a Beam-Based Alignment (BBA) procedure. The beam instrumentation devices in the HiRadMat facility were introduced in Section 2.1. A low intensity beam ($\sim 5 \times 10^{10} p^+$) was used to scan an object inside the vessel, and the shower levels were recorded by diamond detectors and beam-loss monitors. The signal was normalised by the intensity of each bunch measured with the current transformer in the transfer line. The original plan was to scan the stainless steel frame in front of batch 1 (see Figure 5.7), but the secondary showers produced were not sufficient to give a proportional signal. Consequently, the batch 1 shower blocks and the second stage plate were scanned during the horizontal and vertical BBA, respectively. In the vertical direction, the correct alignment was confirmed. A horizontal offset around 2 mm was measured, which is acceptable if compared to the winding size.

Table 6.1.: Measured beam parameters (Intensity, Number of Bunches, Pulse Length, and Transverse Beam Sizes) of each batch of coils.

Batch	Intensity ($\times 10^{12}$ p$^+$)	Bunches	Pulse length (ns)	σ_x (mm)	σ_y (mm)
1	3.78 ± 4%	36	900	1.33 ± 5%	1.05 ± 5%
2	2.58 ± 4%	24	600	1.33 ± 5%	1.05 ± 5%
3	2.58 ± 4%	24	600	1.33 ± 5%	1.05 ± 5%

In the second phase of the experiment, thermomechanical stress was induced in the samples by high-intensity beam pulses consisting of 36 (batch 1) and 24 (batch 2 and 3) bunches separated by 25 ns. The parameters of each pulse impacting the three batches of coils are reported in Table 6.1.

The intensity of each successive bunch in the pulse was measured with the current transformer in the transfer line (see Figure 6.1). The mean intensity of each bunch was found as 1.06×10^{11}p$^+$. The total intensity of the extracted pulse was additionally measured with another current transformer in the SPS during the scanning the bean with wire in order to get its profile. Both measurements gave consistent results with deviations of less than 4 %. Therefore, the average of both measurements was used with an uncertainty of 4 %.

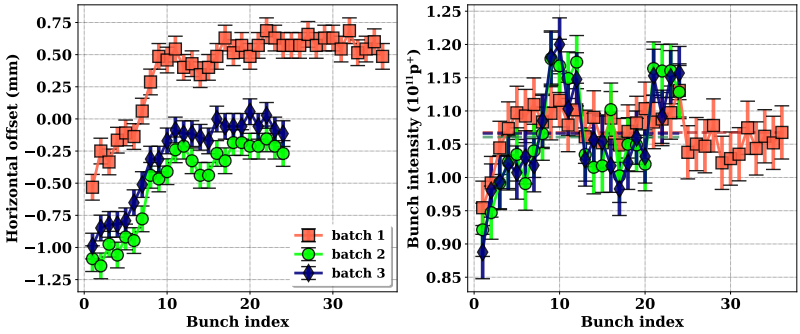

Figure 6.1.: *Left:* Horizontal offset of each bunch within the high-intensity train measured by BPKG upstream of the experimental tables for batch 1 (red squares), batch 2 (green circles), and batch 3 (blue diamonds). *Right:* Bunch-by-bunch intensity of the high-intensity pulse measured with BCT in the transfer line.

The transverse beam size was determined using two independent diagnostic systems. Beam emittance was measured with the wire scanner in the SPS before the first and before the second high-intensity shot. Based on the beamline parameters [119], the horizontal beam size σ_x and the vertical beam size σ_y were determined using Equation 2.2. In addition, the beam size was measured directly at the HiRadMat facility using a beam screen located upstream of the experimental table. The vertical beam size showed good agreement between the two instruments: 1.1 mm from both the wire scanner and the beam screen. The uncertainty of 5 % was calculated by assumption on the uncertainty of the beta function β.

In contrast, a notable discrepancy was observed in the horizontal plane, where the wire scanner reported a beam size of 1.1 mm, while the beam screen measured 1.4 mm, corresponding to a difference of 27 %. This difference is attributed to a bunch-by-bunch transverse position offset within the beam pulse. Beam position monitor data acquired along the bunch train (see Figure 6.1) revealed a systematic horizontal displacement of approximately 1.0 mm between the leading and trailing bunches. As a result, individual bunches, although having similar intrinsic sizes, are centred at different transverse positions. To quantify the impact of this effect, the transverse beam profile was reconstructed by summing the spatial distributions of individual bunches. Each bunch was modelled as a Gaussian distribution with a width determined from the wire scanner measurements. The bunch intensities were normalised using beam current transformer data, while their transverse positions were aligned according to beam position monitor measurements. This reconstruction shows that the bunch-to-bunch displacement leads to an effective broadening of the overall beam envelope. Taking this effect into account, the effective horizontal beam size was determined to be 1.33 mm, with an uncertainty of 5 %.

The observed broadening is likely caused by small transverse orbit variations introduced during the extraction from the SPS and subsequent transfer to the HiRadMat beamline. The reconstructed beam size is consistent with the beam imprint observed on the witness foil (see Figure 6.5). In energy deposition simulations, the full pulse is treated as a single, instantaneous impact, making accurate knowledge of the beam size critical, as it directly influences the calculated density of deposited energy in the sample coils.

Following each high-intensity shot, the temperature of the first and second cryocooler stage rose up to 37 K and 32 K, respectively, as shown in Fig-

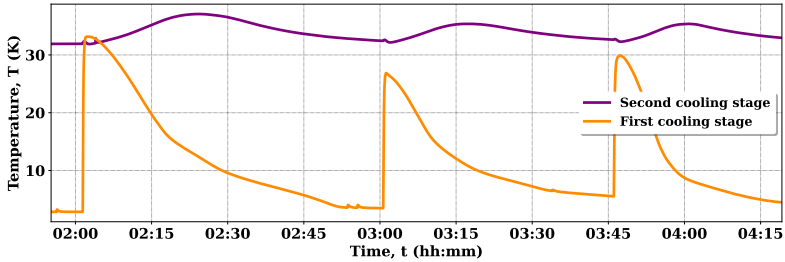

Figure 6.2.: Measured temperature on the first (orange) and the second (purple) cooling stages during the beam experiment. The temperature increase after each high-intensity shot is well visible. The plot originally published in [6].

ure 6.2. A cooling period of approximately 45 min was necessary to restore the temperature of the second stage below 5.5 K between the high-intensity shots.

6.2. Structural and microstructural analysis

This section evaluates the information obtained through visual inspection, computer tomography (CT) and metallography, which were performed after the beam impact. The high energy of incoming protons induced hadronic showers and, thus, create radioactive elements inside the samples. Once the activation levels had sufficiently decayed, the samples were removed from the vessel and examined. The Nb_3Sn sample B3Sn5, which experienced the highest energy deposition, as will be shown in the next subsection, was first qualified with transport current measurements (see Section 6.4) and subsequently inspected by CT. Finally, it was cut open and metallographically examined to study possible defects in the strands or epoxy caused by the beam. Shower blocks and witness foils were also examined for beam imprints. These were used to estimate the trajectory of the high-intensity shots.

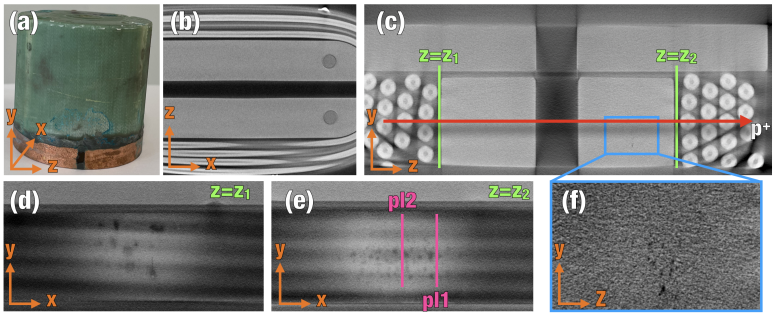

Figure 6.3.: (a) Photo of a complete Nb_3Sn sample with the coordinate system indicated in the lower left corner. (b) View of the winding layers in the z-x plane. (c) Cross-section of the winding showing the turn structure turns arranged in four layers. In this view, the beam enters from the left and exits from the right, as indicated by the red arrow. The layer between the winding core and the first layer of winding, where only CTD101k epoxy is present for each side of the coil, is indicated by two horizontal lines $z{=}z_1$ for the upstream side and $z{=}z_2$ for the downstream side. (d) Zoom on the upstream epoxy layer at $z{=}z_1$ where black spots are visible. (e) Zoom on the downstream epoxy layer at $z{=}z_2$ where more black spots are visible compared to $z{=}z_1$. (f) Zoom on the centre of the copper core where small black spots are visible.

Visual inspection of coils

After the experiment, the coils were carefully examined by a naked eye and with help of an optical microscope. No signs of damage were found on either the strands or their insulation (Nb-Ti samples) or the G10 clamps (Nb_3Sn coils) during these inspections.

Computer tomography and metallographic examination of B5Sn3

Sample B3Sn5, which showed no degradation during the transport current measurements, was examined by CT, and two types of artefacts were observed. Figure 6.3 shows various projections in the coordinate system employed earlier during the metrology measurements. Firstly, epoxy defects were observed in the layer between the winding core and the first winding layer, as shown in plots (d) and (e) of Figure 6.3. The number of defects has increased, but showing smaller dimensions on the downstream side of the coil. Expert opinion suggests that these defects are the copper that has penetrated from the core to

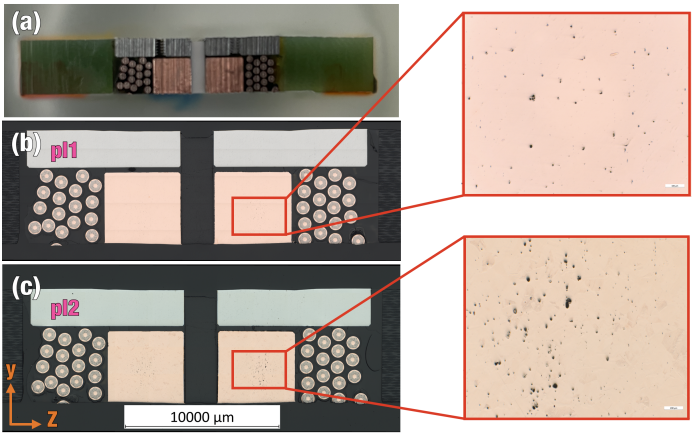

Figure 6.4.: (a) Photo of a Nb_3Sn sample B3Sn5 cut open through the winding to perform the metallographic examination. (b) and (c) Microscopic image of the *pl*1 and *pl*2 with the zoom on the black spots in the core, respectively.

the epoxy [120]. This hypothesis could be confirmed with spectroscopy, as it can potentially affect the dielectric strength of the epoxy. Secondly, there are also defects visible inside the winding core as shown in plot (f) of Figure 6.3. Again, spots are more visible on the downstream side, and their distribution is also wider in the vertical plane, so their appearance could be attributed to the passage of a shower of particles.

Based on the CT scans, the winding of the coil was separated from the rest of the coil, as visible on Figure 6.4. The locations of dark black spots in epoxy, were used to define two cutting planes *pl*1 and *pl*2 perpendicular to the beam propagation (see Figure 6.3). In these planes, the metallographic examinations were performed.

To preserve the coil's integrity during cutting, the winding was embedded in epoxy, as shown in Figure 6.4. The copper defects identified during the CT scans are visible in both planes. There are more of them, and they are larger in dimension in *pl*2. The higher density of spots in *pl*2 indicates that the centre of the beam in the horizontal direction was closer to *pl*2 than to *pl*1. The defects are likely the result of traces of gas (mainly oxygen) in the copper which were released during the beam impact and clustered to create the black spots.

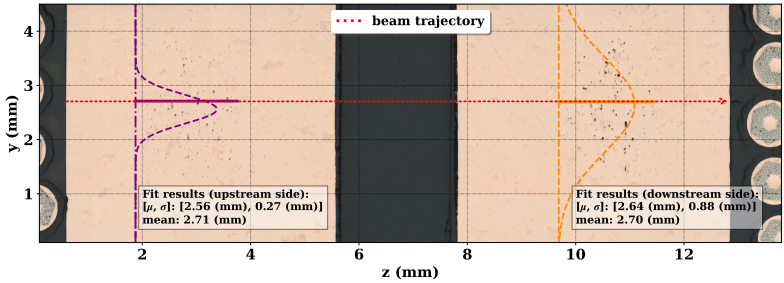

Figure 6.5.: Spatial distribution of copper defect spots found in the winding core. The distribution of black spots was fitted in y-plane with Gauss (dashed line), which gives the mean μ and the width σ, and by taking the arithmetic mean (solid lines). The estimated vertical centre (trajectory of the beam), averaged over the means of both sides, is indicated by a red arrow.

The density of the spots on the upstream and downstream sides of coil in both planes was analysed as shown in Figure 6.5. Based on the colour, the position and size of black spots was identified. The centroid was found in vertical direction in both planes. After converting pixel coordinates into physical dimensions, the vertical position of the beam in sample B3Sn5 was estimated. The mean value of spots in the upstream and downstream side of B3Sn5 was consistently calculated as 2.7 mm of the height of winding core with an uncertainty of 0.1 mm.

Knowledge of the beam's vertical position enabled a deeper analysis of cracks observed in the epoxy. A detailed view of the downstream side of the winding in plane *pl2* is shown in Figure 6.6. The darker cylindrical regions surrounding each strand correspond to epoxy-impregnated glass fibre insulation. Shrinkage voids were observed around some insulation layers, attributed to cooling below 4 K. Metal-to-metal cracks, likely caused by multiple thermal cycles, are visible in Figure 6.6. Two cracks were found at the vertical position corresponding to the estimated beam trajectory. The first crack extends from the winding core to the insulation layer, while the second is located at the epoxy–protection clamp interface. The mismatch in thermal expansion coefficients is the most likely cause of crack formation at these interfaces. No defects were observed inside the protection clamp. Although these cracks are likely associated with beam passage, they did not affect the maximum current reached by the coil, as discussed in the following chapter.

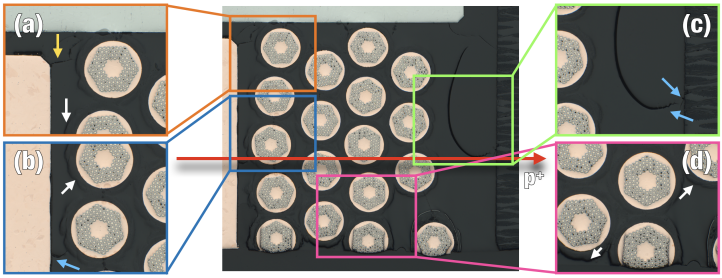

Figure 6.6.: Downstream side of B3Sn5, where the beam path is indicated by the red arrow with a view on various cracks in the epoxy. (a) Zoom on the metal-to-metal crack (yellow arrow) between the blocking piece to the winding core. White arrows show the shrinkage cavities around the strand insulation. (b) Zoom on the crack between the core and a Nb_3Sn strand (blue arrow), most likely caused by the beam. (c) Zoom on the crack found in the epoxy/protection clamp interface (blue arrows) coinciding with the estimated beam passage. (d) Zoom in on the shrinkage voids in the lower part of the winding, which are larger than those in other locations.

The investigation of beam-impacted Nb_3Sn coil follows the same metallographic analyses as was done for coils of HL-LHC inner triples [73], discussed in Section 2.3. Some features as cracks in insulation and porosities, were also observed, especially at the vicinity of spacers. However, microcracks within the filaments, reported for coils of HL-LHC inner triples, were not observed here, consistent with the unchanged critical current of the sample coil.

Visual inspection of shower blocks and witness foils

When examined under the microscope, the shower blocks showed no evidence of beam passage, except for two black imprints found on blocks, B1B6 and B1B7. Both blocks were in batch 1 during the beam experiment. B1B6 was attached to B1Ti4 and B1B7 to B1Ti5 (see Figure 5.7). For the analysis, each block was placed on micrometre paper and studied with a microscope. The pixel-to-millimetre ratio gave a size and location of the imprint, with an estimated error of 0.2 mm.

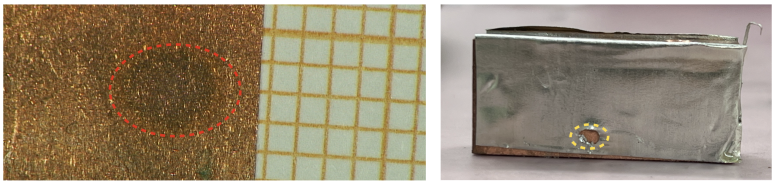

Figure 6.7.: Photos taken during the post-irradiation visual inspection. *Left:* A dark beam imprint (location indicated by red ellipse) on the shower block B1B6 placed on the fourth Nb-Ti coil B1Ti4. *Right:* Melted imprint on witness foil B1F4 (location indicated by yellow ellipse).

The imprint on B1B6 has a horizontal size of 3.1±0.2 mm and vertical size of 2.6±0.2 mm as shown in Figure 6.7. The size of the imprint on B1B7 was difficult to measure as there was no clear boundary of the imprint. However, visually, it seems similar to the B1B6 imprint. As the exact position of the shower blocks and the witness foils was not recorded during the metrology measurements, the position of the blocks had to be estimated from the position of the coils to which the blocks were attached. The uncertainty of the position of the imprint on the shower block was estimated to be 0.3 mm in horizontal direction and 0.1 mm in vertical direction.

Upon opening the vessel, most of the witness foils, which were glued to the upstream side of the blocks with the vacuum grease, had been displaced by the shock wave caused by the beam impact. Only the foils placed between a shower block and a coil windings did not move during the experiment. The melted imprint on B1F4 has a size of 3.6±0.2 mm and 2.8±0.2 mm (see Figure 6.7). The dimensions of the foils varied as they were cut by hand. When the cryostat was opened, the foils and blocks were separated. Fortunately, to accommodate the larger foils, the excess foil was bent. The position of the foils in relation to the blocks was estimated by assuming that the position of the fold was equal to the edge of the block. The uncertainty associated with the position of the imprint on the witness foil was estimated to be 1 mm in both horizontal and vertical directions.

For subsequent calculations of the beam trajectory, the absolute size of the beam imprint is not relevant, only its position is required. Assuming that the target (experimental setup) is isotropic, the imprint shape is expected to reflect the transverse beam profile. In particular, the ratio of the horizontal to vertical imprint dimensions can be used to estimate the transverse beam size. Based on the BTV and WS measurement, the transverse beam size ratio was

determined to be σ_x/σ_y=1.27±0.09. An analogous analysis was performed using the imprints observed on block B3B7 and on foils B1F4 and B2F4, where the imprint shape was clearly discernible. The beam size ratios extracted from the imprint dimensions are consistent, within uncertainties, with those obtained from the measurements with beam instrumentation. This agreement provides an additional validation of the transverse beam size and supports the beam parameters used in the simulations.

6.3. Beam trajectory

The structural damage caused by the beam was assessed in the previous section. The spatial distribution of the imprints can also be used to reconstruct the beam's trajectory, thereby enabling the offset of the centre of the beam and centre of the winding to be calculated for each sample, albeit with some margin of error, as discussed in this section. The beam trajectory can be estimated in two different ways. Online during the experiment or after it, upon opening the vessel, based on the position of traces of the beam in the vessel. In practice, the online procedure should ascertain that the beam will hit the samples as designed. Both approaches will be briefly discussed.

Metrology measurements were used to map the position of all samples inside the vessel, while survey measurements established the relationship between the metrology reference frame, the movable stages, and the incoming beam coordinate system. The survey revealed a small inclination of the vessel, resulting in a batch-dependent vertical offset when different horizontal stage positions were selected. The correct alignment between the vessel and the beam was subsequently verified during the beam-based alignment procedure. Beam position information from BPKG and BTV measurements, together with the known precision of the movable stages, allowed the beam offset with respect to each batch to be determined. The resulting offsets for all three batches are summarised in Table 6.2. As this procedure relies on several independent inputs with different and partly correlated uncertainties, a reliable estimate of the combined uncertainty is non-trivial and is therefore not provided.

Table 6.2.: The offset of the beam impact position in horizontal H and vertical V direction for all three batches. The values calculated with the online procedure *on* and based on the measured imprint location *meas* are shown.

	H^{on}(mm)	H^{meas}(mm)	V^{on}(mm)	V^{meas}(mm)
Batch 1	2.1	2.2 ± 0.3	1.2	0.7 ± 0.1
Batch 2	2.2	2.4 ± 1.1	1.0	0.1 ± 0.8
Batch 3	1.2	2.5 ± 1.5	0.1	−0.1 ± 1.2

After opening the vessel, the beam trajectory was estimated from the position of imprints found inside the vessel. The general approach was to fit the horizontal and vertical centres of all imprints in one batch as a function of the longitudinal distance between the imprints. The uncertainty of the offset for each batch is based on the uncertainties of positions, which are fitted and therefore inversely proportional to the number of imprints observed in the batch. The measured offsets are presented in Table 6.2. The agreement between the two methods further supports the validity of the discussed analysis.

The data from metrology measurements were used to calculate the offset of each coil from the offset found for each batch. The horizontal and vertical offset estimated for each coil sample is shown in Figure 6.8.

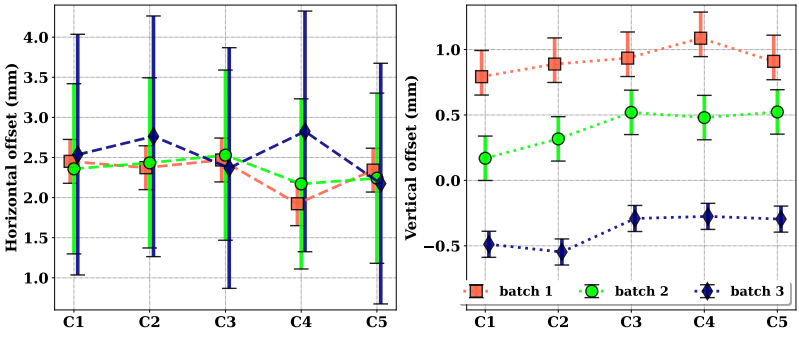

Figure 6.8.: Horizontal (left plot) and vertical (right plot) offset calculated for each coil sample in batch 1 (red squares), batch 2 (green circles), and batch 3 (blue diamonds).

When the results presented in Figure 6.8 are compared to the horizontal and vertical sizes of the winding as 25 mm and 4.9 mm, respectively, it confirms that each coil sample was impacted in the transverse mid-plane of the winding. However, limited knowledge about the exact position of each strand in the winding did not allow for resolving which specific strand was impacted, except for the Nb_3Sn coil B3Sn5, which was cut open. The two methods show consistent results within their uncertainties.

6.4. Post-irradiation transport current measurements

Following the visual inspection, transport current measurements were performed in the same conditions as before the irradiation (see Section 5.2). This section discusses the results of the measurements. The correlation of degradation with the conditions of each coil during the experiment, maximum deposited energy, peak temperature, temperature gradient and strain, and the interpretation of the results are described in Section 7.

The procedure for measuring the transport current was to train each coil until a transition was observed. This allowed to derive the critical current, and by comparing the value before and after the beam impact, the direct quantitative degradation could be calculated.

Results for Nb-Ti coils

The left and right sides of Figure 6.9 show the training of Nb-Ti coils before and after the beam impact, respectively. Starting from the sample B1Ti2, some coils showed temporary de-training after the beam impact. During the first current sweep, sample B1Ti5 reached only 675 A, which is 229 A less than when it was powered for the first time. The reduction of the current after the beam impact grows with increased energy deposited except for B1Ti3, which should suffer from the de-training more than B3Ti2, but nothing like this was observed. For coils B3Ti2, B3Ti4, and B3Ti5, three to four current sweeps were required to reach above 95 % of SSL. The observed temporary loss of training memory can be attributed to thermo-mechanical stresses inside the winding due to the rapid heating generated by the beam impact.

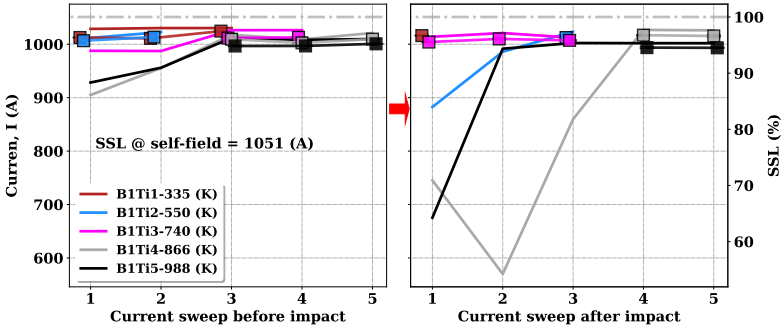

Figure 6.9.: Training of Nb-Ti samples before (left plot) and after (right plot) the beam impact. The quench current I_Q for each coil is shown (solid lines). For the current sweeps, which led to a transition, critical current I_c (squares) found from the fit with Equation 1.4 is shown in terms of current I and as a fraction of SSL (right y axis). Temporary de-training of the samples B1Ti2, B1Ti4 and B1Ti5 is clearly visible.

The mechanical stresses arising from coil powering may alter the residual stress state produced by the beam impact, potentially mitigating its effects. The stresses most likely changed the configuration of the strands, and several training quenches were required to find a new stable configuration. It needs to be noted that after the beam impact, a higher current ramping rate was used until 900 A to reduce the measurement time. The temporary current degradation was likely amplified by the higher current ramping rate during which the thermal runaways happened.

After re-training, all samples reached similar currents as before the beam impact, which means no degradation of their performance. The left plot of Figure 6.10 shows the ratio of the maximum obtained critical current before and after the beam impact $I_c/I_{c,0}$. The change of up to 2 % is in the order of the error of the measurements. No permanent degradation of performance was observed for the Nb-Ti coils.

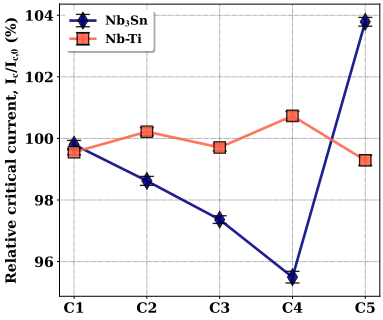

Figure 6.10.: Relative degradation of critical current $I_c/I_{c,0}$ of Nb-Ti coils in self-field (red squares) and Nb_3Sn coils at 7 T external magnetic field (blue diamonds). The maximum value of critical current before $I_{c,0}$ and after the beam impact is shown for each coil as obtained from the fit with Equation 1.4 using critical electric field criterium E_c of 1.0 µV cm^{-1}.

Results for Nb_3Sn coils

The second batch hosted two Nb_3Sn samples in the first two positions, and there was one shower block in front of them, same as for batch 3. During the experiment, no relevant difference was measured in the beam properties of pulses impacting batches 2 and 3 (see Table 6.1). The geometry of these two batches, *i.e.* the number of shower blocks and the space between samples and the shower block, was purposely identical to generate a minimum of statistics of the obtained results, in the region of deposited energy considered the most interesting. Therefore, the samples on these two positions are shown in plots both as B3Sn1 and B3Sn2 using circles for batch 2 and diamonds for batch 3. It needs to be noted that the impact's vertical position was different for batches 2 and 3 as discussed in Section 6.3.

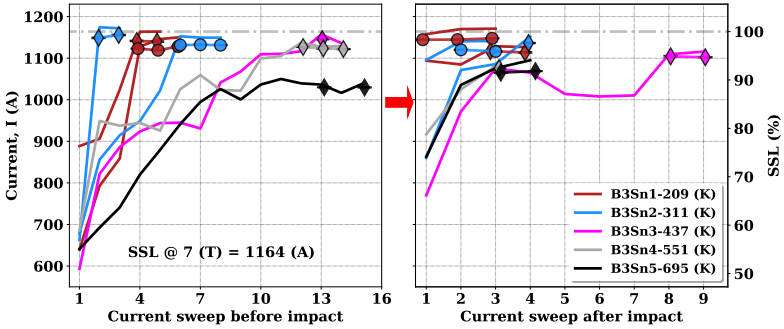

Figure 6.11.: Training of Nb_3Sn samples before (left plot) and after (right plot) the beam impact. The quench current I_Q for each coil is shown (solid lines). For the current sweeps, which led to a transition, critical current I_c (circles for samples in batch 2 and diamonds for batch 3) found from the fit with Equation 1.4 is shown in terms of current I and as a fraction of SSL (right y axis).

After the beam impact, the de-training was observed as for the Nb-Ti coils. In contrast to Nb-Ti samples, all Nb_3Sn samples reached a higher current directly after the beam impact than they reached right after the impregnation. The reason for this is possibly that the impregnation prevented the strands from mechanical movements as a result of the beam impact. To investigate the effect of de-training, the samples B3Sn3 and B3Sn5 were warmed up to room temperature and measurement was repeated as shown in Figure 6.12. After the beam impact, during which the coils went through multiple thermal cycles B3Sn5 reached 863 A during the first current sweep. After another thermal cycles, the maximum current during the first sweep was more than 131 A higher than right after the beam impact. In contrast, the measurements done for coil B3Sn3 show that the thermal cycle alone can cause de-training to a similar extent. Thus relation between beam impact and de-training cannot be derived, as the effect of the thermal cycle is masking the effect.

Figure 6.10 shows the ratio of the maximum obtained critical current before and after the beam impact $I_c/I_{c,0}$ at 7 T external field. A negligible change of critical current was observed for all samples except for coil B3Sn4, where a modest degradation of 5 % was observed. This implies no degradation of their performance.

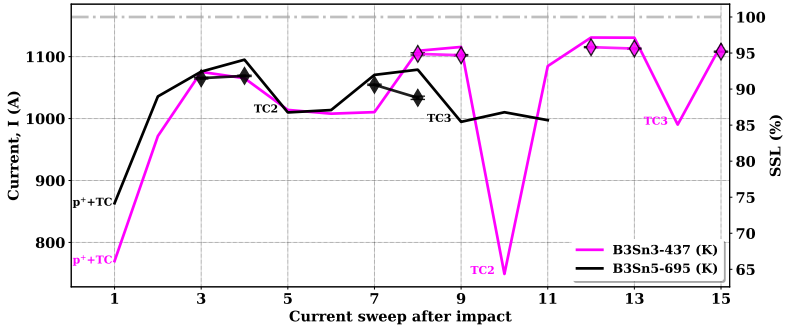

Figure 6.12.: Training of samples B3Sn3 and B3Sn5 after the beam impact (denoted with p^++TC) and another two additional thermal cycles (denoted with TC1 and TC2).

The modest degradation of the critical current suggests that the induced damage was insufficient to trigger the primary damage mechanism observed in the strand experiment [3]–[5], filament breakage. The stress produced by the beam heating was not severe enough to cause a significant reduction in the critical current. To exclude an alternation of upper critical field B_{c2}, samples B3Sn3-5 were qualified using transport current measurements at higher external magnetic fields from 15 T to 19 T.

The left side of Figure 6.13 shows the critical current of samples B3Sn3-5 at different external magnetic fields in range from 15 T to 18 T. Each sample was measured once at a different magnetic field. The critical currents at the different total magnetic fields were fitted with Equation 1.7 using C and B_{c2} as free parameters. The fit results together with uncertainties are shown in the right plot of Figure 6.13. As the Nb_3Sn samples were qualified only at 7 T external field before the beam impact, the results cannot be normalized to the pre-irradiation values. Therefore, the results were normalized to the maximum C and B_{c2} among these three samples. When the fit is performed in the full magnetic field domain, the B_{c2} of samples B3Sn3 and B3Sn5 is 3 % lower than for sample B3Sn4. However, if the result from the lowest magnetic field is omitted, the lowest B_{c2} is, in contrast, found for sample B3Sn4. Similarly, for the scaling constant, considering all magnetic fields, the samples B3Sn4 and B3Sn5 appear to reach only 92 % of the sample B3Sn3, but higher field measurements result in the comparable value of C and B_{c2} for samples B3Sn3 and B3Sn5. The fits for the three samples are consistent

with each other, which shows there is no relevant difference between their performance.

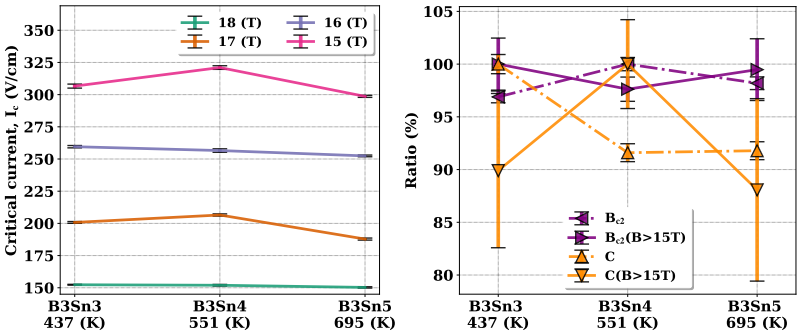

Figure 6.13.: *Left:* Critical current I_c at a different external magnetic field for the three Nb_3Sn samples with the highest deposited energy in batch 3. *Right:* Comparison of the fit results with Equation 1.7. The scaling constant C and upper critical field B_{c2} are shown. For a comparison the fit results from magnetic field above 15 T $C(B{>}15\,\mathrm{T})$ and $B_{c2}(B{>}15\,\mathrm{T})$ are shown.

From the discussed analysis, it was concluded that no degradation of any superconducting properties was found after the beam impact for any of the Nb_3Sn samples.

6.5. Energy deposition simulations

Based on the beam properties measured during the experiment (see Table 6.1) and the beam offset of each coil calculated from the beam imprints in the experimental setup (see Figure 6.8), the density of deposited energy in the experimental setup is calculated in this section. The transport code FLUKA is employed for that. In the following, the model of a coil is discussed, followed by the simulation results. The propagation of uncertainties of beam intensity, size and impact position into uncertainty in the deposited energy is discussed. Using the specific heat, the energy deposition is translated into temperature and spatial temperature gradients which are calculated for the strands in each coil. Finally, the melted imprints in witness foils are compared to the simulated imprint sizes, which benchmarks the presented simulations.

Geometry model

The FLUKA geometry model represents the experimental setup discussed in Section 5.3. The vacuum vessel and the thermal radiation shield are modelled as concentric cylinders with wall thicknesses as in the technical drawings. The radiation shield accommodates the second cooling stage plate on which a batch of coils is placed. Only one batch was used in the model for simplicity. The model of the Nb_3Sn coil is shown in Figure 6.14. The dimensions of the different parts were taken from the technical drawings, but the geometry of the winding was simplified. The strands are modelled to be perpendicular to the incoming beam and are always impacted in the horizontal centre along the length of the strands. This simplification is justified by the fact that during the simulation, the maximum deposited energy was of interest.

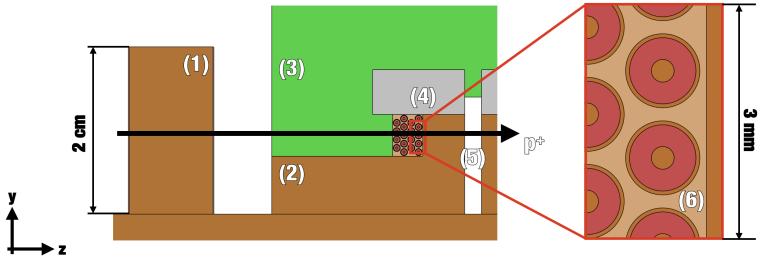

Figure 6.14.: Flair visualisation of the FLUKA model developed for the beam damage experiment, where the superconducting coils were impacted by a proton beam. Model of the coil showing a block of copper in front of a Nb_3Sn coil (1), semicircular terminal (2), protective clamp (3), blocking piece (4), and insulating sheet (5). Zoom on the winding illustrates Nb_3Sn strands and surrounding epoxy (6). The approximate beam path is indicated by the black arrow.

The strands are modelled as three concentric cylinders, with the inner and outer cylinders representing the copper matrix and the middle cylinder representing the filament region. The definition of the compounds and material densities of the filament region for Nb-Ti and Nb_3Sn strands reflects the Cu/SC ratio given in Table 1.1. The insulation of the strands is not considered, as its low mass, combination of low density combined with low total volume, has a negligible effect on the peak deposited energy. The shower blocks and witness foils were included in the model.

The purpose of the pre-experiment simulations was to design the layout, thereby defining the coil positions, beam intensities, and copper block thick-

nesses. The targeted temperature was based on the damage limits derived in the previous beam impact experiment at 4 K with the identical Nb-Ti and Nb_3Sn strands [3]. Hotspot temperatures in the windings of the sample coils were chosen to be between 300 K and 1200 K for Nb-Ti and 200 K and 800 K for Nb_3Sn coils. The aim was to have two Nb_3Sn samples reaching hotspots below 490 K, one around and two above it as this was the damage limit, based on the results from the strand experiment.

The designed beam had a circular profile with σ_x=σ_y=1 mm with an intensity of 3.6×10^{12} p^+ for batch 1 and 2.4×10^{12} p^+ for batches 2 and 3. During the actual experiment, the beams were larger (see Table 6.1). Therefore, the showers were produced over a wider area, resulting in a lower peak energy, therefore a lower hotspot temperature, and spatial temperature gradient. In contrast, the pulse had a slightly higher intensity, which has an opposite effect. Results of the preliminary simulations and a comparison of the designed and obtained beam parameters are presented in [7]. This paper also discusses direct comparison with the Geant4-based particle tracking code BDSIM [121]. These simulations showed that the two codes produced consistent energy deposition predictions, with only minor discrepancies in the winding regions. These were attributed to differences in the material contributions to a given bin, which arose from the two codes having non-identical scoring meshes. The preliminary simulations also allowed the assessment of various safety concerns. The simulations excluded the melting of copper inside the vessel and of the vessel itself. The total energy deposited in the vessel was used to calculate how much it would heat after each high-intensity shot, which defined the experimental procedure.

Refined simulations

Refined simulations were performed with the measured beam properties (see Table 6.1) and trajectory of the beam (see Figure 6.8). A statistical sample of 7 million primary particles was used, and the resulting map of deposited energy inside the vessel for batch 3 is shown in upper part of Figure 6.15. The simulation output for the density of deposited energy is in GeV/cm^3 per primary proton. The results were normalised to the intensity of the pulse in kJ/cm^3 to allow for a direct comparison with the previous studies [1]–[5]. The effect of the particle shower is directly visible.

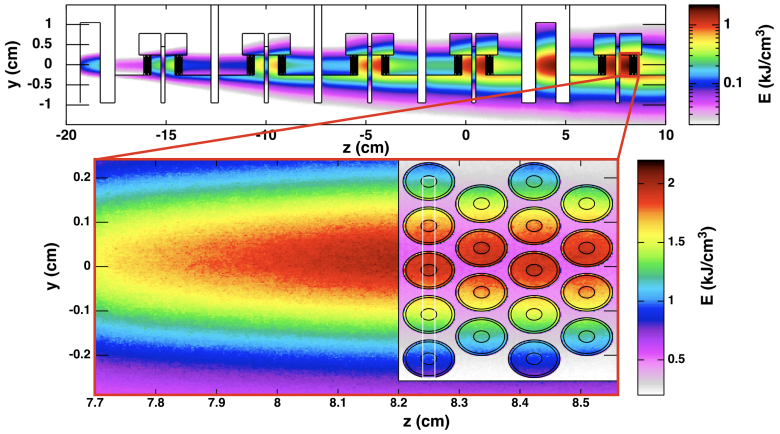

Figure 6.15.: Map of deposited energy resulting from the impact of the high-intensity proton pulse, averaged over 100 µm along the x-axis, for batch 3 based on the measured beam parameters. The beam comes from the left and moves in the z-direction.

The lower part of Figure 6.15 shows a zoom on the downstream side of the energy-deposition map for sample B3Sn5. The energy deposited in the core and strands is higher than in the other parts containing low-density organic materials. In the vertical direction, the energy deposited in the strand closest to the centre of the beam is relatively homogeneous as compared to other strands. In order to correlate the resilience of sample coils to the beam impact with the simulation results, the following quantities were extracted and are reported in Table 6.3 and Table 6.4 for the Nb-Ti and Nb_3Sn coils, respectively. The maximum energy deposited for each strand of each coil was derived. The winding core enhanced the generation of the shower. More energy was deposited in the downstream side of the coil, and the maximum energy was deposited on the strand closest to the centre of the beam in the vertical direction. The maximum energy deposited is directly proportional to the hotspot temperature in the sample. Along the beam direction, the deposited energy increases steadily in homogeneous material. In the direction transverse to the beam, the gradient of the deposited energy is higher than along the beam axis. The downstream side of Nb_3Sn B3Sn5 is shown in Figure 6.15.

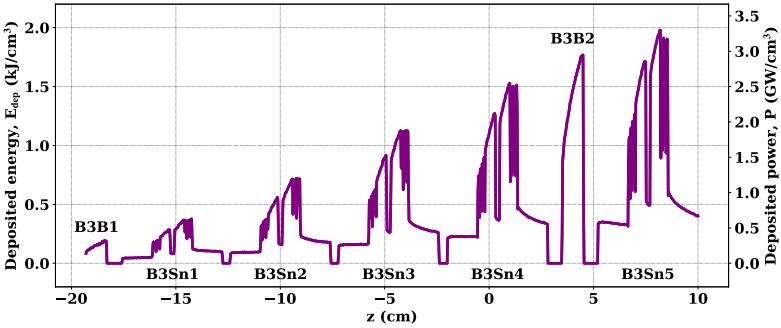

Figure 6.16.: The simulated energy deposition along the beam centre in both transverse planes for the batch 3.

Figure 6.16 shows the one-dimensional scoring of deposited energy along the beam centre in both transverse planes. The deposited energy can also be expressed in terms of power by assuming an impact duration of 600 ns for batch 1 and 900 ns for batches 2 and 3 (see Table 6.1).

The left side of the Figure 6.17 shows the energy deposited in the y direction, where the scoring was done in a strip going through the centre of the strands in the first winding layer (compare to Figure 6.15). The sudden drops in the deposited energy are caused by the low density of epoxy between the strands. The gradient in the y direction was calculated as the difference between the maximum and minimum energy deposited in each strand. The density of deposited energy along the length of the strand in the downstream side of each coil in batch 3 (z direction) is shown on the right side of Figure 6.17. The deposited energy follows a Gaussian distribution, as the material is homogeneous there. By numerical derivation, the maximum gradient in the z direction was found. For each coil, which was impacted by the beam during the experiment, the maximum deposited energy in a strand in the first layer, and the maximum transverse gradients were extracted. Additionally, the maximum energy deposited in any part of the coil was of interest because this can give the upper boundary of the later discussed damage limits. As defects in the epoxy were observed during the post-irradiation analysis, the maximum deposited energy in the epoxy was extracted for each Nb_3Sn coil.

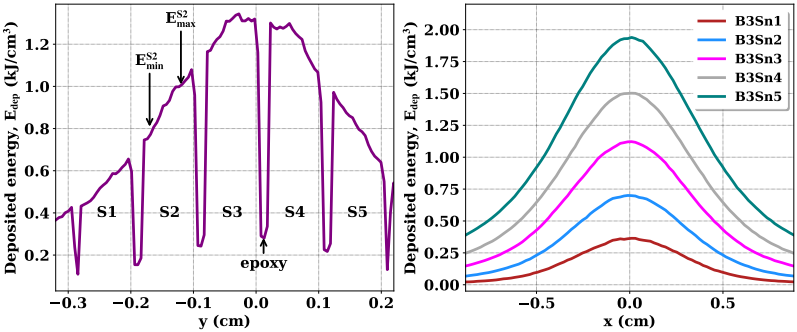

Figure 6.17.: *Left:* Spacial distribution of deposited energy in coil sample B3Sn4. The S1-5 indicate the Nb_3Sn strands in the first layer of windings on the downstream side of the coil. Higher deposited energy is interleaved with lower deposited energy regions where only low epoxy is present. The positions of the maximum E^{S2}_{max} and minimum E^{S2}_{min} energies deposited in the second strand are shown to illustrate the calculation of the transverse temperature gradient. *Right:* Spacial distribution of deposited energy in coil B3Sn1-5.

Table 6.3.: Peak deposited energy E, hotspot temperature T, and maximum transverse G_T in the most affected strands of the Nb-Ti coils in batch 1. The temperature was evaluated in a mixture of Nb-Ti and copper (see Figure 6.18). Uncertainties were calculated from the uncertainties of the beam properties.

Coil	B1Ti1	B1Ti2	B1Ti3	B1Ti4	B1Ti5
E (kJ/cm^3)	0.81±0.08	1.53±0.13	2.18±0.18	2.61±0.19	3.03±0.21
T (K)	335±23	550±39	740±52	866±56	988±61
G_T (K/mm)	104±22	167±34	196±24	237±30	272±25

The simulated maximum temperature in epoxy of B3Sn5 is (385±10 K) which is very close to glass transition temperature of 388 K to 419 K for the heat treatment used [122]. This is likely the reason for the defect observed in this coil when it was metallographically examined (see Figure 6.6).

Taking the discussed uncertainty of the impact position into account, the vertical position of the beam was systematically varied during the simulations. The upper part of strand 3 (S3) was assumed to be impacted, and the beam impact position was varied in steps of 100 µm. The more the centre of the primary beam overlapped with the strand, the higher was the deposited energy and gradient in the z direction and the lower was the gradient in the y

Table 6.4.: Peak deposited energy E, hotspot temperature T, and maximum transverse G_T in the most affected strands of the Nb-Ti coils in batch 3. Peak temperature in CTD101k epoxy $T_{CTD101k}$ is also shown. For the strands, the temperature was evaluated in a mixture of Nb_3Sn and copper (see Figure 6.18). Uncertainties were calculated from the uncertainties of the beam properties.

Coil	B3Sn1	B3Sn2	B3Sn3	B3Sn4	B3Sn5
E (kJ/cm^3)	0.35±0.03	0.63±0.04	0.99±0.06	1.32±0.08	1.75±0.09
T (K)	209±10	311±14	437±20	551±26	695±31
G_T (K/mm)	61±9	87±11	133±12	150±15	189±15
$T_{CTD101k}$ (K)	173±8	226±8	284±9	333±10	385±10

direction and vice versa. The error due to the uncertainty in the beam impact position was calculated as the difference between the highest and lowest value found during the simulations.

The deposited energy is linear to the beam intensity and scales approximately as $E_{dep} \propto 1/\sigma=(\sigma_x^2 + \sigma_y^2)^{-1/2}$, where σ_x and σ_y are the beam sizes in the horizontal and vertical planes. The uncertainties of the beam properties were calculated by subtracting the upper and lower extrema divided by two. The total uncertainty was taken as the quadratic sum of all uncertainties. Figure 6.18 shows the uncertainty of the maximum deposited energy for all Nb_3Sn coil samples in Batch 3.

The beam impact took 600 ns for batch 1 and 900 ns for batches 2 and 3 (see Table 6.1). On such a short time scale, heat conduction can be neglected, and an adiabatic temperature rise is assumed. Under this assumption, the peak temperature in a material is determined by the volumetric thermal capacity ρC_p. The volumetric thermal capacity for copper, Nb-Ti, and Nb_3Sn are summarized in [123]. During the analysis, the specific heat of copper [124] and CTD101k epoxy [122] were used. The specific heat data taken from the literature are shown in the left plot of Figure 6.18 [123]. Assuming a temperature of 4 K before the beam impact, the temperature rise can be calculated with Equation 3.3. For the Nb-Ti and the Nb_3Sn strands, the specific heat presented in Figure 6.18 was used, assuming the Cu/SC ratio discussed earlier (see Table 1.1). The right plot of Figure 6.18 shows the relationship between the density of deposited energy and the temperature rise from 4 K.

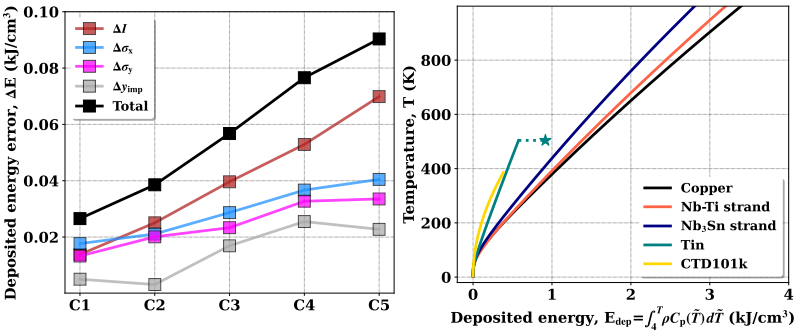

Figure 6.18.: *Left:* The different contributions to the uncertainty in the deposited energy for Nb_3Sn samples in batch 3. The effect of the error of the horizontal beam size $\Delta\sigma_x$, the vertical beam size $\Delta\sigma_y$, the pulse intensity ΔI, and the impact position in the vertical direction Δy_{imp} is shown, together with the total error for each sample. The total error for each sample is given by the quadratic sum of the listed terms. *Right:* Hot-spot temperature as a function of the energy deposited per unit volume.

Table 6.4 lists the maximum energy deposited for each coil sample, the hotspot temperature and axial and transverse temperature gradients together with the maximum temperature epoxy (only for Nb_3Sn samples). The uncertainty for each quantity is also given.

Benchmark of the energy deposition simulations

Witness foils placed on the shower blocks served several purposes. The beam trajectory was reconstructed based on their position (see Section 6.3). The shape of an imprint can be compared to the beam size measured with WS or BTV. Finally, its measured dimensions can be compared with the simulated size and thereby benchmark the energy deposition simulations.

The witness foils were modelled as 0.1 mm thick sheet of tin, and density of deposited energy was simulated. The energy required to melt a material E_{tot} is equal to the sum of energy needed to raise its temperature to the melting temperature E_{melt} and latent energy E_{lat}. The former was calculated with Equation 3.3 by integrating the specific heat of α-Tin [124] up to the melting temperature of tin of 505 K. The latter is equal to 59 kJ/k [125].

The distribution of energy deposition in the transverse plane can be well represented with a shifted 2D Gaussian distribution

$$f(x,y) = C + A\exp\left(-(x-\mu_x)^2/2\sigma_x^2 - (y-\mu_y)^2/2\sigma_y^2\right), \tag{6.1}$$

where $C+A$ is the height of the distribution, μ_x and μ_y are the positions of the centre of the peak, and σ_x and σ_y are the standard deviations in the horizontal and vertical plane, respectively. The isothermal ellipse at $f(x,y)$=E_{tot} has semi-major r_x and semi-minor r_y with a size equal to

$$r_x = \sqrt{2\sigma_x \ln\left(\frac{E_{tot.}-C}{A}\right)}, \quad r_y = \sqrt{2\sigma_y \ln\left(\frac{E_{tot.}-C}{A}\right)}. \tag{6.2}$$

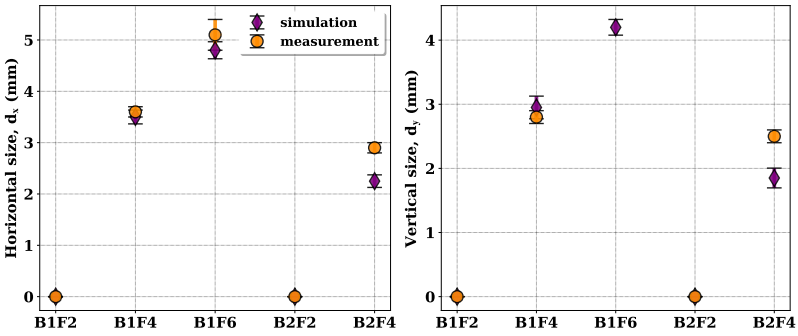

Figure 6.19.: Horizontal d_x and vertical d_y size of imprints on foils B1F2-6 in batch 1 and B1F2-4 in batch 2 from simulations (purple diamonds) and as measured (orange circles), respectively.

The expected size was calculated with Equation 6.2. Foils are labelled with nomenclature BXFY, where X denotes the batch number and Y the foil number. The foils were glued using vacuum grease, and all foils on the downstream side of the block, between the block and the winding (see Figure 5.3), were found to be intact. The imprint size was calculated in these foils, which are labelled with an even number. The imprint size was also measured in both transverse planes, except for B1F6, where only the upper part of the imprint was visible, so that only the horizontal size could be determined. The left and right plots of Figure 6.19 show the results of these calculations in the horizontal and vertical planes, respectively. The uncertainty was calculated

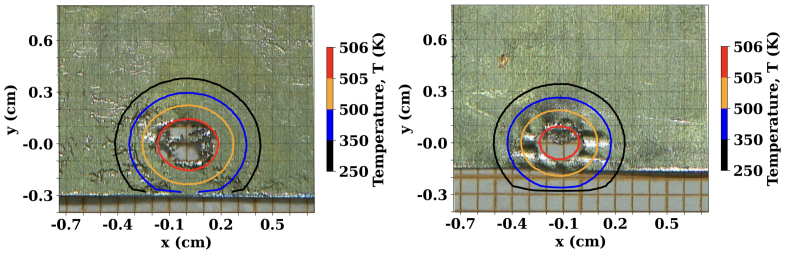

Figure 6.20.: Photos of B1F4 (left plot) and B2F4 (right plot) overlaid with the calculated temperature map.

with the same procedure as for the deposited energy discussed earlier in the section. Beam properties and the impact position were systematically varied, and the respective contributions were added quadratically.

The simulated and measured imprint sizes in batch 1 are in good agreement. For batch 2, the simulation correctly predicts that only the foil B2F2 will melt. However, the imprint size on B2F2 was simulated to be smaller, 24±5 % in x and 26±7 % in y. This discrepancy suggests that the energy deposition predicted by the simulation for batch 2 may be underestimated with respect to the experimental conditions. The difference cannot be explained by the uncertainties in beam size, beam intensity, or impact position.

Two possible explanations can be considered. A first hypothesis is that the material model of the Nb_3Sn coil used in the simulation is less realistic than that of the Nb-Ti coil, for which good agreement was observed in batch 1. If this were the case, even larger discrepancies would be expected for batch 3, which consisted exclusively of Nb_3Sn coils. However, this hypothesis cannot be tested, as none of the foils in batch 3 remained in place after the beam impact. A related implication would be the presence of more pronounced beam-induced imprints in the Nb-Ti coils of batch 1 compared to Nb_3Sn coils, which could in principle be investigated by metallographic analysis of samples B1Ti3 and B1Ti4 (similarly as for B3Sn5, see Section 6.2), but this has not been performed. A second possible explanation is that the foils in batch 2 were in better thermal contact with the shower block than assumed in the simulation, leading to larger measured imprint sizes. However, no experimental evidence is available to support this assumption.

In summary, while both hypotheses provide potential explanations for the observed discrepancy in batch 2, neither can be substantiated with the available data, and their plausibility therefore remains limited. This benchmarks the discussed FLUKA geometry model and enhances confidence in the presented quantities as reported in Table 6.3 and Table 6.4.

6.6. Mechanical response

This section discusses the simulation of the mechanical response of the Nb_3Sn coils after being hit by a beam. Based on the simulated energy deposition, the time-dependent changes in temperature and mechanical strain are calculated. ANSYS R2 is used for these calculations. First, the sample coil model is described, followed by the simulation results. The ANSYS model discussed in this section is based on the model developed for the strand damage experiment, which was discussed earlier [3]–[5], [126]. Finally, as no permanent degradation of the coils was observed during the experiment, the mechanical response was simulated for cases involving even higher energy deposition. These results could be used in the damage experiment with aged coils or any future experiments involving the same coil samples (see Section 6.8).

The model of a sample coil is based on the CAD designs. The strands have the same geometry and dimensions as in the FLUKA model discussed in the previous section. The definition of the materials is purposely identical to the model developed for the strand damage experiment. This allows a quantitative comparison of the results from both beam experiments at the end of this section.

Two geometries were prepared, the first one contains only strands, and the second one also takes other parts into account. Both models include only the upstream side of the coil. Nb_3Sn is a brittle material, exhibiting a linear elastic response in both tension and compression up to fracture. In contrast, copper, bronze, tin, and niobium are ductile and capable of plastic deformation before failure. Therefore, the mechanical properties of the matrix region are based on the tensile tests, which show a semi-plastic behaviour of the strands [127]. The second geometry contains the semicircular part of the copper core and the epoxy around the strands. The semicircular piece was further simplified by filling in the holes to rule out meshing problems.

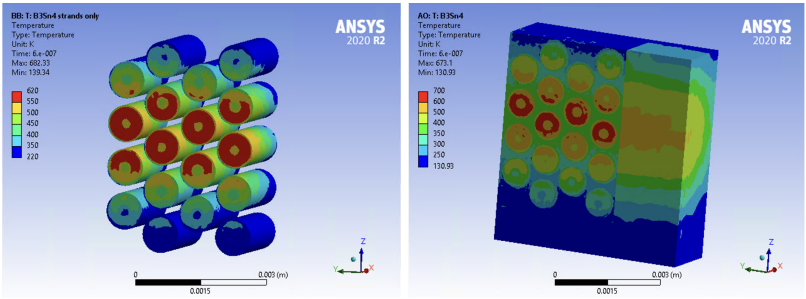

Figure 6.21.: The results of the transient simulations performed using ANSYS where a rise of temperature from 4 K is calculated. The plots show the temperature at the end of the beam heating at 600 ns when the hotspot temperature is maximal. The left and right plots show the results from models containing either the strands only or the strands, epoxy, and semicircular piece with the winding core.

The choice of boundary conditions at the interfaces of model parts is defined through contacts applied at their interfaces. At these interfaces, the contacting bodies are constrained such that no relative motion occurs between them. The interfaces are modelled using a penalty-based contact formulation, in which the contact constraints are enforced by means of penalty stiffness. This approach allows small elastic penetrations at the interfaces while ensuring numerical stability of the non-linear contact problem. By applying the mirror symmetry with respect to the y-z-plane, the mesh count is reduced by half. The coils were independent during the experiment, thus only one is taken into account per simulation.

The time-independent 3D map of deposited energy (see Figure 6.15) is imported into ANSYS as the density of deposited power. Geometry is the same for each coil, and what differs is the imported map of deposited power. Despite the beam pulse being bunched, with a bunch spacing of 25 ns, a continuous heating during the entire duration of the pulse was assumed. This simplifies the simulation, while it leads to a small difference in the order of 0.1 % in the final temperature [126].

During the first simulation step, an evolution of temperature during and after the experiment is calculated as shown for sample B3Sn4 in Figure 6.21. The beam heating starts at time t=0 s and lasts 600 ns. After 1 µs the results barely change, so to take some margin, a time interval of 2 µs is simulated.

The temperatures simulated with ANSYS are consistent with temperatures calculated earlier based on the FLUKA results.

To explore the evolution of the temperature after 2 µs, the maximum temperature in B3Sn3 was simulated until 1 s, as visible in Figure 6.22. The logarithmic decay of temperature is visible with the maximum temperature reaching 674 K at 600 ns, and reaching 455 K after 1 s.

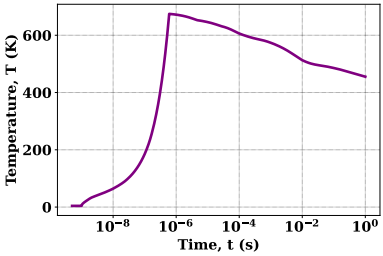

Figure 6.22.: Evolution of maximum temperature in B3Sn4 simulated until 1 s.

During the second simulation step, the output from the transient thermal simulation is imported into mechanical solver. There the deformation of material resulting from the temperature change is calculated. The simulated plastic strain in the matrix region containing the superconducting filaments is shown in Figure 6.23

Both models yielded consistent results for the simulated temperature evolution. However, differences were observed in the predicted strain distributions. In the strand-only model, the maximum strain occurs in the strands directly impacted by the beam centre, coinciding with the location of the maximum temperature. In contrast, the model including the surrounding epoxy and winding core predicts the maximum strain in strands located further from the beam centre, where the maximum transverse temperature gradient is found. The model including the epoxy and winding core is more realistic in terms of the mechanical environment of the strands. However, it also introduces additional material interfaces, mechanical boundary conditions, and material-property uncertainties, which significantly increase the overall uncertainty in the strain prediction. In particular, the mechanical properties of the epoxy at cryogenic temperature is not well reported in literature. For this reason, the strand-only model is retained for the quantitative analysis of strain.

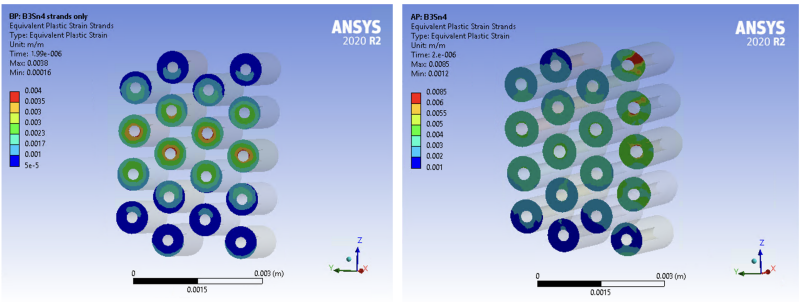

Figure 6.23.: The results of the transient mechanical simulations performed using ANSYS. The plots show the plastic strain at 2 µs. The left and right plots show the results from models containing either the strands only or the strands, epoxy, and semicircular piece with the winding core.

Based on uncertainties related to energy deposition, material properties, and mesh discretisation, the total uncertainty in the simulated strain was estimated to be 16 % for the strand experiment simulations. This value is conservatively adopted here. Two values of the plastic strain inside the matrix region were extracted from the simulation, the average and the maximum value and are presented in Table 6.5 for each Nb_3Sn sample in batch 3. The former characterises the damage of the entire strand while the latter predicts if the filaments at this particular location would brake. During the strand experiment, it was shown that the average strain better describes the observed degradation.

During transport current measurements, it was shown that none of the samples were damaged by the beam impact. To observe the degradation of the critical current resulting from direct beam impact, samples will be impacted by an even higher-intensity beam, as will be discussed in the next section. The coupled FLUKA and ANSYS simulations presented in this work were used to simulate strain at higher hotspot temperatures. To achieve this, the deposited energy map of B3Sn5 was scaled to a range of from 5 % to 50 %. This energy map was then imported into ANSYS, where average and maximum strain were simulated in the strands using the strand model. The results are shown in Table 6.5.

Coil	T (K)	ϵ average (%)	ϵ max (%)
B3Sn1	209	0.17	0.20
B3Sn2	311	0.19	0.26
B3Sn3	437	0.12	0.19
B3Sn4	551	0.26	0.38
B3Sn5	695	0.42	0.53
B3Sn5×1.1	740	0.46	0.62
B3Sn5×1.45	914	0.67	0.89
B3Sn4×2	971	0.73	0.99

Table 6.5.: The simulated temperatures and maximum and average plastic strains reached in sample coils B3Sn1-5 are shown. The light grey coils show the potential failure results for the upcoming damage experiment (see Chapter 6.8). The factor in front of the grey coil names is a scaling constant used to scale the energy deposition map, the input for the temperature and strain simulations.

Comparison with the earlier investigations

At this stage, the results obtained for the sample coils can be compared with those from the strand damage experiment, in which identical Nb-Ti and Nb_3Sn strands, not wound into coils, were directly impacted by the proton beam [3]–[5], [126]. For the Nb-Ti conductor, neither the strand samples nor the coils showed any degradation up to the maximum hotspot temperatures reached in the experiments. In the case of the Nb-Ti coils, a temporary detraining was observed following irradiation. However, the pre-irradiation critical current was recovered after 1 to 3 current sweeps.

In contrast, single Nb_3Sn strands exposed to hotspot temperatures of 490 K and above exhibited critical current degradation in the range of 20 % to 85 %, whereas no significant degradation was observed in Nb_3Sn coils up to hotspot temperatures of 695 K (see Figure 6.24). This discrepancy is attributed to the different mechanical boundary conditions in the two experiments. In the coil configuration, the strands are embedded in epoxy, which constrains their deformation and mitigates the stresses induced by the thermal expansion of surrounding metallic components during beam impact. Conversely, in the strand damage experiment, the expansion of the sample holder imposed additional mechanical loads directly onto the strands, leading to damage. This demonstrates that hotspot temperature alone is insufficient for a direct comparison between the strand and the coil damage experiment. Nevertheless,

the coil results provide a more realistic basis for extrapolation to full-scale accelerator magnets (see Section 7).

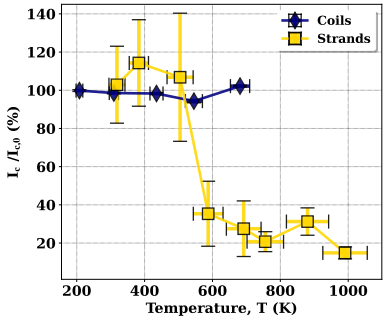

Figure 6.24.: Relative degradation of the measured critical transport current $I_c/I_{c,0}$ for strand and coil samples as a function of the hotspot temperature. Originally published in [8].

Other damage-relevant quantities, such as the transverse temperature gradient and the resulting plastic strain, show good agreement between the two damage experiments (see Figure 6.25). The transverse temperature gradient was identified as the driving mechanism for the strand bending observed in the strand experiment. Nevertheless, in the coil experiment it remained below levels expected to cause mechanical damage. The plastic strain, which can lead to irreversible filament damage, was simulated to stay below 0.41 % in the coil damage experiment, a value that appears insufficient to induce filament breakage.

6.7. Extrapolation to an superconducting accelerator magnet

Previous sections discussed the absence of permanent critical current degradation in the Nb-Ti and Nb_3Sn coils at hotspot temperatures of 988 K and 695 K, respectively. These damage limits are higher than those permitted during quenches, indicating a built-in safety margin against beam impact. However, extrapolating to full-size accelerator magnets is challenging due to differences in geometry and mechanical constraints. The response of the magnets may also depend on whether the impact occurs in a high-field or low-field region.

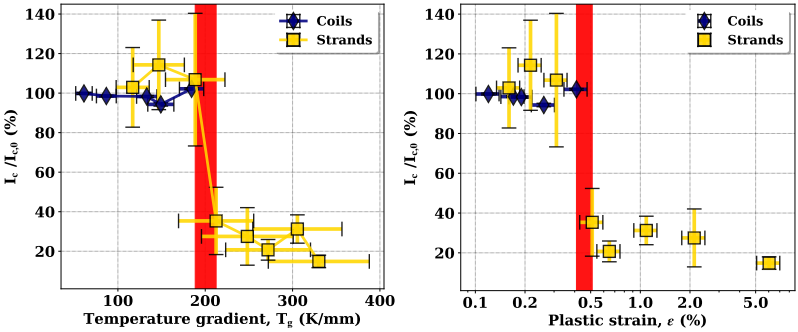

Figure 6.25.: Relative degradation of the measured critical transport current $I_c/I_{c,0}$ for strand and coil samples as a function of the transverse temperature gradient (left plot) and the plastic strain (right plot). Originally published in [8].

A conservative approach is to assume that the impacting beam produces a hotspot in the coil of the accelerator magnet, with the quench temperature occurring on top of the hotspot. The maximum hotspot temperature in an LHC dipole magnet was simulated to remain below 300 K [128]. The energy needed to heat copper from 1.9 K to 300 K, is 0.72 kJ cm^{-3}. Subtracting this value from the peak energy deposited in the Nb-Ti coil experiment (3.03 kJ cm^{-3}) yields a value of 2.31 kJ cm^{-3}. Therefore, if the energy deposited by the beam remains below this value no degradation is expected.

Similarly for Nb_3Sn, the maximum hotspot temperature during a quench in coils of HL-LHC inner triples was simulated at ~230 K [129]. This equates to 0.31 kJ cm^{-3} for the cable material, which is a mixture of copper, Nb_3Sn and G10. Subtracting this value from the peak energy deposited in the coil experiment (1.75 kJ cm^{-3}) equals 1.44 kJ cm^{-3}. Therefore, if the energy deposited by the beam stays below 1.44 kJ cm^{-3}, the total hotspot temperature will stay below 695 K, leading to no degradation as demonstrated during the coil damage experiment discussed in this thesis. However, this is a conservative approach, as the quench would be faster in such a case.

Additionally, relevant failure cases in the HL-LHC lead to large particle showers. These particle showers will heat larger parts of the coil, resulting in a faster quench, lower temperature gradients, and reduced mechanical strain in the coils. This has been observed in the LHC. Therefore, it can be

assumed that summing up the energy deposition and the expected hotspot of the magnet is largely conservative.

6.8. Damage experiment with radiation aged coils

The superconducting magnets of high-energy accelerators are at risk not only from instantaneous beam impact resulting from ultra-fast failures, but also from steady-state losses as discussed in Section 4. The peak dose in coils of HL-LHC inner triples will reach from 20 MGy to 30 MGy depends on the crossing-angle setting and can be reduced by alternating the crossing plane between interaction points [130], [131]. The mixed radiation field consists mainly of photons with a wide range of energies [132]. The effects of the radiation dose on the different parts of the magnets were discussed in Section 4.2. This section discusses the preparation of an upcoming experiment, denoted as damage experiment with aged coil. The design of the damage experiment was developed in the context of this work [9], but the execution and the analysis is not covered here.

The experiment was performed at the HiRadMat facility, investigating damage to sample coils that have undergone radiation ageing with γ-rays prior to beam impact. This simulates the anticipated integral dose levels that the HL-LHC final focusing triplet magnets will reach during their operational lifetime. Based on this, the damage limits for the sample coils will be derived and compared with the results of the coil damage experiment discussed in Section 7. This chapter describes the irradiation conditions in detail and compares the applied γ-field with that expected in coils of HL-LHC inner triples. It also presents energy-deposition simulations used to define the optimal proton-beam parameters required to reach the targeted energy-deposition levels. Finally, the experimental setup and procedure are described.

Experiment preparation

The Nb_3Sn samples (see Section 5.1) will be used for the experiment. Details of the samples, which were used, are presented in Table 6.6. Six of them had already been impacted by the beam as discussed in the previous sections. Nevertheless, they are reused as their performance was not altered. Four virgin samples, which have not been used, were qualified with transport

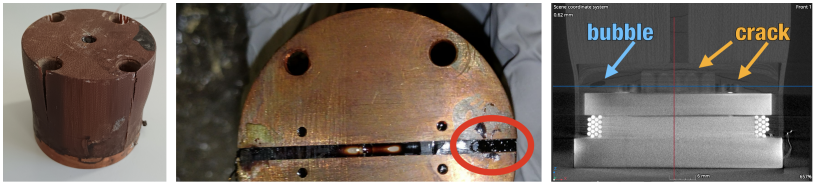

Figure 6.26.: Coil sample B1 after exposure to 30 MGy. *Left:* Deformed G10 clamp after the exposure. *Middle:* Bottom view of the sample showing bubbles inside the CTD101k epoxy. *Right:* CT scan performed upon the reception. A large bubble and many cracks are visible in the upper part of the coil (yellow arrows) where no dense material is present [133].

Table 6.6.: Overview of the sample coils prepared for the experiment. The samples are grouped into two batches, *A* and *B*. The history of each sample is described by the maximum temperature T_{61} reached during the beam damage experiment (HRMT-61) and the dose D accumulated during γ-irradiation. T_{70} and ∇T_{70} denote the target hot-spot temperatures and temperature gradients for the beam damage experiment with aged coils (HRMT-70).

sample	T_{61} (K)	D (MGray)	T_{70} (K)	∇T_{70} (K/mm)
A1	300 ± 16	30±9%	310	67
A2	197 ± 10	25±4%	516	130
A3	197 ± 10	25±3%	701	193
A4	454 ± 22	0	927	194
A5	0	0	1030	207
B1	0	30±4%	310	67
B2	0	25±8%	516	130
B3	300 ± 16	0	701	193
B4	574 ± 21	0	927	194
B5	0	0	1030	207

current measurements. The samples were subsequently sent to an irradiation facility and re-qualified upon reception. These measurements assessed the damage from the γ-irradiation itself. After the high-intensity beam impact, they will be qualified again to see the effect of both the long-term irradiation and the instantaneous beam impact.

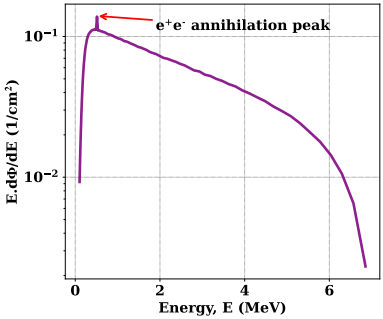

Figure 6.27.: Simulated spectrum of the photons produced with the electron beam.

γ-ray irradiation[1]

To prevent damage during handling and transport, each coil was enclosed in a cylindrical aluminium box with a wall thickness of 0.4 mm. The thickness is small compared to the radiation and nuclear interaction length [134]. Thus, the box had only a negligible influence on the dose received by the samples. In the facility, five samples inside the boxes were glued to an Ethafoam holder, and four alanine dosimeters were attached to each sample at equidistant angular positions of 90° around the circumference. The dose recorded by each dosimeter was used to assess the dose distribution on each side of the sample. Based on this information, the boxes were periodically rotated to ensure a uniform exposure. The dose rate ranged from 22 kGy h^{-1} to 50 kGy h^{-1}. The total dose received by each sample is given in Table 6.6. The uncertainty of the received dose is the difference between the minimum and maximum dose received by any side of the sample.

The photon field was produced by bombarding a water-cooled tantalum target with a 7 MeV/c electron beam. The photon energy spectrum, simulated in air with FLUKA, shows a peak energy around 270 keV with the maximum reaching several MeVs, as shown in Figure 6.27.

Upon receipt, the samples were subjected to a visual inspection, as shown in Figure 6.26, where a sample exposed to 30 MGy is shown. As a result of the irradiation, a colour change was observed in the G10 clamp (compare with

[1] STERIS in Däniken, Switzerland

Figure 5.1, item (b)). There is a small volume between the two semicircular pieces at the bottom of the coil where the epoxy is visible (see middle plot of Figure 6.26). Apart from a colour change, traces of bubbles are also visible. This behaviour has also been observed in other epoxy systems, such as MY750 and Araldite F [117]. However, this is observed for the first time for CTD101k. In addition, the G10 clamps of samples A2 and B1 exhibited cracking and deformation (see Figure 6.26). A thorough investigation of sample B1 was conducted using Computed Tomography (CT), as illustrated in right plot of Figure 6.26. The cracks and bubbles within the clamp are clearly visible, as is the deformation of the clamp. It is expected that there are also defects in the epoxy close to the winding. However, it is believed that bubbles were there already before the γ-irradiation. Unfortunately, the presence of dense materials inside the strands and the winding hinders the resolution of the CT scan for the epoxy around it.

Experimental setup design

The experiment was carried out in late 2025 at the HiRadMat facility at CERN. The experimental parameters and layout were defined during the design phase of the experiment. The final configuration was based on these preliminary design studies and simulations. The beam consisted of pulses of 24 bunches with 1.6×10^{11} protons per bunch, corresponding to a total of 3.84×10^{12} protons per pulse impacting a batch of samples. The transverse beam size was σ=1 mm.

The experimental setup followed the general concept of the previous coil damage experiment performed with non-aged sample coils (see Figure 5.7). The samples were arranged into two batches and exposed to the beam inside a dry-cooled cryogenic vessel operated at 4 K. The two batches were composed of samples with comparable irradiation histories in terms of absorbed γ dose and previously achieved hotspot temperatures during the former experiment. This selection was intended to ensure a similar initial level of material degradation. The preliminary layout of the samples, which formed the basis of the final experimental configuration, is shown in Figure 6.14.

In each batch, the first sample was irradiated to 30 MGy, as these coils were expected to be the most sensitive to beam-induced damage. These were followed by one or two samples exposed to 25 MGy, allowing the investigation of possible degradation at higher hot-spot temperatures but lower absorbed

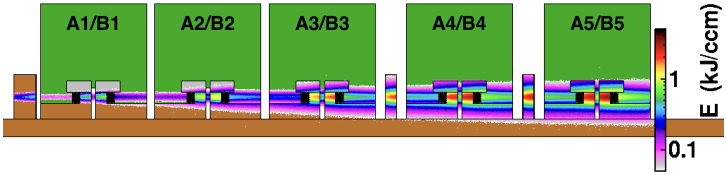

Figure 6.28.: FLUKA model with energy deposition overlay for one batch. The five sample coils are placed on the copper base plate (brown) and held by G10 clamps (green). The detailed winding geometry is reflected in the energy deposition patterns at the coil centres. Shower development from the copper blocks is clearly visible.

dose. Virgin samples were then placed downstream to experience energy deposition levels exceeding those reached in previous beam impact experiments, enabling the assessment of permanent degradation of the critical current. Finally, previously impacted samples were positioned at the end of each batch and exposed to the highest energy deposition levels.

Copper blocks were installed along the beam path to tailor the energy deposition profile within the coils. A 1 cm-thick block was placed upstream of the first coil, and a 0.5 cm-thick block was positioned upstream of the fourth and fifth coils in each batch. Based on the FLUKA model developed for the previous beam impact experiment, an updated simulation model was constructed during the design phase to estimate the energy deposition in individual strands of the coil samples using the assumed beam parameters. Figure 6.14 shows the FLUKA geometry with the corresponding energy deposition map. The simulations indicated that hot-spot temperatures in the range from approximately 300 K to 1030 K would be reached. The strain levels at these temperatures were simulated (see Table 6.5) and significant degradation of critical current is expected.

7. Summary and conclusion on damage limits of superconducting magnets

This thesis has presented a unique experiment in which Nb-Ti and Nb_3Sn superconducting coil samples were impacted with a high-intensity proton beam at cryogenic temperatures. The coils were produced and qualified for their critical current, confirming the stable performance of the samples prior to the beam impact. The design of the experiment was based on the preliminary energy deposition simulations, which were refined using the measured beam properties. The resulting hotspot temperatures and temperature gradients were obtained using their material properties. Multi-physics simulations (FLUKA for energy deposition and ANSYS for thermo-mechanical response) were performed and benchmarked against experimental observations, including melted tin foil imprints and post-irradiation microscopy.

The primary proton beam, with a momentum of 440 GeV/c, induced energy deposition up to $3.03 \pm 0.21\,\mathrm{kJ\,cm^{-3}}$ in Nb-Ti coils, corresponding to a hotspot temperature of 988 ± 61 K. The Nb-Ti coils demonstrated a strong resistance to the beam impact, and no permanent damage was observed. For the first time, radiation-induced de-training was observed above 335 K. The maximum current capabilities were temporarily suppressed from 56 % to 83 % and one to three current sweeps were required to train the coils back to the nominal current. This effect was attributed to the stress caused inside the winding due to the rapid heating resulting from the beam impact.

No permanent degradation was observed in Nb_3Sn coils either, despite the energy deposition up to $1.75 \pm 0.09\,\mathrm{kJ\,cm^{-3}}$ (equivalent to a hotspot temperature of 695 ± 31 K). The radiation-induced de-training was also observed for Nb_3Sn samples above 331 ± 14 K, but its effect cannot be distinguished from the effect of a thermal cycle. During an HL-LHC injection failure, the

simulated peak energy deposition in a coil (0.12 kJ cm^{-3}) [108] remains well below experimentally tested levels that showed no de-training, providing strong evidence that HL-LHC magnets are not at risk from beam-induced energy deposition.

A detailed investigation of the beam marks on the experimental setup enabled the trajectory of the beam during the experiment to be estimated. One Nb_3Sn sample was cut open to investigate a possible microscopic defect. A crack in the CTD101K was observed at the location of the impact. However, it did not affect the performance of the coil.

A thermo-mechanical model was built for the Nb_3Sn samples to confirm the consistency of the results obtained here with those obtained in the strand damage experiment performed within the same experimental campaign [3]–[5]. In this experiment, the permanent degradation of Nb_3Sn strands was measured following beam impact in a comparable environment. Despite the temperature of the most exposed coil being over 200 K higher than that of the first permanently degraded strand, no permanent degradation was observed. This is likely explained by the mechanical constraint imposed by the sample holder on the strands. This demonstrates that peak temperature alone is insufficient for comparing the results of the two experiments. However, using the transverse temperature gradient and plastic strain shows good agreement between the strand and coil experiments. The work presented here also validated experimental and modelling framework for studying beam-induced damage in superconducting systems.

Extrapolating these results to full-scale accelerator magnets is non-trivial due to differences in geometry and mechanical constraints, and depends on whether low- or high-field regions are impacted. The damage limits in terms of temperature are higher than those permitted during quenches, indicating a built-in safety margin against beam impact. However, it is important to note that the damage thresholds observed in terms of hotspot temperatures resulting solely from beam impact will be lower if the magnet is powered. In that case, combined beam heating and Joule heating should not exceed the aforementioned temperature damage limits.

An experiment to study the damage limits of radiation-aged superconducting sample coils from direct beam impact was prepared. The samples produced in the course of this work were irradiated up to 25 MGy and 30 MGy and subsequently impacted with the proton beam in a cryogenic environment. The beam impact experiment was carried out in October 2025 and the critical

current measurements are ongoing. This is particularly relevant for long-term operation scenarios of future colliders.

A key outcome of this work is the demonstration that both Nb-Ti and Nb_3Sn coils exhibit a significantly higher tolerance to rapid beam-induced energy deposition than previously established limits based on strand-level experiments. From an operational perspective, these results demonstrate that future high-energy hadron colliders, including the HL-LHC, possess a substantial safety margin against accidental beam losses in terms of irreversible magnet damage.

Publications and conference contributions

Articles:

- "**Damage Limits of Nb-Ti and Nb_3Sn Superconductors Due to High-Intensity Beam Impact**", D. Gancarcik *et al.*, *IEEE Transactions on Applied Superconductivity*, vol. 35, no. 7, Art. no. 4004215, 2025.

Conference proceedings:

- "**Beam Impact Experiment to Qualify the Damage Limits of Nb_3Sn Sample Coils Pre-Irradiated to 30 MGray**", D. Gancarcik *et al.*, in *Proc. IPAC 2025*, paper WEPB034, 2025.
- "**Energy Deposition Simulations for a Damage Experiment with Superconducting Sample Coils**", D. Gancarcik *et al.*, in *Proc. IPAC 2023*, Venice, Italy, paper WEPM058, 2023.
- "**Damage Experiment with Superconducting Sample Coils – Experimental Setup and Observations During Beam Impact**", D. Gancarcik *et al.*, in *Proc. IPAC 2023*, Venice, Italy, paper WEPM059, 2023.

Co-authored papers:

- "**Proof-of-Principle Experiment to Reconstruct the Trajectory of Dust Grains Interacting with the LHC Beams**", P. Ziegler *et al.*, in *Proc. IPAC 2025*, paper MOPM021, 2025.
- "**Investigations on Nb-Ti Superconducting Racetrack Coils under Pulsed-Current Excitations**", F. Abusaif *et al.*, in *Proc. IPAC 2023*, Venice, Italy, paper WEPM070, 2023.

Acknowledgements

This research was a life-changing experience and a huge leap in my development as a physicist and as a human. I am grateful to all those who guided me through it or supported me in any form.

Most of this work was carried out at CERN. The rest was done at the Karlsruhe Institute of Technology (KIT) which serves as my home university. I would like to deeply thank Prof. Dr. Anke-Susanne Müller for accepting me as a doctoral candidate at KIT, for her supervision, and for her support, particularly during the final stages of writing this thesis. I am especially grateful to Dr. Axel Bernhard, who provided invaluable guidance and warmth throughout this process. His often conversations served as a valuable forum for discussing the project. He demonstrated a high level of competence, passion and empathy, and was eager to help me in any way he could.

On the CERN side, I am much obliged to Dr. Daniel Wollmann for letting me conduct this research within the framework of the HL-LHC project. He helped overcome numerous obstacles in my professional journey through his motivational approach to problem-solving. The constructive and critical feedback that he provided, improved the quality of this work and helped me evolve. I gratefully acknowledge Cedric Hernalsteens, who was a great source of support during the preparation of the experiment and publishing its results. I want to thank Delphine Domange for her contribution to this project. She has been a joy to work with and I am happy that I could had entrusted the project to her. Finally, I would like to acknowledge the support of Stefan Thomsen, who assisted with the preliminary work of the damage experiment.

Many additional collaborators were essential to this work and are acknowledged below:

- F. Abusaif (KIT-IBPT) for her assistance with winding the coil samples and performing the Opera simulations.
- N. Glamann for providing technical drawings, and A. Grau and D. Saez de Jauregui (KIT-IBPT) for their help during the coil winding process, which contributed significantly to the success of this project.
- The team from the University of Geneva (M. Bonura, C. Senatore, D. Zurmuehle and R. Babouche) for carrying out the heat treatment

of the Nb_3Sn coils, their qualification, the post-irradiation transport current measurements, and for many insightful discussions.

- The HiRadMat team, in particular N. Charitonidis, A. Goillot, E. Matheson, A. Rahmoun and P. Simon, for their essential support during the preparation, installation and execution of the experiment.
- B. Bordini (TE-MPE-PE) for providing the Nb_3Sn cable and for valuable discussions on coil fabrication and the analysis of the qualification results.
- T. Koettig (TE-CRG-CL) for his support with cryogenic-related questions and maintenance of the cryogenic equipment.
- The polymer laboratory team, including D. Tommasini and S. Clement (TE-MSC-GLO) and C. Urscheler (TE-MSC-SMT), for impregnating the coils.
- E. Effinger and E. Calvo (SY-BI-BL) for providing the diamond detectors and for discussions regarding their proper use.
- J. Sestak and T. Raska (TE-VSC-BVO) for their help and advice with anything related to the vacuum equippment.
- M. Favre (TE-MPE-MP) and S. L. Bolton (TE-MPE-MI) for their help with technical drawings and the manufacturing of several experimental components.
- Last but not least, I would like to thank my friends P. A. Ziegler, M. R. Blaszkiewicz and H. A. Dostmann, as well as all the other wonderful colleagues I had the opportunity to meet during my time at CERN.

Tato stránka je věnována mým dcerám Laře a Isabel, manželce Tereze a rodičům Renátě a Břetislavovi

2L

Bibliography

[1] V. Raginel, D. Kleiven, K. Kulesz, *et al.*, "Change of critical current density in Nb-Ti and Nb_3Sn strands after millisecond heating", JACoW IPAC, May 2017, pp. 3528–3531. DOI: 10.18429/JACoW-IPAC2017-WEPVA111 (cit. on pp. 2, 45, 47, 85).

[2] V. Raginel, "Study of the Damage Mechanisms and Limits of Superconducting Magnet Components due to Beam Impact", Ph.D. dissertation, TU Vienna, 2018 (cit. on pp. 2, 45, 47, 85).

[3] A. Will, "Damage mechanisms in superconductors due to the impact of high energy proton beams and radiation tolerance of cryogenic diodes used in particle accelerator magnet systems", Ph.D. dissertation, Karlsruhe, KIT, 2021 (cit. on pp. 2, 12, 16, 45, 46, 52, 55, 56, 58, 82, 85, 93, 97, 106).

[4] A. Will *et al.*, "Beam impact experiment of 440 gev/p protons on superconducting wires and tapes in a cryogenic environment", *Proc. IPAC*, THPTS066, 2019. DOI: 10.18429/JACoW-IPAC2019-THPTS066 (cit. on pp. 2, 46, 55, 56, 58, 82, 85, 93, 97, 106).

[5] A. Will, A. Bernhard, M. Bonura, *et al.*, "Impact of 440 GeV Proton beams on Superconductors in a Cryogenic Environment", *J. Phys.: Conf. Ser.*, vol. 1559, 2020. DOI: 10.1088/1742-6596/1559/1/012060 (cit. on pp. 2, 46, 55, 56, 58, 82, 85, 93, 97, 106).

[6] D. Gancarcik, F. Abusaif, B. Bordini, *et al.*, "Damage experiment with superconducting sample coils - experimental setup and observations during beam impact", *J. of Phys: Conf. Ser.*, vol. 2687, p. 082 014, Jan. 2024. DOI: 10.1088/1742-6596/2687/8/082014 (cit. on pp. 2, 51, 70).

[7] F. Abusaif, A. Bernhard, D. Gancarcik, *et al.*, "Energy deposition simulations for a damage experiment with superconducting sample coils", *JACoW IPAC*, vol. 2023, WEPM058, 2023. DOI: 10.18429/JACoW-IPAC2023-WEPM058 (cit. on pp. 2, 51, 85).

[8] D. Gancarcik, A. Bernhard, M. Bonura, *et al.*, "Damage limits of NbTi and Nb_3Sn superconductors due to high-intensity beam impact", *IEEE Transactions on Applied Superconductivity*, pp. 1–16, 2025. DOI: 10.1109/TASC.2025.3596324 (cit. on pp. 2, 51, 98, 99).

[9] D. Gancarcik *et al.*, "Beam impact experiment to qualify the damage limits of Nb_3Sn sample coils pre-irradiated to 30 MGy", in *Proc. IPAC'25 - 16th International Particle Accelerator Conference*, JACoW Publishing, Geneva, Switzerland, 2025, pp. 1807–1810. DOI: 10.18429/JACoW-IPAC2025-WEPB034 (cit. on pp. 2, 100).

[10] Kleiner, Reinhold and Buckel, Werner, *Superconductivity: an introduction*. Wiley, Jan. 2016. DOI: 10.1002/9783527686513 (cit. on pp. 7, 9).

[11] M. Tinkham and V. Emery, "Introduction to superconductivity", *Physics Today*, vol. 49, no. 10, pp. 74–74, Oct. 1996, ISSN: 0031-9228. DOI: 10.1063/1.2807811 (cit. on p. 7).

[12] H. K. Onnes, "Further experiments with liquid helium. d. on the change of the electrical resistance of pure metals at very low temperatures, etc. v. the disappearance of the resistance of mercury", in K. Gavroglu and Y. Goudaroulis, Eds. Springer Netherlands, 1991 (cit. on p. 7).

[13] P. Drude, "Zur elektronentheorie der metalle", *Annalen der Physik*, vol. 306, no. 3, pp. 566–613, 1900. DOI: 10.1002/andp.19003060312 (cit. on p. 7).

[14] V. L. Ginzburg and L. D. Landau, "On the Theory of superconductivity", *Zh. Eksp. Teor. Fiz.*, vol. 20, D. ter Haar, Ed., pp. 1064–1082, 1950. DOI: 10.1016/b978-0-08-010586-4.50078-x (cit. on p. 8).

[15] J. Bardeen, L. N. Cooper, and J. R. Schrieffer, "Theory of superconductivity", *Phys. Rev.*, vol. 108, pp. 1175–1204, 5 Dec. 1957. DOI: 10.1103/PhysRev.108.1175 (cit. on p. 8).

[16] E. Maxwell, "Isotope effect in the superconductivity of mercury", *Phys. Rev.*, vol. 78, pp. 477–477, 4 May 1950. DOI: 10.1103/PhysRev.78.477 (cit. on p. 9).

[17] A. A. Abrikosov, "On the Magnetic properties of superconductors of the second group", *Sov. Phys. JETP*, vol. 5, pp. 1174–1182, 1957 (cit. on p. 9).

[18] W. V. Pogosov and V. R. Misko, "Vortex quantum tunneling versus thermal activation in ultrathin superconducting nanoislands", *Phys. Rev. B*, vol. 85, p. 224 508, 22 Jun. 2012. DOI: 10.1103/PhysRevB.85.224508 (cit. on p. 10).

[19] Y. B. Kim, C. F. Hempstead, and A. R. Strnad, "Flux-flow resistance in type-ii superconductors", *Phys. Rev.*, vol. 139, A1163–A1172, 4A Aug. 1965. DOI: 10.1103/PhysRev.139.A1163 (cit. on p. 10).

[20] P. W. Anderson and Y. B. Kim, "Hard superconductivity: Theory of the motion of abrikosov flux lines", *Rev. Mod. Phys.*, vol. 36, pp. 39–43, 1 Jan. 1964. DOI: 10.1103/RevModPhys.36.39 (cit. on p. 10).

[21] J. E. Kunzler, E. Buehler, F. S. L. Hsu, and J. H. Wernick, "Superconductivity in Nb_3Sn at high current density in a magnetic field of 88 kgauss", *Phys. Rev. Lett.*, vol. 6, pp. 89–91, 3 Feb. 1961. DOI: 10.1103/PhysRevLett.6.89 (cit. on p. 11).

[22] *CAS - CERN Accelerator School : Superconductivity and Cryogenics for Accelerators and Detectors: Erice, Italy 8 - 17 May 2002. CAS - CERN Accelerator School on Superconductivity and Cryogenics for Accelerators and Detectors*, CERN, CERN, 2004. DOI: 10.5170/CERN-2004-008 (cit. on p. 11).

[23] G. Volpini, "Quench propagation in 1-D and 2-D models of high current superconductors", in *Proceedings of the COMSOL Conference Milan*, 2009 (cit. on p. 11).

[24] R. L. Powell, H. M. Roder, and W. J. Hall, "Low-temperature transport properties of copper and its dilute alloys: Pure copper, annealed and cold-drawn", *Phys. Rev.*, vol. 115, pp. 314–323, 2 Jul. 1959. DOI: 10.1103/PhysRev.115.314 (cit. on p. 11).

[25] P. Bauer, R. Wolf, L. R. Oberli, and M. N. Wilson, "Minimum quench energies of LHC strands", *IEEE Trans. Appl. Supercond.*, vol. 9, M. A. Green and M. Adams, Eds., pp. 1137–1140, 1999. DOI: 10.1109/77.783499 (cit. on pp. 12, 28, 39).

[26] A. P. Verweij, "Electrodynamics of superconducting cables in accelerator magnets", Ph.D. dissertation, Twente U., Enschede, 1995 (cit. on p. 12).

[27] P. Lee, B. Strauss, M. Wilson, *et al.*, "Nb-Ti - from beginnings to perfection", in CRC/Taylor Francis, Jan. 2011, pp. 643–661 (cit. on p. 13).

[28] P. J. Lee *et al.*, "Composite superconductors: Chapter 5", in K. Osamura, Ed., Marcel Dekker, 1994 (cit. on p. 13).

[29] J. Somerkoski, D. Hampshire, H. Jones, R. Toivanen, and V. Lindroos, "Structure and superconducting property characterisation of MF Cu/Nb - 46.5% Ti superconductors", *IEEE Transactions on Magnetics*, vol. 23, no. 2, pp. 1629–1633, 1987. DOI: 10.1109/TMAG.1987.1064845 (cit. on p. 13).

[30] T. Boutboul, S. Le Naour, D. Leroy, L. Oberli, and V. Previtali, "Critical current density in superconducting Nb-Ti strands in the 100 mT to 11 T applied field range", *Applied Superconductivity, IEEE Transactions on*, vol. 16, pp. 1184–1187, Jul. 2006. DOI: 10.1109/TASC.2006.870777 (cit. on pp. 13, 14).

[31] K. Hübner and T. M. Taylor, "The Birth and Development of the First Hadron Collider The CERN Intersecting Storage Rings (ISR)", *Pontif. Acad. Sci. Scr. Varia*, vol. 119, pp. 180–192, 2011 (cit. on p. 14).

[32] L. Rossi, "The LHC Main Dipoles and Quadrupoles toward Series Production", *IEEE Trans. Appl. Supercond.*, vol. 13, pp. 1221–1228, 2003 (cit. on p. 14).

[33] P. Ferracin, G. Ambrosio, M. Anerella, *et al.*, "The HL-LHC Low-β Quadrupole Magnet MQXF: from Short Models to Long Prototypes", *IEEE Trans. Appl. Supercond.*, vol. 29, no. 5, p. 4 001 309, 2019. DOI: 10.1109/TASC.2019.2895908 (cit. on p. 14).

[34] M. Suenaga, D. O. Welch, R. L. Sabatini, O. F. Kammerer, and S. Okuda, "Superconducting critical temperatures, critical magnetic fields, lattice parameters, and chemical compositions of "bulk" pure and alloyed Nb_3Sn produced by the bronze process", *J. Appl. Phys.; (United States)*, vol. 59:3, Feb. 1986. DOI: 10.1063/1.336607 (cit. on p. 15).

[35] D. Schoerling and A. V. Zlobin, *Nb_3Sn accelerator magnets* (Particle acceleration and detection). Springer, 2019. DOI: 10.1007/978-3-030-16118-7 (cit. on p. 15).

[36] S. C. Hopkins, B. Medina-Clavijo, C. Rastoll, *et al.*, "Deformation Behavior and Degradation on Rutherford Cabling of Nb_3Sn Wires", *IEEE Trans. Appl. Supercond.*, vol. 34, no. 3, p. 6 001 308, 2024. DOI: 10.1109/tasc.2024.3375274 (cit. on p. 15).

[37] E. Barzi, N. Andreev, P. Li, V. Lombardo, D. Turrioni, and A. V. Zlobin, "Nb_3Sn RRP Strand and Rutherford Cable Development for a 15 T Dipole Demonstrator", *IEEE Trans. Appl. Supercond.*, vol. 26, no. 4, p. 4 804 305, 2016. DOI: 10.1109/TASC.2016.2535963 (cit. on p. 15).

[38] J. Ekin, *Experimental Techniques for Low-Temperature Measurements: Cryostat Design, Material Properties and Superconductor Critical-Current Testing*. Oxford University Press, Oct. 2006, ISBN: 9780198570547. DOI: 10.1093/acprof:oso/9780198570547.001.0001 (cit. on pp. 16, 17, 20, 21).

[39] L. Goodrich and F. Fickett, "Critical current measurements: A compendium of experimental results", *Cryogenics*, vol. 22, no. 5, pp. 225–241, 1982, ISSN: 0011-2275. DOI: 10.1016/0011-2275(82)90120-5 (cit. on p. 17).

[40] A. Goedeke, "Performance boundaries in Nb_3Sn superconductors", Ph.D. dissertation, University of Twente, 2005 (cit. on p. 17).

[41] J. Ekin, "Relationships between critical current and stress in Nb-Ti", *IEEE Transactions on Magnetics*, vol. 23, no. 2, pp. 1634–1637, 1987. DOI: 10.1109/TMAG.1987.1064844 (cit. on p. 18).

[42] G. Mondonico, B. Seeber, C. Senatore, *et al.*, "Improvement of electromechanical properties of an iter internal tin Nb_3Sn wire", *Journal of Applied Physics*, vol. 108, pp. 093 906–093 906, Dec. 2010. DOI: 10.1063/1.3499649 (cit. on pp. 18, 19).

[43] B. Seeber, G. Mondonico, and C. Senatore, "Toward a standard for critical current versus axial strain measurements of Nb_3Sn", *Superconductor Science and Technology*, vol. 25, no. 5, p. 054 002, Apr. 2012. DOI: 10.1088/0953-2048/25/5/054002 (cit. on p. 18).

[44] C. Senatore, T. Bagni, J. Ferradas-Troitino, B. Bordini, and A. Ballarino, "Degradation of ic due to residual stress in high-performance Nb_3Sn wires submitted to compressive transverse force", *Superconductor Science and Technology*, vol. 36, no. 7, p. 075 001, May 2023. DOI: 10.1088/1361-6668/acca50 (cit. on p. 18).

[45] J. F. Troitino, T. Bagni, C. Barth, *et al.*, "Effects of the initial axial strain state on the response to transverse stress of high-performance RRP Nb_3Sn wires", *Supercond. Sci. Technol.*, vol. 34, no. 3, p. 035 008, 2021. DOI: 10.1088/1361-6668/abd388 (cit. on pp. 18, 19).

[46] R. Flükiger, "Superconductivity for magnets", *CAS-CERN Accelerator School: Superconductivity for Accelerators - Proceedings*, Jan. 2015. DOI: 10.5170/CERN-2014-005.247 (cit. on p. 19).

[47] J. Ferradas Troitino, "Mechanical behavior of a Nb_3Sn accelerator magnet during a quench", Ph.D. dissertation, U. Geneva (main), 2022. DOI: 10.13097/archive-ouverte/unige:159696 (cit. on p. 19).

[48] T. Bagni, D. Mauro, M. Majkut, A. Rack, and C. Senatore, "Formation and propagation of cracks in rrp Nb_3Sn wires studied by deep learning applied to X-ray tomography", *Superconductor Science and Technology*, vol. 35, Sep. 2022. DOI: 10.1088/1361-6668/ac86ac (cit. on p. 19).

[49] D. Dew-Hughes, "Flux pinning mechanisms in type ii superconductors", *A Journal of Theoretical Experimental and Applied Physics*, vol. 30, no. 2, pp. 293–305, 1974. DOI: 10.1080/14786439808206556 (cit. on p. 20).

[50] L. Muzzi, V. Corato, A. Corte, *et al.*, "Direct observation of Nb_3Sn lattice deformation by high-energy X-ray diffraction in internal-tin wires subject to mechanical loads at 4.2 k", *Superconductor Science and Technology*, vol. 25, p. 054 006, Apr. 2012. DOI: 10.1088/0953-2048/25/5/054006 (cit. on p. 21).

[51] L. Bottura, "A practical fit for the critical surface of Nb-Ti", *IEEE Transactions on Applied Superconductivity*, vol. 10, no. 1, pp. 1054–1057, 2000. DOI: 10.1109/77.828413 (cit. on p. 21).

[52] J. W. Ekin, N. Cheggour, L. Goodrich, J. Splett, B. Bordini, and D. Richter, "Unified scaling law for flux pinning in practical superconductors: II. parameter testing, scaling constants, and the extrapolative scaling expression", *Superconductor Science and Technology*, vol. 29, no. 12, p. 123 002, Nov. 2016. DOI: 10.1088/0953-2048/29/12/123002 (cit. on p. 22).

[53] E. J. Kramer, "Scaling laws for flux pinning in hard superconductors", *Journal of Applied Physics*, vol. 44, no. 3, pp. 1360–1370, Mar. 1973, ISSN: 0021-8979. DOI: 10.1063/1.1662353 (cit. on p. 22).

[54] C. Segal, C. Barth, I. Falorio, *et al.*, "Evidence of Kramer extrapolation inaccuracy for predicting high field Nb_3Sn properties", *J. Phys.: Conf. Ser.*, vol. 1559, no. 1, p. 012 062, 2020. DOI: 10.1088/1742-6596/1559/1/012062 (cit. on p. 22).

[55] E. Lopienska, "The CERN accelerator complex, layout in 2022", 2022 (cit. on p. 23).

[56] S. Gilardoni and D. Manglunki, Eds., *Fifty years of the CERN Proton Synchrotron: Volume 1* (CERN Yellow Reports: Monographs). 2011. DOI: 10.5170/CERN-2011-004 (cit. on p. 24).

[57] *HiRadMat: A New Irradiation Facility for Material Testing at CERN*, CERN, 2011 (cit. on p. 25).

[58] F. J. Harden, A. Bouvard, N. Charitonidis, Y. Kadi, on behalf of the HiRadMat experiments, and facility support teams, "HiRadMat: A facility beyond the realms of materials testing", *Journal of Physics: Conference Series*, vol. 1350, no. 1, p. 012 162, Nov. 2019. DOI: 10.1088/1742-6596/1350/1/012162 (cit. on p. 25).

[59] "Targetry challenges HiRadMat", in *Proceedings of the 3rd J-PARC Symposium (J-PARC2019)*. DOI: 10.7566/JPSCP.33.011149 (cit. on p. 25).

[60] V. K. Verena Kain, "Machine Protection and Beam Quality during the LHC Injection Process", Ph.D. dissertation, Vienna Tech. U., 2005 (cit. on p. 25).

[61] S. Burger, B. Biskup, S. Mazzoni, and M. Turner, "Scintillation and OTR Screen Characterization with a 440 GeV/c Proton Beam in Air at the CERN HiRadMat Facility", in *5th International Beam Instrumentation Conference*, 2017, MOPG78. DOI: 10.18429/JACoW-IBIC2016-MOPG78 (cit. on p. 26).

[62] D. Belohrad, L. Jensen, O. Jones, M. Ludwig, and J. Savioz, "The LHC Fast BCT system: A comparison of Design Parameters with Initial Performance", CERN, Tech. Rep., 2010 (cit. on p. 26).

[63] E. B. Holzer, B. Dehning, E. Effnger, *et al.*, "Beam Loss Monitoring for LHC Machine Protection", *Phys. Procedia*, vol. 37, pp. 2055–2062, 2012. DOI: 10.1016/j.phpro.2012.04.110 (cit. on p. 26).

[64] *B2 poly-crystalline diamond detector*. [Online]. Available: https://cividec.at/detectors-B2.html (cit. on p. 26).

[65] O. S. Brüning, P. Collier, P. Lebrun, *et al.*, *LHC Design Report* (CERN Yellow Reports: Monographs). CERN, 2004. DOI: 10.5170/CERN-2004-003-V-1 (cit. on p. 26).

[66] T. A. collaboration, "Observation of a new particle in the search for the standard model higgs boson with the ATLAS detector at the LHC", *Physics Letters B*, vol. 716, no. 1, pp. 1–29, 2012, ISSN: 0370-2693. DOI: 10.1016/j.physletb.2012.08.020 (cit. on p. 26).

[67] T. C. collaboration, "Observation of a new boson at a mass of 125 GeV with the CMS experiment at the LHC", *Physics Letters B*, vol. 716, no. 1, pp. 30–61, 2012, ISSN: 0370-2693. DOI: 10.1016/j.physletb.2012.08.021 (cit. on p. 26).

[68] L. Rossi, "Superconducting magnets for the lhc main lattice", *IEEE Transactions on Applied Superconductivity*, vol. 14, no. 2, pp. 153–158, 2004. DOI: 10.1109/TASC.2004.829031 (cit. on p. 28).

[69] S. Stoynev, K. Riemer, A. V. Zlobin, *et al.*, "Analysis of Nb_3Sn accelerator magnet training", *IEEE Transactions on Applied Superconductivity*, vol. 29, no. 5, pp. 1–6, 2019. DOI: 10.1109/TASC.2019.2895554 (cit. on p. 28).

[70] G. Apollinari *et al.*, "High-luminosity large hadron collider: Technical design report v. 0.1", CERN, Tech. Rep. CERN-2017-007-M, 2017. DOI: 10.23731/CYRM-2017-004 (cit. on p. 29).

[71] A. Ghodgaonkar, A. T. Sugunan, P. K. Govekar, M. R. Patil, K. Mazumdar, and on behalf of the CMS collaboration, "Pileup mitigation in hadron forward calorimeter at the Level-1 trigger of the CMS experiment for the HL-LHC", *Journal of Instrumentation*, vol. 20, no. 01, p. C01045, Jan. 2025. DOI: 10.1088/1748-0221/20/01/C01045 (cit. on p. 30).

[72] CTD-Materials, *CTD-101K epoxy resin system – high performance resins for cryogenic and radiation applications*, https://www.ctd-materials.com/wp-content/uploads/2014/05/CTD-101K-DS-2014.pdf, Jan. 2014 (cit. on p. 30).

[73] I. A. Santillana, S. Sgobba, M. D. Crouvizier, *et al.*, "Advanced examination of Nb_3Sn coils and conductors for the lhc luminosity upgrade: A methodology based on computed tomography and materialographic analyses", *Superconductor Science and Technology*, vol. 37, no. 8, p. 085 007, Jul. 2024. DOI: 10.1088/1361-6668/ad5a44 (cit. on pp. 30, 74).

[74] A. Lechner, "Particle interactions with matter", *CERN Yellow Rep. School Proc.*, vol. 5, p. 47, 2018. DOI: 10.23730/CYRSP-2018-005.47 (cit. on p. 31).

[75] W. R. Leo, *Techniques for Nuclear and Particle Physics Experiments: A How-to Approach*, 2nd. Springer, 1994, ISBN: 978-3-540-57280-0. DOI: 10.1007/978-3-642-57920-2 (cit. on p. 31).

[76] N. Bohr, "Ii. on the theory of the decrease of velocity of moving electrified particles on passing through matter", *The London, Edinburgh, and Dublin Philosophical Magazine and Journal of Science*, vol. 25, no. 145, pp. 10–31, 1913. DOI: 10.1080/14786440108634305 (cit. on p. 31).

[77] F. Bloch, "Zur bremsung rasch bewegter teilchen beim durchgang durch materie", *Annalen der Physik*, vol. 408, no. 3, pp. 285–320, 1933. DOI: 10.1002/andp.19334080303 (cit. on p. 31).

[78] H. Bethe, J. Ashkin, *et al.*, *Experimental Nuclear Physics*, E. Segrè, Ed. J. Wiley, 1953, p. 253 (cit. on p. 31).

[79] C. Patrignani *et al.*, "Review of Particle Physics", *Chin. Phys. C*, vol. 40, no. 10, p. 100 001, 2016. DOI: 10.1088/1674-1137/40/10/100001 (cit. on pp. 32, 34, 35).

[80] H. C. Pollock, "The discovery of synchrotron radiation", *American Journal of Physics*, vol. 51, no. 3, pp. 278–280, Mar. 1983, ISSN: 0002-9505. DOI: 10.1119/1.13289 (cit. on p. 32).

[81] J. F. Mahdi, "Calculation of the total mass stopping power for electrons in some human body tissues in the energy range 0.01-1000 mev", *Iraqi Journal of Physics*, vol. 15, no. 34, pp. 72–80, Jan. 2019. DOI: 10.30723/ijp.v15i34.122 (cit. on p. 33).

[82] R. P., "The quantum theory of radiation", *Nature*, vol. 138, no. 3490, pp. 483–484, 1936. DOI: 10.1038/138483a0 (cit. on p. 34).

[83] J. Friedman, "The discovery of quarks", *Annalen der Physik*, vol. 513, no. 1-2, pp. 109–121, 2001. DOI: 10.1002/andp.200151301-210 (cit. on p. 34).

[84] V. Baru, E. Epelbaum, A. A. Filin, C. Hanhart, H. Krebs, and F. Myhrer, "Threshold pion production in proton-proton collisions at NNLO in chiral EFT", *The European Physical Journal A*, vol. 52, no. 5, May 2016, ISSN: 1434-601X. DOI: 10.1140/epja/i2016-16146-6 (cit. on p. 34).

[85] R. W. Roussin, B. L. Kirk, and D. K. Trubey, "Radiation shielding and protection", in *Encyclopedia of Physical Science and Technology (Third Edition)*, R. A. Meyers, Ed., Academic Press, 2003, pp. 581–612, ISBN: 978-0-12-227410-7. DOI: 10.1016/B0-12-227410-5/00635-9 (cit. on p. 35).

[86] M. R. Blaszkiewicz, "Methods to optimize rare-event Monte Carlo reliability simulations for Large Hadron Collider Protection Systems", M.S. thesis, University of Amsterdam, 2022 (cit. on pp. 35, 42).

[87] C. Ahdida *et al.*, "New Capabilities of the FLUKA Multi-Purpose Code", *Front. in Phys.*, vol. 9, p. 788 253, 2022. DOI: 10.3389/fphy.2021.788253 (cit. on p. 36).

[88] G. Battistoni, T. Boehlen, F. Cerutti, *et al.*, "Overview of the FLUKA code", *Annals of Nuclear Energy*, vol. 82, pp. 10–18, 2015, ISSN: 0306-4549. DOI: 10.1016/j.anucene.2014.11.007 (cit. on p. 36).

[89] A. Bertarelli *et al.*, "Behaviour of advanced materials impacted by high energy particle beams", *J. Phys. Conf. Ser.*, vol. 451, p. 012 005, 2013. DOI: 10.1088/1742-6596/451/1/012005 (cit. on p. 37).

[90] F. Carra, "Thermomechanical response of advanced materials under quasi-instantaneous heating", Ph.D. dissertation, Politecnico di Torino, Oct. 2017 (cit. on p. 37).

[91] C. Wiesner, F. Carra, J. Don, *et al.*, "Study of Hydrodynamic-Tunnelling Effects Induced by High-Energy Proton Beams in Graphite", *JACoW IPAC*, vol. 2022, pp. 1870–1873, 2022. DOI: 10.18429/JACoW-IPAC2022-WEPOPT015 (cit. on p. 37).

[92] M. P. Nemeth, "An in-depth tutorial on constitutive equations for elastic anisotropic materials", NASA Langley Research Center, Tech. Rep., 2011 (cit. on p. 38).

[93] *ANSYS 2020 R2 documentation*, ANSYS, Inc., 2020 (cit. on p. 38).

[94] R. Courant, K. Friedrichs, and H. Lewy, "Über die partiellen differenzengleichungen der mathematischen physik", *Mathematische Annalen*, vol. 100, pp. 32–74, 1928 (cit. on p. 38).

[95] A. P. Verweij *et al.*, "Performance of the Main Dipole Magnet Circuits of the LHC during Commissioning", *Conf. Proc. C*, vol. 0806233, I. Andrian and C. Petit-Jean-Genaz, Eds., WEPD029, 2008 (cit. on p. 39).

[96] R. B. Appleby, B. Goddard, A. Gomez-Alonso, *et al.*, "Beam-related machine protection for the cern large hadron collider experiments", *Phys. Rev. ST Accel. Beams*, vol. 13, p. 061 002, 6 Jun. 2010. DOI: 10.1103/PhysRevSTAB.13.061002 (cit. on p. 40).

[97] R. Schmidt, R. Assmann, H. Burkhardt, *et al.*, "Beam loss scenarios and strategies for machine protection at the LHC", *AIP Conference Proceedings*, vol. 693, no. 1, pp. 184–187, Dec. 2003, ISSN: 0094-243X. DOI: 10.1063/1.1638351 (cit. on p. 40).

[98] R. Schmidt and J. Wenninger, "Machine Protection Issues and Strategies for the LHC", 2004 (cit. on p. 40).

[99] J. Barth, F. Bogyai, J.-C. Garnier, *et al.*, "A Modernized Architecture for the Post Mortem System at CERN", *JACoW IPAC*, vol. 2022, pp. 1557–1560, 2022. DOI: 10.18429/JACoW-IPAC2022-TUPOMS055 (cit. on p. 40).

[100] A. Priebe, B. Dehning, M. Sapinski, M. Q. Tran, and A. Verweij, "Investigations of quench limits of the LHC superconducting magnets", *IEEE Transactions on Applied Superconductivity*, vol. 23, no. 3, p. 4 701 205, 2013. DOI: 10.1109/TASC.2012.2236378 (cit. on p. 40).

[101] T. Podzorny, A. Hollos, A. Skoczen, *et al.*, "Data acquisition and supervision systems for the HL-LHC quench protection system - part I the hardware", *JACoW IPAC*, vol. 2023, THPA023, 2023. DOI: 10.18429/JACoW-IPAC2023-THPA023 (cit. on p. 40).

[102] F. Bordry, R. Denz, K. H. Mess, B. Puccio, F. Rodríguez-Mateos, and R. Schmidt, "Machine Protection for the LHC", CERN, Tech. Rep., 2001 (cit. on p. 40).

[103] B. Puccio, A. Castaneda, M. Kwiatkowski, I. Romera, and B. Todd, "The CERN Beam Interlock System: Principle and Operational Experience", *Conf. Proc. C*, vol. 100523, A. Noda, C. Petit-Jean-Genaz, V. R. W. Schaa, T. Shirai, and A. Shirakawa, Eds., WEPEB073, 2010 (cit. on p. 41).

[104] B. Todd, "A Beam Interlock System for CERN High Energy Accelerators", Ph.D. dissertation, Brunel U., 2006 (cit. on p. 41).

[105] R. Johnson, C. Martin, T. Podzorny, I. Romera, R. Secondo, and J. Uythoven, "The Consolidation of the CERN Beam Interlock System", *JACoW IPAC*, vol. '21, pp. 3309–3312, 2021. DOI: 10.18429/JACoW-IPAC2021-WEPAB282 (cit. on p. 41).

[106] CERN/AT/PhL, "Summary of the analysis of the 19 September 2008 incident at the LHC. Résumé de l'analyse de l'incident survenu le 19 septembre 2008 au LHC", CERN, Tech. Rep., 2008 (cit. on p. 42).

[107] B. H. F. Lindstrom, "Criticality of fast failures in the High Luminosity Large Hadron Collider", Ph.D. dissertation, Uppsala University, 2021 (cit. on p. 42).

[108] A. Lechner, M. Barnes, C. Bracco, *et al.*, "Protection of Superconducting Magnets in Case of Accidental Beam Losses during HL-LHC Injection", in *6th International Particle Accelerator Conference*, 2015, TUPTY049. DOI: 10.18429/JACoW-IPAC2015-TUPTY049 (cit. on pp. 42, 44, 106).

[109] J. Uythoven *et al.*, "Injection Protection Upgrade for the HL-LHC", in *6th International Particle Accelerator Conference*, 2015, TUPTY051. DOI: 10.18429/JACoW-IPAC2015-TUPTY051 (cit. on pp. 42, 44).

[110] A. Lechner, A. Alnuaimi, C. Bracco, *et al.*, "Energy Deposition Studies for Fast Losses during LHC Injection Failures", *Conf. Proc.*, vol. C130512, TUPFI027, 2013 (cit. on p. 42).

[111] D. Carbajo Perez, E. Berthomé, C. Bertone, *et al.*, "New Generation CERN LHC Injection Dump - Assembly and Installation", *JACoW IPAC*, vol. 2021, pp. 3548–3551, 2021. DOI: 10.18429/JACoW-IPAC2021-WEPAB361 (cit. on p. 43).

[112] R. Srinivasan, R. R. Hall, W. D. Loehle, W. D. Wilson, and D. C. Allbee, "Chemical transformations of the polyimide kapton brought about by ultraviolet laser radiation", *Journal of Applied Physics*, vol. 78, no. 8, pp. 4881–4887, Oct. 1995, ISSN: 0021-8979. DOI: 10.1063/1.359776 (cit. on p. 47).

[113] S. S. Roy, P. Potluri, S. Canfer, and G. Ellwood, "Braiding ultrathin layer for insulation of superconducting rutherford cables", *Journal of Industrial Textiles*, vol. 48, no. 5, pp. 827–847, 2018. DOI: 10.1177/1528083716661204 (cit. on p. 47).

[114] P. Wiker, "Thermomechanical Characterization of Epoxy Composites Used in High Field Magnet Coils", Norwegian U. Sci. Tech., Tech. Rep., 2021 (cit. on pp. 47, 48).

[115] *CTD-101K epoxy resin system* (cit. on p. 47).

[116] M. H. Van de Voorde, *Effects of radiation on materials and components* (CERN Academic Training Lecture). CERN, 1970. DOI: 10.5170/CERN-1970-005 (cit. on p. 48).

[117] D. M. Parragh, C. Scheuerlein, N. Martin, *et al.*, "Effect of Irradiation Temperature and Atmosphere on Aging of Epoxy Resins for Superconducting Magnets", *MDPI Polymers*, vol. 16, no. 3, p. 407, 2024. DOI: 10.3390/polym16030407 (cit. on pp. 48, 103).

[118] F. Abusaif, A. Bernhard, E. Bründermann, *et al.*, "Investigations on Nb-Ti superconducting racetrack coils under pulsed-current excitations. Investigations on Nb-Ti superconducting racetrack coils under pulsed-current excitations", *J. Phys.: Conf. Ser.*, vol. 2687, no. 8, p. 082 015, 2024. DOI: 10.1088/1742-6596/2687/8/082015 (cit. on pp. 55, 56).

[119] P. Simon, *Private discussion*, January 2025 (cit. on p. 69).

[120] M. D. Celuch, *Private communication*, March 2025 (cit. on p. 72).

[121] L. Nevay *et al.*, "BDSIM: An accelerator tracking code with particle-matter interactions", *Computer Physics Communications*, vol. 252, p. 107 200, 2020. DOI: 10.1016/j.cpc.2020.107200 (cit. on p. 85).

[122] C. Scheuerlein, "CTD101K epoxy resin system", CERN, Tech. Rep., Feb. 2025 (cit. on pp. 88, 89).

[123] S. Russenschuck, *Field computation for accelerator magnets*. Wiley, 2010. DOI: 10.1002/9783527635467 (cit. on p. 89).

[124] R. J. Corruccini and J. J. Gniewek, "Specific heats and enthalpies of technical solids at low temperatures", National Bureau of Standards, Washington, D.C., Tech. Rep., Oct. 1960 (cit. on pp. 89, 90).

[125] E. ToolBox, *Latent heat of melting for common solids*, https://www.engineeringtoolbox.com/latent-heat-melting-solids-d_96.html (cit. on p. 90).

[126] J. Schubert, "Damage study on single strand Nb_3Sn ultra-fast beam impact in cryogenic environment simulation with finite element method", M.S. thesis, Friedrich Schiller University Jena, 2020 (cit. on pp. 93, 94, 97).

[127] J. Ferradas Troitino, "Electromechanical characterization of Nb_3Sn conductors at university of Geneva", in *Workshop on Nb_3Sn Technology for Accelerator Magnets*, Oct. 12, 2018 (cit. on p. 93).

[128] F. Rodriguez-Mateos and F. Sonnemann, "Quench heater studies for the LHC magnets", in *Proceedings of the 2001 Particle Accelerator Conference*, 2001 (cit. on p. 99).

[129] E. Ravaioli, "Update on the inner triplet quench simulations and current in the circuit branches", in *Proceedings of the 12th HL-LHC Collaboration Meeting*, Sep. 2022 (cit. on p. 99).

[130] A. Ciccotelli, R. B. Appleby, F. Cerutti, *et al.*, "Energy deposition studies for the upgrade ii of lhcb at the cern large hadron collider", *Phys. Rev. Accel. Beams*, vol. 27, 6 Jun. 2024. DOI: 10.1103/PhysRevAccelBeams.27.061003 (cit. on p. 100).

[131] R. García Alía, M. Brugger, F. Cerutti, *et al.*, "LHC and HL-LHC: Present and future radiation environment in the high-luminosity collision points and RHA implications", *IEEE Transactions on Nuclear Science*, vol. 65, no. 1, pp. 448–456, 2018. DOI: 10.1109/TNS.2017.2776107 (cit. on p. 100).

[132] R. Flükiger, "Irradiation effects in low T_c superconductors", in *WAMSDO Workshop Accelerator Magnet Superconductors, Design and Optimization*, CERN, CERN, 2009. DOI: 10.5170/CERN-2009-001.55 (cit. on p. 100).

[133] M. D. Celuch, *Edms 3053689 uCT - HRMT61-B3Sn4 coil*. [Online]. Available: https://edms.cern.ch/document/3053689/1 (cit. on p. 101).

[134] P.A. Zyla and others (Particle Data Group), "Review of particle physics", *Progress of Theoretical and Experimental Physics*, vol. 2020, no. 083C01, 2020. DOI: 10.1093/ptep/ptaa104 (cit. on p. 102).